

ULTRAFAST CONTINUUM MID-INFRARED SPECTROSCOPY
OF HYDROGEN-BONDED DIMERS

A Dissertation

Presented to the Faculty of the Graduate School
of Cornell University

In Partial Fulfillment of the Requirements for the Degree of
Doctor of Philosophy

by

Ashley Marie Stingel

May 2016

© 2016 Ashley Marie Stingel

ULTRAFAST CONTINUUM MID-INFRARED SPECTROSCOPY OF HYDROGEN-BONDED DIMERS

Ashley Marie Stingel, Ph. D.

Cornell University 2016

Hydrogen-bonded systems are ubiquitous in nature, where they provide structure and pathways for energy dissipation. Cyclic, hydrogen-bonded interfaces are capable of mediating proton transfer, but these structures have broad and complex vibrational spectra. To study these vibrational features, an ultrafast continuum mid-infrared (CIR) laser pulse has been incorporated as the probe pulse in several vibrational spectroscopies used to study the vibrational dynamics and proton transfer of cyclic, hydrogen-bonded dimers. Unlike traditional ultrafast vibrational spectroscopy, which is limited to a few hundred cm^{-1} of bandwidth in a single experiment, ultrafast mid-infrared continuum spectroscopy allows vibrational dynamics and coupling to be observed across the full vibrational spectrum. The vibrational dynamics of the 7-azaindole—acetic acid heterodimer were studied with mid-infrared pump—CIR probe and two dimensional infrared (2D IR) spectroscopy, which revealed strong coupling across the spectrum and very fast energy transfer across the bridging hydrogen bonds. Additionally, photoinduced proton transfer was studied in the 7-azaindole homodimer with preliminary UV pump—CIR probe experiments, which showed the formation of the doubly proton-transferred tautomer and spectral signatures of proton transfer. Further development of ultrafast mid-IR spectroscopy was explored with the generation of high energy continuum mid-IR pulses in bulk chalcogenide glass.

BIOGRAPHICAL SKETCH

Ashley Stingel earned a Bachelor of Arts in Chemistry from Skidmore College in 2010. She then enrolled as a Ph.D. student in Chemistry and Chemical Biology at Cornell University, where she has completed her dissertation under the supervision of Professor Poul Petersen.

ACKNOWLEDGMENTS

Thank you to my parents, Sue and Earl Stingel, for being my first teachers and always encouraging me.

This would not be possible without the influence of many teachers, including M/Sgt Donald “Sarge” MacNeil and my first chemistry teacher, Mr. Jim Huie. Thank you to my professors at Skidmore College, especially Professors Judy Halstead and Kimberley Frederick, for their advice and encouragement during my undergraduate years and since.

I would also like to thank my committee members, Professor Roger Loring and Professor Floyd Davis, for their time and insight. Thank you to my colleagues in the Petersen group, especially Carmella and Heather, for making the past five and a half years interesting.

Most of all, thank you to my advisor, Professor Poul Petersen, for his encouragement and support, without which none of this would have happened.

This research presented in this dissertation was supported by the Arnold and Mable Beckman Foundation Young Investigator Award.

TABLE OF CONTENTS

Acknowledgements	iv
Table of Contents	v
List of Figures.....	viii
List of Tables.....	xiii
1 Hydrogen-Bonded Dimers	1
1.1 Overview	1
1.2 Photoinduced Proton Transfer	3
1.3 Vibrational Spectra of Hydrogen-Bonded Dimers	5
1.4 Vibrational Dynamics of Hydrogen-Bonded Dimers	7
1.5 Research Overview	11
2 Time-Resolved Spectroscopy	13
2.1 Time-Resolved Spectroscopy	13
2.2 Ultrafast Laser Pulses	14
2.2.1 Generation of Pulses	14
2.2.2 Overlap of Pulses	15
2.3 Pump-Probe Spectroscopy	16
2.3.1 Introduction to Pump-Probe Spectroscopy	16
2.3.2 Measuring Transient Signals	17
2.3.3 Pump-Probe Experimental Design	19
2.3.4 Pump-Probe Example: Rhodium Dicarbonyl	20
2.4 Two Dimensional Infrared Spectroscopy (2D IR)	23
2.4.1 Introduction to 2D IR Spectroscopy	23
2.4.2 Examples of 2D IR Spectra	27
2.3.3 2D IR Experimental Design	29
3 Ultrafast Mid-Infrared Continuum Pulses	31
3.1 Overview	31
3.2 Background.....	32
3.3 Generation of Ultrafast Mid-Infrared Continuum Pulses	32
3.3.1 Experimental Design	32
3.3.2 Alignment	35
3.4 Detection.....	37
3.4.1 Single Element Detection	37
3.4.2 Array Detector	38
3.5 Characterization of Mid-IR Continuum Pulses	41
3.5.1 Pulse Characterization Methods	41
3.5.2 Temporal Resolution and Dispersion	42
3.6 Applications in Ultrafast Spectroscopy	44
3.6.1 Pump-CIR Probe Spectroscopy	44

3.6.2 Probing the Full Vibrational Spectrum with 2D IR.....	45
4 Mid-Infrared Continuum Spectroscopy of the 7-Azaindole—Acetic Acid Heterodimer	48
4.1 Overview	48
4.2 Experimental Considerations.....	49
4.3 Results	51
4.4 Fitting	55
4.5 Conclusions	60
5 A Comprehensive Study of the Vibrational Dynamics of the 7-Azaindole—Acetic Acid Heterodimer	62
5.1 Overview	62
5.2 Experimental Design and Considerations	63
5.3 Mid IR Pump--CIR Probe Results and Discussion	64
5.3.1 High Frequency Transient Response of the 7AI--Ac Heterodimer.....	64
5.3.2 Fingerprint Modes	69
5.3.3 Energy Transfer and Vibrational Coupling	72
5.4 Conclusions	74
6 Two Dimensional Infrared Spectroscopy of the 7-Azaindole—Acetic Acid Heterodimer	75
6.1 Overview	75
6.2 2D IR of the 7AI--Ac Heterodimer	76
6.2.1 Experimental.....	76
6.2.2 Results	76
6.3 The Elusive Carbonyl.....	83
6.4 Conclusions from 2D IR.....	86
7 Photoinduced Proton Transfer in the 7-Azaindole Homodimer	87
7.1 Overview	87
7.2 Experimental Considerations and Design	88
7.2.1 Generation of UV Pump.....	88
7.2.2 Flowjet.....	89
7.2.3 Sample Considerations	91
7.3 Preliminary Results	93
7.4 Conclusions	98
8 Generation of Microjoule Mid-Infrared Supercontinuum Pulses in Chalcogenide Glasses	99
8.1 Overview	99
8.2 Background.....	100
8.2.1 Pulses for Nonlinear Infrared Spectroscopy.....	100
8.2.2 Mid-Infrared Supercontinuum Generation in Materials.....	100
8.3 Method.....	102

8.4 Results	104
8.5 Supercontinuum Sum Frequency Generation.....	111
8.6 Conclusions and Future Prospects.....	112
9 Conclusions and Future Prospects	113
9.1 Summary.....	113
9.2 Ultrafast Vibrational Spectroscopy of the 7AI-Ac Heterodimer.....	113
9.3 Proton Transfer in the 7AI Homodimer	114
9.4 Future Prospects for Ultrafast CIR Spectroscopy	114
9.4.1 Limitless Applications of Ultrafast CIR Spectroscopy	114
9.4.2 IR Pump--CIR Probe	115
9.4.3 UV Pump--CIR Probe	116
9.4.4 Beyond Vibrational Experiments	117
References	118

LIST OF FIGURES

1.1	The structures and vibrational spectra of the guanine-cytosine (G-C) and adenine-thymine (A-T) base pairs of DNA.....	2
1.2	The 7AI homodimer undergoes photoinduced double proton transfer. The mechanism of this process remains controversial...	4
1.3	FTIR Spectra and Structures of AcOH homodimer (red), 7AI—Ac heterodimer (blue), and 7AI homodimer (black).....	6
1.4	FTIR of 7AI—Ac, and the intensity spectrum of the CIR pulse and a traditional OPA pulse.....	12
2.1	The level diagram (a,d), absorbance (b,e), and transient (c,f) spectra of a single anharmonic vibrational mode without (a-c) and with (d-f) the influence of an IR pump pulse.....	16
2.2	Chopping the pump pulse to half of the probe frequency (top) creates adjacent pulses with and without the effect of the pump (middle). The small changes induced by the pump are clearer when viewed as a difference signal (bottom).....	18
2.3	A general pump-probe experimental set-up.....	19
2.4	RDC structure with CO stretches highlighted and the FTIR spectrum of these vibrations.....	20
2.5	Transient spectra of the CO stretches of RDC at 1 and 10 ps.....	21
2.6	Vibrational dynamics of the RDC CO stretches measured at single frequencies (top) and measured as a time-resolved transient spectrum (bottom).....	22
2.7	Pulse sequence used to measure 2D IR spectra.....	23
2.8	An inhomogeneous lineshape at early waiting times (left) becomes homogeneously broadened at later waiting times.....	24
2.9	Crosspeaks in 2D spectra can be caused by vibrational coupling (top) or energy transfer (bottom). The time evolution of the peaks is necessary to decipher the two processes.....	26
2.10	Structure (a) and FTIR spectrum of the cyanide stretch of N749 Black Dye, along with the 2D spectra at 0.2 and 5 ps, showing spectral diffusion over several ps.....	27
2.11	The 2D spectrum (left) of the CO stretches of RDC, with a noticeable offset in the induced off diagonal feature, caused by excitation into the $ 11\rangle$ mode as showed in the level diagram (right).....	28

2.12	The experimental set-up for 2D IR experiments. The pump (purple) beam is generated by an OPA and split into two pulse pairs in a Mach-Zehnder interferometer. The continuum probe (red) is crossed with the pump at the sample and then recollimated and dispersed onto an MCT array detector.....	29
3.1	Schematic of the generation of the ultrafast, mid-IR continuum pulse by nonlinear mixing of the first, second, and third harmonics of a 25 fs, 800 nm pulse.....	34
3.2	Beam path of CIR generation from the amplifier to the detector.....	36
3.3	The CIR spectrum measured on a single element MCT detector by scanning each of three gratings, and measured interferometrically with a commercial FTIR spectrometer.....	38
3.4	Transient Spectra of RDC measured on each of the three spectrometer gratings. From left to right, the bandwidth increases while the resolution decreases.....	39
3.5	CIR spectrum measured on the MCT array detector after being dispersed by grating 1 and grating 2.....	40
3.6	Pulse duration and spectral chirp obtained from the cross-correlation in germanium.....	42
3.7	Schematic (left) and results (right) of a cross correlation between an 1850 nm idler pulse and the CIR in germanium.....	43
3.8	Photograph of the CIR generation (top) and the CIR spectrum with the 7AI-Ac heterodimer spectrum.....	45
3.9	Schematic of 2D IR, showing the portion of the spectrum that can be obtained with OPA pulses in a one-color (green) or two-color (orange) geometry, and the 2D spectrum obtainable with an excitation pulse generated by an OPA and the CIR probe pulse (purple).....	46
4.1	Spectrum of the pump and probe pulses (top) and FTIR of the 7AI—Ac dimer (bottom) over the studied region.....	50
4.2	Figure 4.2: Transient spectra and fits of 7AI—Ac at time delays of 0.35, 1.0, and 2.5 ps.....	51

4.3	Full IR pump–CIR probe data set (negative adsorption change, bottom) spanning a frequency range of 1750 cm^{-1} in 25 cm^{-1} steps and a time delay of -1.0 to 2.75 ps in 50 fs steps.....	55
4.4	Fitting of the transient spectrum at 350 fs with the sum of six Gaussians, each corresponding to one of the observed features	56
4.5	The spectral fit (bottom) and residual (top) are shown from -1.00 to 2.75 ps	57
4.6	Fitted amplitudes of the six Gaussian peaks. The legend gives the five fixed center frequencies (1795 , 1939 , 3000 , 3260 , and 3320 cm^{-1}) and the average center frequency value of the floating peak (2450 cm^{-1}).....	58
4.7	Center frequency and peak width (fwhm) of the sixth Gaussian peak that was allowed to vary as a function of the pump–probe time delay. The dashed vertical line at 0.3 ps indicates the start of the single-exponential fits with time constants of 0.6 and 1.3 ps , respectively, as described in the text.....	59
5.1	Transient spectra of the 7AI–Ac heterodimer at 200 fs (bottom) after each of three excitation pulses shown with the FTIR at top.....	65
5.2	Transient response of the 7AI--Ac dimer following excitation of the OH stretch centered at 2500 cm^{-1}	67
5.3	Dynamics of the three high frequency modes following excitation of the OH stretch (a) and NH stretch (b).....	67
5.4	Transient response of the 7AI--Ac dimer following excitation of the coupled OH mode centered at 1940 cm^{-1}	68
5.5	Transient response of the 7AI--Ac dimer following excitation of the NH stretch centered at 3250 cm^{-1}	68
5.6	Transient response of the fingerprint modes following exciation at 2500 cm^{-1} (top) and 3250 cm^{-1} (bottom).....	70
5.7	Dynamics of three fingerprint modes following excitation of the OH (a,c) and NH stretches (b,d) on short (a,b) and long (c,d) time scales.....	71
6.1	Figure 6.1: 2D IR spectrum of 7AI--Ac measured with three excitation pulses (shown on the FTIR at top) and probed with the CIR pulse.....	77

6.2	Figure 6.2: The fingerprint region of the 2D IR spectrum of 7AI--Ac measured with three excitation pulses (shown on the FTIR at top) and probed with the CIR pulse.....	80
6.3	Figure 6.3: The carbonyl diagonal and cross peaks at each excitation pulse in parallel (left) and perpendicular (right) polarizations.....	85
7.1	Photoinduced tautomerization of the 7-azaindole homodimer occurs following UV excitation.....	87
7.2	The generation of the 300 nm pump pulse by quadrupling of the 1200 nm signal beam (top), and the resulting pulse spectrum with the UV absorbance spectrum fo the 7AI homodimer.....	89
7.3	The flow jet used for flowing samples for the UV pump--CIR probe experiments (left) and a close-up of the nozzle with a thin film of solvent flowing through the wire loop (right).....	90
7.4	FTIR spectrum of the 7AI homodimer in both carbon tetrachloride and cyclohexane.....	91
7.5	Transient spectra of 7AI homodimer at time dealys of 0.1 and 15 ps (top), and as a function of time (bottom).....	93
7.6	Transient response of the fingerprint modes show the broad induced absorbance decay away while a few narrower fingerprint modes remain at long times.....	95
7.7	Pump-probe spectrum measured from -1 to 4 ps in 50 fs steps (bottom) and transient spectra at time delays of -1, 0.1, 0.5, 1 and 4 ps (top).....	96
7.8	The 7AI homodimer transient response from -450 to 450 fs shows the fast rise time and small chirp across the entire spectrum.....	97
8.1	Experimental set-up for generation of mid-IR supercontinuum pulses in bulk chalcogenide glasses.....	104
8.2	Spectra of mid-infrared supercontinuum generated in the chalcogenide glasses, measured on both spectrometer gratings with glasses located 3.5 mm in front of the focus of the 30 μ J, 3750 nm incident pulse.....	105
8.3	Mid-infrared supercontinuum generated in IG2 (top) and IG6 (bottom) as a function of glass position with an incident 30 μ J, 3750 nm pulse.....	107

8.4	Broadening of mid-infrared supercontinuum generated in IG2 (top) and IG6 (bottom) as a function of the input wavelength, with the window located 3.5 mm in front of the focus of the incident pulse. Incident pulse energies were held constant at 30 μ J.....	109
8.5	Second order autocorrelation of the supercontinuum pulses generated in IG6 in a 0.3 mm thick GaSe crystal with no compression (top) and with 13 mm CaF ₂ in the beam.....	110
8.6	SFG spectrum of gold (black) and collagen (blue) measured with supercontinuum pulse generated in IG6.	111
9.1	The Zundel and Eigen structures for the excess proton in bulk water.....	115
9.2	The photoacid HPTS (hydroxypyrenetrisulfonate) releases a proton following excitation at 400 nm.....	116

LIST OF TABLES

3.1	Horiba Monochromator Grating Specifications.....	38
4.1	Fixed Parameters for Fitting 7AI-Ac Transient Response.....	57
8.1	Pulse Energies of Supercontinuum Pulses Generated in Chalcogenide Glasses at Positions Relative to the Focus.....	107

CHAPTER 1

HYDROGEN-BONDED DIMERS

1.1 Overview

Hydrogen bonding is ubiquitous in biological systems, where it provides structure and pathways for the dissipation of vibrational energy. One class of hydrogen-bonded structures is dimers formed by multiple hydrogen bonds bridging the interface of the two monomers. A classic example of this is the hydrogen bonding between the base pairs of deoxyribonucleic acid (DNA), shown in Figure 1.1, which have either two or three hydrogen bonds that connect the purine and pyrimidine bases and provide support for the double helix structure.¹ Hydrogen-bonded interfaces may also provide a pathway for energy dissipation from excited states²⁻⁵ and are important for proton-coupled electron transfer reactions in many chemical and biological systems.⁶⁻⁹ Proton transfer is thus integral to biological function and lies at the heart of bioenergetics and biomimetic energy conversion.^{8,9} For example, excited-state proton transfer within DNA following ultraviolet (UV) excitation has been proposed as an explanation for the photostability of DNA, but whether proton transfer occurs between DNA bases in solution remains controversial.^{2,9} Cyclic hydrogen-bonded structures, such as those found in DNA and those formed by carboxylic acid–amidine interfaces, are capable of mediating multiproton transfer.¹⁰⁻¹²

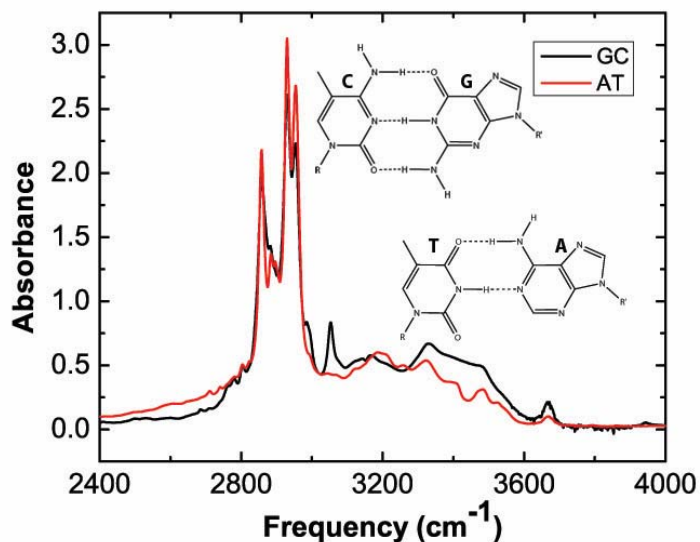


Figure 1.1: The structures of the guanine-cytosine (G-C) and adenine-thymine (A-T) base pairs of DNA, along with the infrared absorbance spectra of the solubilized base pairs in carbon tetrachloride.

Examining the ground state vibrational dynamics and couplings of such systems is important to developing an understanding of both the structures themselves and energy transport through the structure. The strength of the coupling between hydrogen-bonded vibrational modes within these cyclic structures influences the mechanism of multiproton transfer reactions. Vibrational spectroscopy is sensitive to molecular structure, and ultrafast spectroscopy is a valuable tool for investigating the dynamics and couplings of complex molecular systems at relevant time scales of femtoseconds (fs) to picoseconds (ps). However, hydrogen-bonded dimers often have very broad vibrational spectra, as shown in the linear absorbance spectra of solubilized DNA base pairs in carbon tetrachloride in Figure 1.1, while ultrafast vibrational spectroscopy is typically limited in bandwidth to a few hundred cm^{-1} . Here, novel ultrafast continuum

mid-infrared spectroscopy is used to explore the vibrational dynamics of cyclic, hydrogen-bonded dimers such as the 7-azaindole—acetic acid (7AI—Ac) heterodimer and the 7-azaindole (7AI) homodimer.

1.2 Photoinduced Proton Transfer

Since biological systems are complex and often part of larger macromolecules, model systems are frequently used to study the chemical structures of interest. In addition to mimicking the structure of DNA base pairs, many model systems have been shown to undergo inter- and intramolecular proton transfer.^{10,12–22} One such system, the cyclic, doubly hydrogen-bonded 7AI homodimer, has been studied extensively.<sup>10,12,11,23–
34</sup> Several decades ago, fluorescence experiments by Ingham et al¹⁰ showed that the doubly proton-transferred tautomer of 7AI forms following UV excitation of the dimer. In solvents with minimal solute-solvent interactions (such as 3-methylpentane), normal dimer fluorescence was observed around 330 nm, while tautomer fluorescence was observed at longer wavelengths. This confirmed the existence of both the starting dimer and proton-transferred tautomer, but not the mechanism of double proton transfer. The structures of both the normal dimer and the tautomer are shown in Figure 1.2. This photoinduced proton transfer was first studied with time-resolved fluorescence spectroscopy in 1979 by Eisenthal and coworkers,²³ who assigned an upper time limit of 5 ps, the temporal resolution of the experiment, to the proton transfer process. In 1991, Hochstrasser and coworkers²⁵ revisited the experiment with increased time resolution and determined a proton transfer rate of 1.4 ps.

A series of UV and visible experiments with better time resolution were carried out by Zewail^{26,28,30,33} and Tahara^{27,29,32,34}, revealing two decay times associated with double proton transfer in the 7AI homodimer. In the gas phase, Zewail and coworkers²⁶ observed two time scales of 650 fs and 3.3 ps. In solution, both Zewail and Tahara observed time scales of about 200 fs and 1100 ps. In various time-resolved fluorescence experiments, Tahara and coworkers³⁴ observed these time constants and assigned them to a concerted mechanism, in which the fast component is described as internal conversion between two excited states with significant overlap in UV absorbance, and the slower component is due to the concerted double proton transfer from the lower of the two excited dimer states. Zewail and coworkers³³ carried out a series of fluorescence and transient absorption experiments that revealed similar decay times, which they assigned to sequential single proton transfers in a stepwise mechanism.

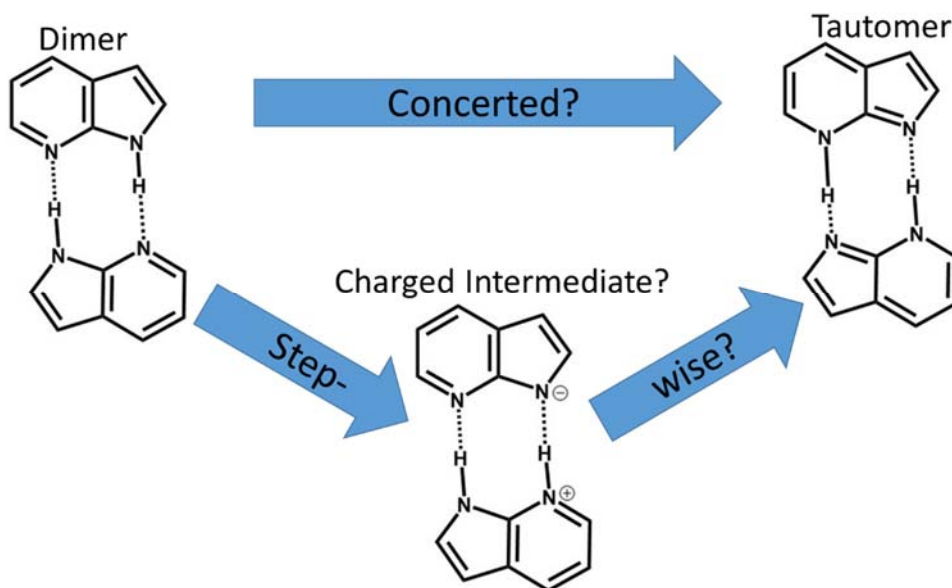


Figure 1.2: The 7AI homodimer undergoes photoinduced double proton transfer. The mechanism of this process remains controversial.

Both potential mechanisms for proton transfer in 7AI have theoretical support.^{33–}
³⁸ These earlier experiments used time-resolved electronic spectroscopies to determine the mechanism of proton transfer within hydrogen-bonded structures. In addition to being sensitive to proton transfer, electronic spectroscopy also probes electronic state transitions and solvent reorganization, making it difficult to isolate the proton transfer dynamics.^{26,27,33,34} Vibrational spectroscopy instead utilizes light in the mid-infrared (mid-IR) spectral region, which is resonant with the fundamental transitions of molecular vibrations. As such, vibrational spectroscopy is very sensitive to molecular structure and is accordingly a more specific probe of proton transfer. However, directly probing the chemical bonds that are breaking and forming during the proton transfer reaction is complicated by the very broad vibrational features associated with medium and strongly hydrogen-bonded structures.³⁹

1.3 Vibrational Spectra of Hydrogen-Bonded Dimers

Ultrafast vibrational spectroscopy has been used to study many biological systems,^{40–53} which can have very complex vibrational spectra, as shown in the FTIRs of solubilized DNA base pairs in carbon tetrachloride in Figure 1.1. For that reason, model systems have proven useful in understanding the behaviors and features of systems containing multiple intermolecular hydrogen bonds. To understand the features of cyclically hydrogen-bonded dimers, the homodimers of various carboxylic acids, such as acetic acid (AcOH), and amidines, such as the 7AI dimer discussed above, have been studied.^{54–69}

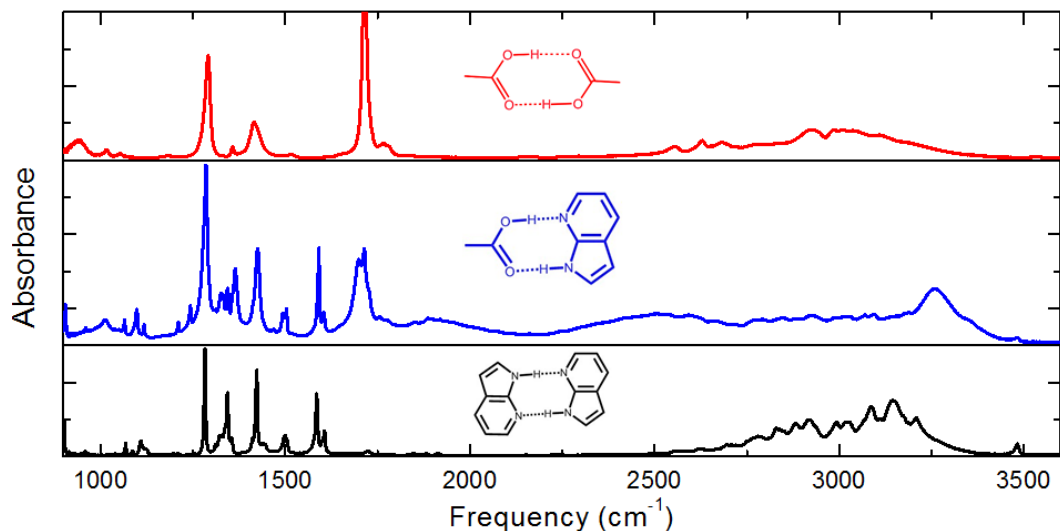


Figure 1.3: FTIR spectra and structures of AcOH homodimer (red), 7AI—Ac heterodimer (blue), and 7AI homodimer (black)

The broad features in the vibrational spectrum of the doubly hydrogen-bonded 7AI and AcOH homodimers can be seen in Figure 1.3. The XH groups involved in the hydrogen bonding of these symmetric dimers exhibit broad spectra around 3000 cm^{-1} that span more than 500 cm^{-1} . Like the respective homodimers, 7AI and AcOH form a cyclic, doubly hydrogen-bonded heterodimer that exhibits an even broader vibrational spectrum,^{61,67,69} also shown in Figure 1.3, and can undergo photoinduced double proton transfer.^{16,70,71} At high frequencies, the heterodimer spectrum exhibits a continuous absorption with three broad peaks, which have been previously assigned.^{61,69} The amino group of the 7AI is centered at approximately 3250 cm^{-1} , while the acid hydroxyl is centered at 2500 cm^{-1} . Both of these are redshifted and broadened significantly relative to the NH and OH peaks of the AcOH and 7AI monomers, which are seen as narrow peaks in Figure 1.3 at roughly 3540 and 3480 cm^{-1} , respectively. However, the amino group of the heterodimer is slightly blue-shifted relative to the broad absorbance of the

7AI homodimer, while the OH is redshifted by $\sim 500\text{ cm}^{-1}$ from the AcOH homodimer, to nearly 1000 cm^{-1} lower in frequency than the free OH of the monomer. The third peak at 1950 cm^{-1} results from a Fermi resonance between the OH stretch and the overtone of the OH bend.⁶⁹

Due to the very anharmonic potential of, and high degree of coupling within, hydrogen-bonded dimers, complex calculations are required to replicate the structure of these spectra.^{57,59,60,72} The substructure of the broad high-frequency peaks is due to Fermi resonances between the XH modes and overtones and combination bands of various fingerprint modes. As such, coupling between the hydrogen-bonded modes and low-frequency modes play an important role in the transfer and dissipation of vibrational energy. The bridging hydrogen bonds are an important influence on the spectrum and dynamics of these systems, but these generally occur at very low frequencies ($<200\text{ cm}^{-1}$) below the range of most vibrational spectrometers.^{61,65}

1.4 Vibrational Dynamics of Hydrogen-Bonded Dimers

Due to the very broad spectra and high degree of coupling in hydrogen-bonded systems, understanding the vibrational characteristics of these structures requires studying most of the vibrational spectrum. While linear infrared spectroscopy utilizes broadband, incoherent light sources that cover the whole vibrational range, most ultrafast vibrational spectroscopy relies on infrared pulses generated by optical parametric amplifiers (OPAs). These pulses are generally referred to as broadband, but typically only cover $100\text{-}500\text{ cm}^{-1}$, which can span only a fraction of these broad vibrational spectra. Traditional transient IR and two dimensional infrared spectroscopy (2D IR) experiments use replicates of a single mid-IR pulse as both pump and probe

pulses,^{52,53} while two-color experiments use different pump and probe frequencies to excite and probe different spectral regions. These experiments require knowing where to look for new spectral features, and are still limited to probing several hundred cm^{-1} in a single experiment.^{60,73,74} Full spectrum experiments can be performed by scanning traditional OPA pulses in the two-color scheme, but this is time consuming and introduces additional technical difficulties.⁷⁵⁻⁷⁸

Despite the limitations of OPAs, there have been several studies of the vibrational dynamics of cyclic intermolecular hydrogen-bonded structures.^{54,58,60,77,79} The vibrational dynamics of both the 7AI^{58,60,62} and AcOH⁵⁴⁻⁵⁶ homodimers have been studied extensively. Both the carbonyl⁵⁴ and hydroxyl^{56,57,60} stretches of the AcOH homodimer have been studied with linear and ultrafast vibrational spectroscopy and theoretical analyses. Lim and Hochstrasser⁵⁴ studied the vibrational dynamics of the acetic acid carbonyl at 1700 cm^{-1} and found that anharmonic coupling to nearby modes could not adequately describe the fast relaxation times. Ultrafast experiments^{55,56,60} and modeling of the high frequency spectrum⁵⁷ have shown that coupling between very low frequency (less than 200 cm^{-1}) hydrogen bond modes, fingerprint modes (about 1000 to 1700 cm^{-1}), and the high frequency spectrum (1700 - 3500 cm^{-1}) is important in understanding the hydrogen-bonded dimer.

Similar experimental^{58,60} and theoretical⁵⁹ work has been applied to the 7AI homodimer. Studying the high frequency 7AI homodimer dynamics, Nibbering and coworkers^{56,58,60,61} observed sub-picosecond dynamics in which the high frequency excitation decays rapidly into what they referred to as a “hot ground state.” In this state, the NH stretch has decayed to the ground state, but other modes remain excited and relax more slowly toward equilibrium. In both homodimers, a modulation of the transient response is observed corresponding to vibrations of the intermolecular hydrogen bonds. The very short relaxation times observed experimentally for the high

frequency modes of these systems are due to the strong coupling to the ring-bending and deformation modes and modulation by the low-frequency modes. Theoretical modeling of the high frequency spectra of these systems requires the inclusion of Fermi resonances caused by these modes to accurately reproduce the experimental spectra.^{57,60,69}

The 7AI homodimer has also been studied with IR pump/anti-Stokes Raman probe spectroscopy.⁶² Like two color pump-probes, this study allowed for the observation of one spectral region following the excitation of another. Unlike two color pump-probes, the use of spectrally narrow excitation pulses allowed for preferential excitation of the Fermi resonances while observing the fingerprint modes involved in the coupling, providing greater support for the calculation and assignment of the high frequency modes.^{59,62}

While symmetric model systems are useful tools to simplify complicated structures, biological systems are rarely symmetric. Heterodimers break the symmetry and further complicate both the vibrational spectrum and dynamics. Like the homodimers, hydrogen-bonded heterodimers also have very broad and complex vibrational spectra, such as the 7AI—Ac spectrum described in the previous section. Ultrafast vibrational studies of various heterodimers have observed similar behaviors to the homodimers, including fast decay of the excited modes with low frequency modulations.^{61,67,80}

The dimers of 2-pyridone, which isomerizes to form 2-hydroxypyridine, can form three types of cyclic dimers. Two of these are symmetric, but contain a pair of O-H \cdots N or O \cdots H-N hydrogen bonds, while the third contains one O-H \cdots O and one N \cdots H-N bond.^{63,64} Systems such as this one are more difficult to study because of the presence

of multiple structures, which can also be a problem in biological systems. For example, A-T base pairs are known to form non-Watson-Crick dimers.^{1,81}

Various other structures, such as those containing intramolecular hydrogen bonds^{82–84} and other types of complexes,^{66,68} are also interesting systems to study. For example, Nibbering and coworkers^{66,68} recently published several studies of aniline-*d*₅ hydrogen-bonded to 0, 1, or 2 dimethyl sulfoxide (DMSO) molecules. Using a combination of linear and nonlinear infrared techniques, including 2D IR and two color pump-probe experiments, they studied the origin of the spectral features as well as dynamics and coupling in the different structures. Like the dimers, the introduction of hydrogen bond acceptors to aniline greatly broadens the infrared spectrum by shifting the NH stretch frequency to allow greater overlap with the overtones of fingerprint modes and increasing the likelihood and strength of Fermi resonances.⁶⁶ Additionally, they used two-color pump-probe experiments to observe similar dynamics of the fingerprint modes regardless of the excitation frequency, suggesting strong coupling between the modes.⁶⁸

While model systems can be used to understand the dynamics and spectra of different structures, ultrafast vibrational spectroscopy has been used to study biological systems, such as DNA base pairs and macromolecules, directly.^{52,53} For example, Elsaesser and co-workers recently studied the asymmetric hydrogen-bonded structures of DNA base pairs in solution as well as hydrated films of DNA using both IR pump-probe and 2D IR spectroscopies.^{42,44,46,47,49} Like the symmetric model systems, these cyclic hydrogen-bonded biological systems also display structured bands from 2600 to 3400 cm⁻¹ due to Fermi resonances and couplings to low-frequency modes. The pump-

probe experiments again revealed sub-picosecond vibrational population decay times, and the 2D IR spectra resolved several individual NH modes and their couplings. In separate experiments, they have studied various parts of the DNA vibrational spectrum, including both the high frequency bands associated with the hydrogen-bonded modes^{44,46,47} and the low frequency fingerprint modes associated with backbone vibrations.⁴⁹

1.5 Research Overview

Recent works utilizing a mid-IR continuum probe have expanded these experiments so that the entire vibrational spectrum can be probed following excitation by a “traditional” pump pulse.^{48,67,77,79,85–90} Figure 1.4 compares the vibrational spectrum of the 7AI—Ac heterodimer to both a conventional OPA pulse and the mid-IR continuum pulse. In this work, the development of novel ultrafast mid-infrared continuum spectroscopies and its application to understanding the structures and dynamics of hydrogen-bonded dimers is presented.

This chapter provides an introduction to biologically-relevant and biomimetic hydrogen-bonded dimers. Chapter 2 gives an overview of the ultrafast vibrational spectroscopic techniques used to study such systems. In Chapter 3, the generation and characterization of ultrafast mid-infrared continuum (CIR) pulses, and their incorporation into ultrafast experiments is described. The first mid-IR pump—CIR probe study on the hydrogen-bonded 7AI—Ac heterodimer is presented in Chapter 4.

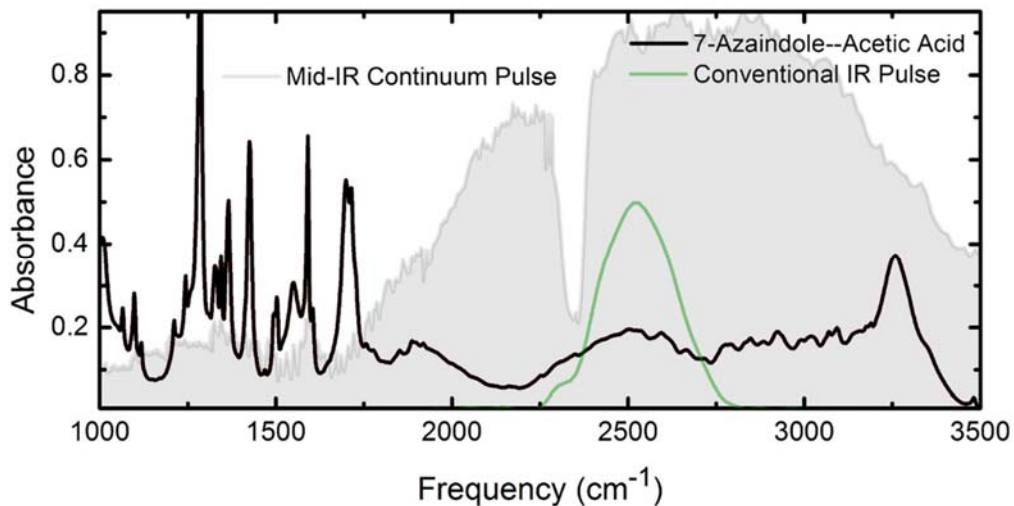


Figure 1.4: FTIR of 7AI—Ac, and the intensity spectrum of the CIR pulse and a traditional OPA pulse.

In Chapters 5 and 6, the results of comprehensive transient IR and 2D IR studies of the 7AI—Ac dimer are presented. Experimental considerations and preliminary results from the first UV pump—CIR probe study of the 7AI homodimer are summarized in Chapter 7. A novel technique for the generation of high energy mid-infrared supercontinuum pulses in bulk chalcogenide glasses is described in Chapter 8. The final chapter summarizes the overall conclusions and future prospects for ultrafast mid-infrared continuum spectroscopy and for understanding hydrogen-bonded systems.

CHAPTER 2

TIME-RESOLVED SPECTROSCOPY

2.1 Time-Resolved Spectroscopy

Time-resolved spectroscopy measures the changes in the spectral properties of a system following an induced change. In this work, several forms of ultrafast vibrational spectroscopy are used to study the dynamics of hydrogen-bonded systems. Ultrafast dynamics can only be observed by using laser pulses that are shorter in time than the process of interest. Vibrational dynamics of molecular systems occur on femtosecond (fs) to picosecond (ps) time scales and at infrared frequencies. As a result, these experiments require fs IR pulses to both induce a change in the system and measure the induced changes in the vibrational spectrum. In section 2.2, the generation of ultrafast pulses and methods for tuning these pulses to various frequencies are discussed. The overlap of pulses in space and time is also described. Two time-resolved techniques employed in this work are described and demonstrated. In section 2.3, transient third order ultrafast vibrational spectroscopy, commonly called “pump-probe” spectroscopy is described and demonstrated in (acetylacetonato)dicarbonylrhodium(I) (RDC). In section 2.4, the application and interpretation of two-dimensional infrared spectroscopy (2D IR) are discussed and demonstrated in both RDC and N749 Black Dye.

2.2 Ultrafast Laser Pulses

2.2.1 Generation of Pulses

All of the laser pulses used in this work are generated from 1 kHz, 25 fs, 800 nm pulses produced by an Ti:Sapphire regenerative amplifier (Coherent Legend Elite Duo). The amplifier is pumped by a Nd:YLF diode laser (Coherent Evolution HE) and amplifies seed pulses generated by a Ti:sapphire oscillator (Micra-5). The overall output of the amplifier is 5 W, which is divided into three separate beams, each of which goes through an independent grating compressor. The three beams have powers of approximately 3.0, 1.25 and 0.75 W (or mJ) at the amplifier output, and have a horizontal polarization (parallel to the laser table).

The strongest of the three beams (3 mJ) is used to drive a commercial optical parametric amplifier (OPA; Coherent OPerA Solo). The OPA converts 800 nm pulses into near-infrared signal and idler pulses at frequencies that sum to the 800 nm. Mid-infrared pulses are then generated by difference frequency mixing in a nonlinear crystal (AgGaS₂, 0.4 mm thick). In the experiments discussed here, the signal, idler, or DFG are used as excitation pulses. The signal can range from 1170 to 1600 nm and is horizontally polarized like the pump pulse, while the idler can range from 1573 nm to 2463 nm and is vertically polarized. Mid-IR pulses can be generated from 2.5 through 15 μm with polarization parallel to that of the 800 nm pump and the signal. Additional nonlinear mixing of the signal or idler pulses can be used to generate pump pulses down to less than 300 nm.

For the experiments discussed in this work, a mid-infrared continuum pulse is used to probe the vibrational spectrum of the system of interest. The generation of those ultrafast mid-infrared continuum pulses is driven by the 1.25 mJ portion of the 25 fs, 800 nm output, and will be described in detail in Chapter 3.

2.3.2 Overlap of Pulses

For time-resolved experiments, multiple laser pulses need to be overlapped in space and time. The timing of pulses is controlled by varying the path length of the beams. The duration of the pulses, 25 fs, corresponds to a thickness of only 7.5 μm . In comparison, sequential laser pulses at a repetition rate of 1 kHz are separated by 1 ms in time, or 300 km in space. As a result, the total path length (on the order of 10 m) of each overlapping beam must be the same to within 7.5 μm . This is controlled by directing the beams through retroreflectors mounted on motorized linear translation stages (Newport XMS100 and IMS600, controlled by an XPS-6 controller). The retroreflector consists of three mirrors arranged as a corner of a cube and reflects the beam back out parallel to the incoming beam. Changing the position of the retroreflector by moving the translation stage tunes the path length by twice the distance the stage travels, resulting in a timing change equal to twice the stage distance divided by the speed of light. The shorter stages (XMS100) can travel 100 mm in steps of 50 nm, resulting in a timing range of 667 ps in steps of less than 0.3 fs. The longer stage (IMS600) can travel 600 mm for a timing difference of 4 ns, but is less accurate and slower than the shorter stages. All stages can be controlled with provided software or programmed to interface with other instruments, such as monochromators and detectors.

Since the path length inside the OPA is several meters, the other beams need to be carefully routed to the sample in order to travel an equivalent distance. Although the stages can tune the path length by 200 to 1200 mm, the stationary optics must be set up and aligned with the optical path lengths of the beams within a few centimeters of each other in order for the pulses to overlap temporally.

2.3 Pump-Probe Spectroscopy

2.3.1 Introduction to Pump-Probe Spectroscopy

One short, intense laser pulse (“pump”) is used to induce a population change in the system of interest, while a second laser pulse (“probe”) measures the absorbance of the system. The timing between the two pulses is controlled very accurately by varying the path length of one (or both) beams with linear translation stages. In the case of infrared (IR) pump-probe spectroscopy, the probe pulse measures a spectrum that is equivalent to a linear absorbance spectrum—some portion of incident light excites the molecule from the vibrational ground state to the first excited state (the $0 \rightarrow 1$ or fundamental transition, as shown in Figure 2.1a), resulting in a peak in the IR spectrum, such as that shown in Figure 2.1b, that is characteristic of that specific vibration.

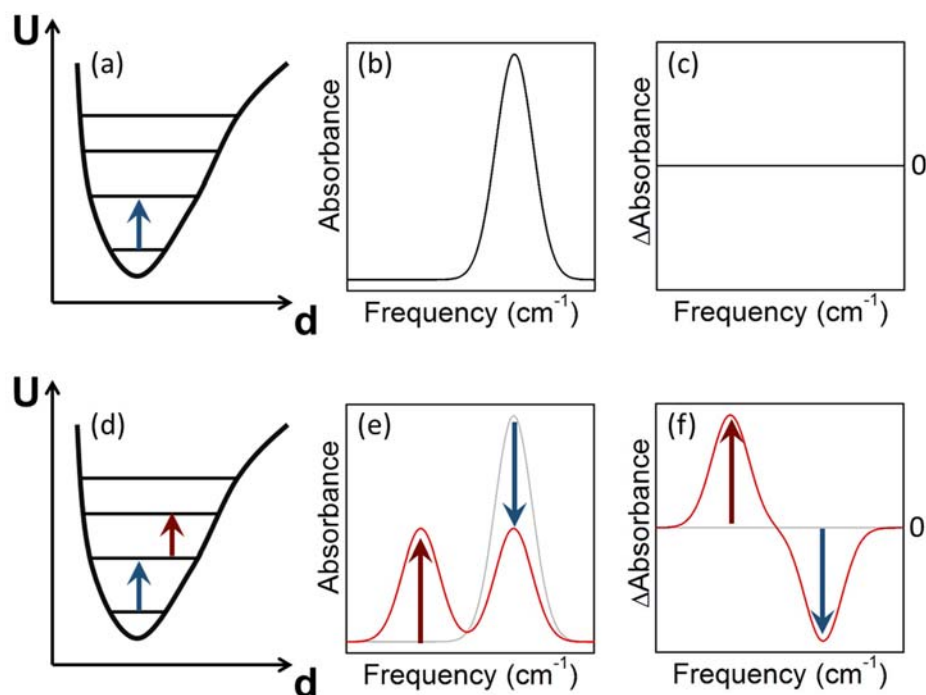


Figure 2.1: The level diagram (a,d), absorbance (b,e), and transient (c,f) spectra of a single anharmonic vibrational mode without (a-c) and with (d-f) the influence of an IR pump pulse.

The pump pulse excites some portion of the sample from the ground state into the first excited state, resulting in a reduced population in the ground state and an increased population in the first excited state. When the probe pulse is transmitted through the sample after the pump pulse, light can be absorbed by either the $0 \rightarrow 1$ or $1 \rightarrow 2$ transition, as shown in Figure 2.1d. In a completely harmonic potential the $0 \rightarrow 1$ and $1 \rightarrow 2$ transitions would occur at the same frequency, but due to anharmonicity the $1 \rightarrow 2$ transition usually occurs at a lower frequency than the fundamental transition, as shown in Figure 2.1e.

2.3.2 Measuring Transient Signals

In the absorbance spectrum, the population change shows up as a decreased absorbance for the fundamental ($0 \rightarrow 1$) transition, and a new absorbance peak at the hot band ($1 \rightarrow 2$) frequency. This change is greatly exaggerated in Figure 2.1e, and is generally a very small effect observed as a 1% or less change in optical density (OD). For this reason, transient measurements are often measured as a difference between the absorbance with and without the pump excitation, which is shown as change in absorbance (Δ Absorbance) in Figures 2.1c (which shows zero change without the pump pulse) and 2.1f. In a difference (Δ Absorbance) spectrum, the transient signal shows up as a negative feature for the reduced absorbance or bleach, and the hot band results in a positive feature for the induced absorbance.

Since these signals are very small, fluctuations in the laser intensity can greatly reduce the signal-to-noise ratio of transient experiments. Long time drifts in the pulse intensity make it difficult to calculate a difference spectrum by measuring separate pumped and unpumped intensities. Instead, a chopper wheel is used to block every other laser pulse in the pump beam, and the difference between adjacent pulses is measured directly, as shown in Figure 2.2.

While this does not eliminate noise from shot-to-shot fluctuations, it greatly improves signal quality by eliminating the effects of long term drifts. Again, looking at this information as a difference in signal enhances the clarity of the signal. This also requires a detection and signal processing method capable of measuring signals at 1 kHz. Lock-in detection is commonly used to do this directly, but software methods of calculating the differential signal are also used.

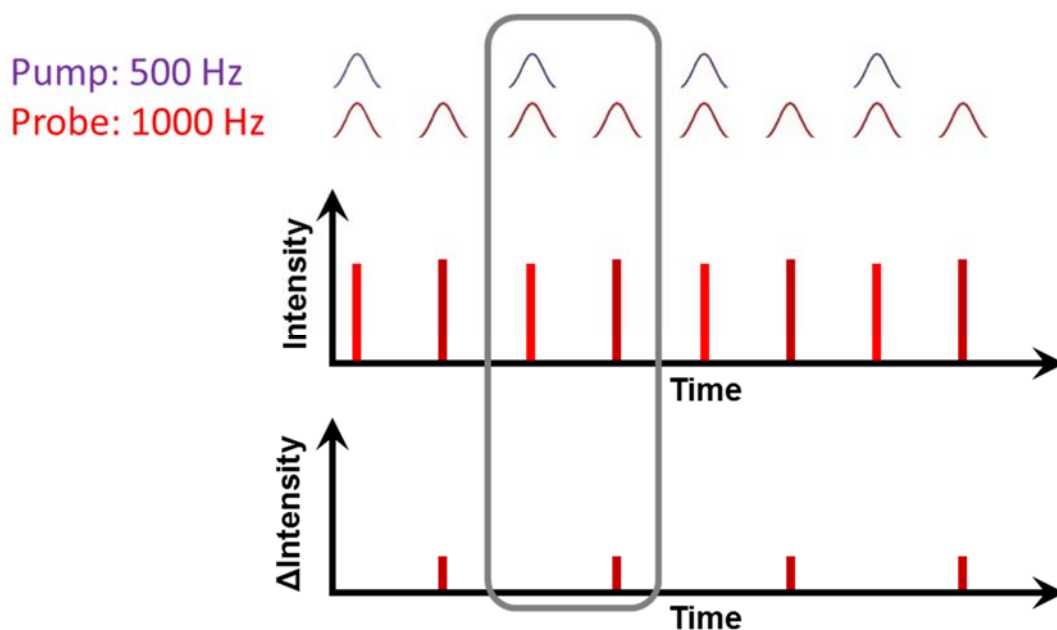


Figure 2.2: Chopping the pump pulse to half of the probe frequency (top) creates adjacent pulses with and without the effect of the pump (middle). The small changes induced by the pump are clearer when viewed as a difference signal (bottom).

2.3.3 Pump-Probe Experimental Design

To measure a transient signal, the pump and probe pulses must be overlapped in space and time, and the time delay between the two pulses carefully controlled. Timing control was discussed in Section 2.3.2. The generation of the probe pulse will be discussed in detail in Chapter 3. A general pump-probe set-up is shown in Figure 2.3, while pulse generation, detection, and other experimental design details specific to our set-up are given in later chapters. The pump pulse is routed through a retroreflector and chopped to obtain a difference signal. Both pulses are focused (which may be done with curved mirrors or lenses, depending on the pulse characteristics) together at or near the sample. In order to guarantee that the probe is measuring an excited portion of the sample, the pump pulse is usually made to be slightly larger than the probe at the overlap. This is often done by focusing the pump pulse behind the sample, but is also dependent on the beam characteristics and parameters of the focusing optic. The probe pulse is then routed to a detector and the signal changes are recorded. The translation stage can be scanned to obtain the signal as a function of time delay to obtain dynamical information, or the signal can be measured at a set delay time to obtain a difference spectrum.

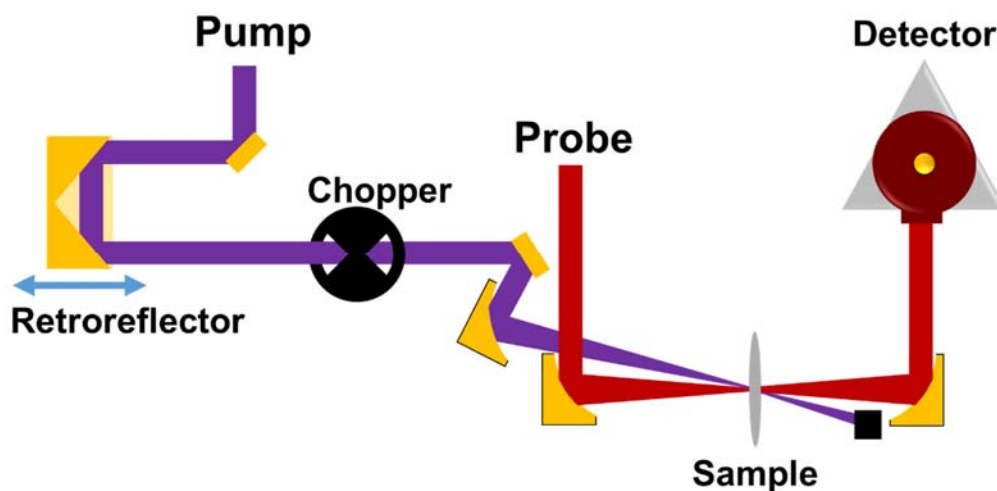


Figure 2.3: A general pump-probe experimental set-up.

2.3.4 Pump-Probe Example: Rhodium Dicarbonyl

Metal carbonyls are strong absorbers in the infrared. Rhodium dicarbonyl (RDC), the structure of which is shown in Figure 2.4, has been studied extensively and is commonly used as a test system for ultrafast vibrational spectroscopy.⁹¹⁻⁹⁵ RDC has a pair of C≡O stretches around 2000-2100 cm^{-1} , shown in the FTIR spectrum in Figure 2.4. The exact frequencies of the peaks vary with solvent,⁹² but in deuterated chloroform, the asymmetric (ν_a) and symmetric (ν_s) C≡O stretches are at 2014 and 2085 cm^{-1} , respectively. A transient IR study of the C≡O stretch dynamics was performed by exciting a 5 mM sample in deuterated chloroform with a pump pulse centered at 2035 cm^{-1} with a bandwidth of about 300 cm^{-1} .

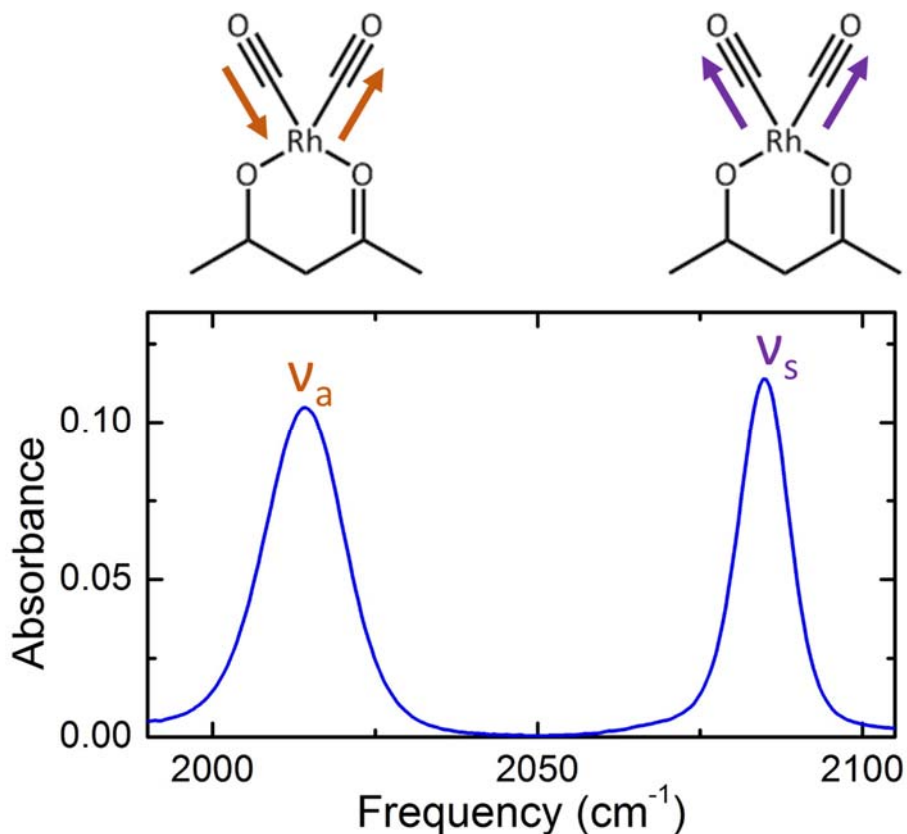


Figure 2.4: RDC structure with C≡O stretches highlighted and the FTIR spectrum of these vibrations.

Transient spectra are measured as the difference between a pumped and unpumped sample at a fixed time delay. The transient spectra in Figure 2.5 were measured at time delays of 1 and 10 ps. Each consists of two reduced absorbances (“bleaches”) at the fundamental transition frequencies of each C≡O stretch, as well as the induced absorbance of the hot band (1→2) transition of each at 1994 and 2075 cm⁻¹, respectively. By comparing the fundamental and hot band frequencies, the anharmonicity of each vibration can be calculated, suggesting that the asymmetric stretch is more anharmonic than the higher frequency symmetric stretch. Additionally, the higher frequency induced absorbance has a shoulder that is not well-resolved. This is due to a combination mode of the symmetric and asymmetric stretches, which will be discussed later.⁹⁴

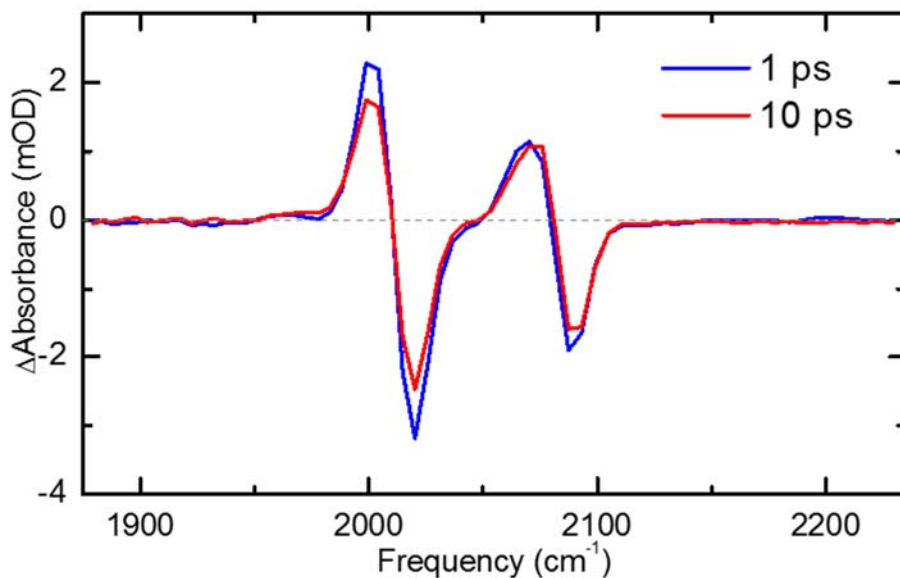


Figure 2.5: Transient spectra of the C≡O stretches of RDC at 1 and 10 ps

Sometimes, spectral diffusion dynamics can cause a frequency shift in the peak as a function of time. In pump-probe spectroscopy, this is observed when the pump intensity varies over the bandwidth of a mode. This can be seen by comparing the transient spectra at multiple time points. If a frequency shift were to occur, the peaks in spectra measured at different time points would be offset. In the case of RDC, the peaks are narrow relative to the pump bandwidth, so spectral diffusion is not observed in the pump-probe.

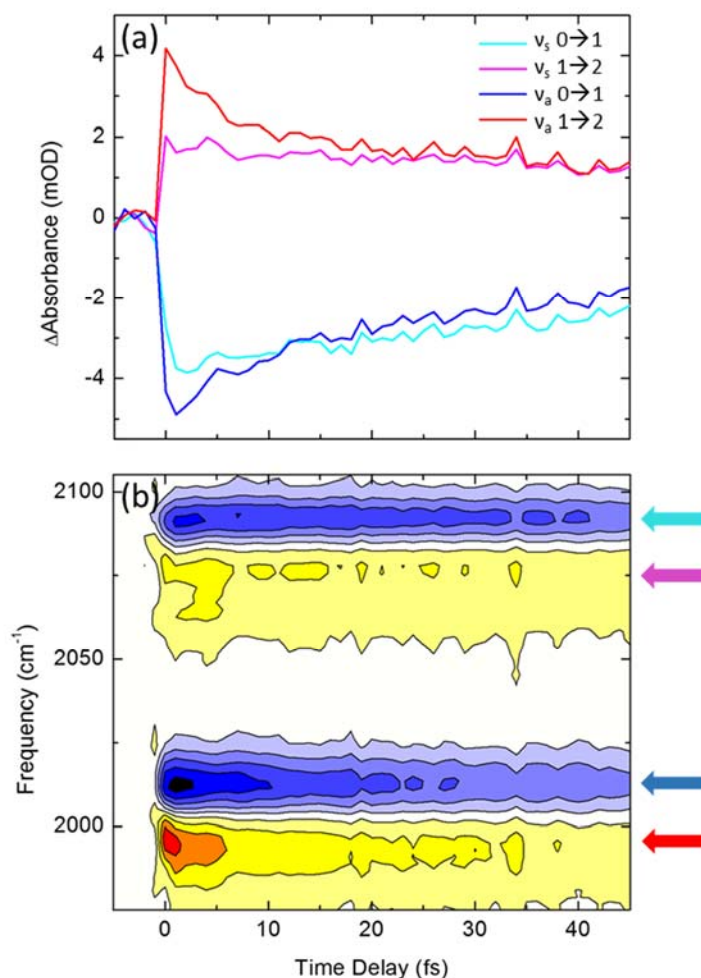


Figure 2.6: Vibrational dynamics of the RDC C \equiv O fundamental and hot band transitions measured at (a) single frequencies and measured as (b) a time-resolved transient spectrum (bottom)

Pump-probe spectroscopy can also be used to study the dynamics of a mode as a function of time delay between the pulses. This is done by scanning the translation stage to vary the pathlength of the pump pulse. In Figure 2.6 above, the dynamics of the two $\text{C}\equiv\text{O}$ stretch fundamental and hot band transitions are shown from -5 ps to 45 ps in steps of 1 ps (equivalent to moving the stage 7.5 mm in steps of 150 μm). Depending on the detection method, which will be discussed in detail in Chapter 3, the dynamics of a single frequency (any one of the four traces in 2.6a) or a section of the spectrum (Figure 2.6b), can be obtained.

2.4 Two Dimensional Infrared Spectroscopy (2D IR)

2.4.1 Introduction to 2D IR Spectroscopy

2D IR reveals vibrational coupling and frequency-resolved ultrafast vibrational dynamics. This method uses time-ordered laser pulses to study the couplings and dynamics of vibrational transitions, as shown in Figure 2.7.^{52,53,96,97} The first pulse (E_1) induces a coherence in the sample, while the second pulse (E_2) arrives at an evolution time τ_1 later and converts the coherence into a population. The third pulse (E_3) probes the resulting vibrational frequency as a function of the waiting time τ_2 . 2D IR spectroscopy can be viewed as transient IR spectroscopy that is frequency-resolved along the excitation axis. As such, it can be used to observe couplings between vibrational modes, as well as heterogeneity, spectral diffusion, chemical exchange, and energy transfer.

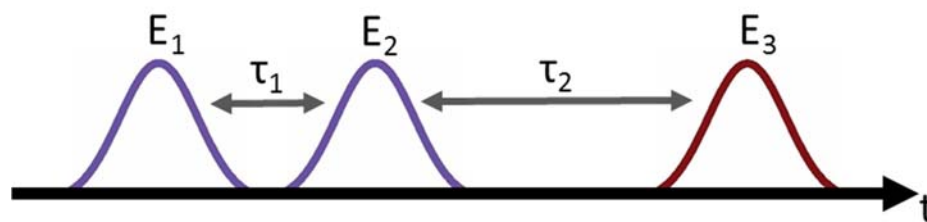


Figure 2.7: Pulse sequence used to measure 2D IR spectra

For simplicity, features of a 2D IR spectrum can be identified by their coordinates in the excitation and detection axes, (ω_1, ω_3) . Each peak of a linear infrared spectrum shows up as a bleach along the diagonal, with equal frequencies in both the excitation and detection axes $(\omega_1 = \omega_3)$. Figure 2.8 shows a model 2D IR spectrum of a single mode. As in the pump-probe spectrum, each fundamental bleach is accompanied by an induced absorbance that occurs at the same excitation frequency but a lower detection frequency due to the anharmonic frequency shift. The lineshape of a diagonal peak provides information about the peak broadening. Round, symmetric peaks result from homogenous broadening, while peaks that are elongated along the diagonal are the result of inhomogeneous broadening due to uncoupled subpopulations within a broader feature. Spectral diffusion can be observed by measuring a series of 2D spectra at multiple values of τ_2 . At early times, the excitation is isolated to individual subpopulations, resulting in an inhomogeneous feature, which evolves into a homogeneous lineshape due to spectral diffusion over a correlation time τ_c .

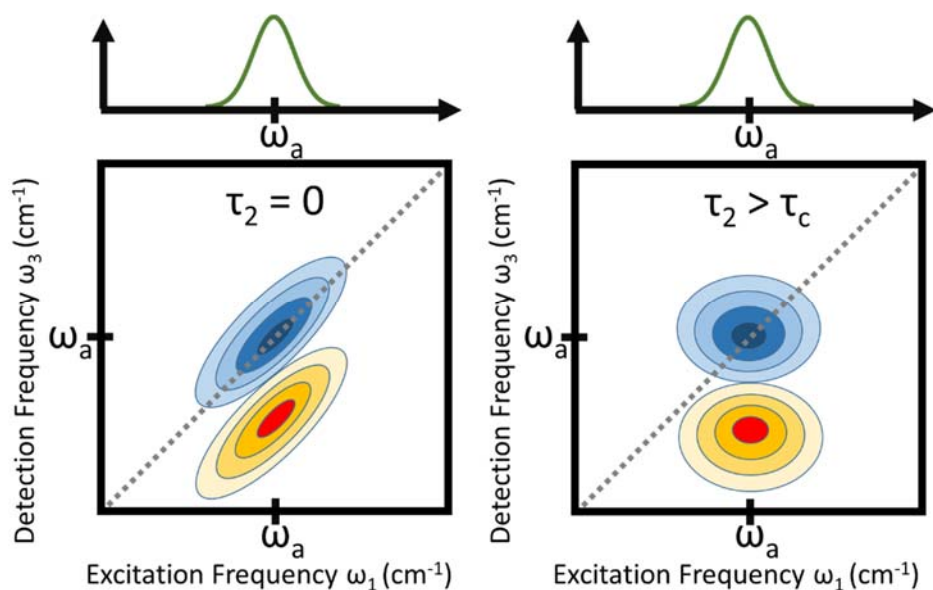


Figure 2.8: An inhomogeneous lineshape at early waiting times (left) becomes homogeneously broadened at later waiting times.

Figure 2.9 shows a simplified model of 2D IR for a system with two vibrational modes. Cross peaks show up at $\omega_1 \neq \omega_3$ when excitation of one vibrational mode causes a response in a different mode. These can be due to vibrational coupling or energy transfer between the two modes. When the pump pulse has created a population in the first excited state, the probe pulse can then be absorbed into the overtone of that mode, or a combination band of that mode and another mode to which it is coupled. Like the $1 \rightarrow 2$ transition, the combination mode occurs as a lower energy than the sum of the two independent modes, which causes a frequency shift in the coupled mode. Alternatively, the absorbed energy can decay by transferring to lower energy states. The difference between these two processes can be observed experimentally from the waiting time (τ_2) dependence of the 2D spectrum. Coupling appears instantaneously (when $\tau_2 = 0$), while energy transfer occurs over some time scale ($\tau_2 > 0$). Spectral diffusion, vibrational coupling, and energy transfer can all occur in real systems, which can complicate the interpretation of 2D IR results.

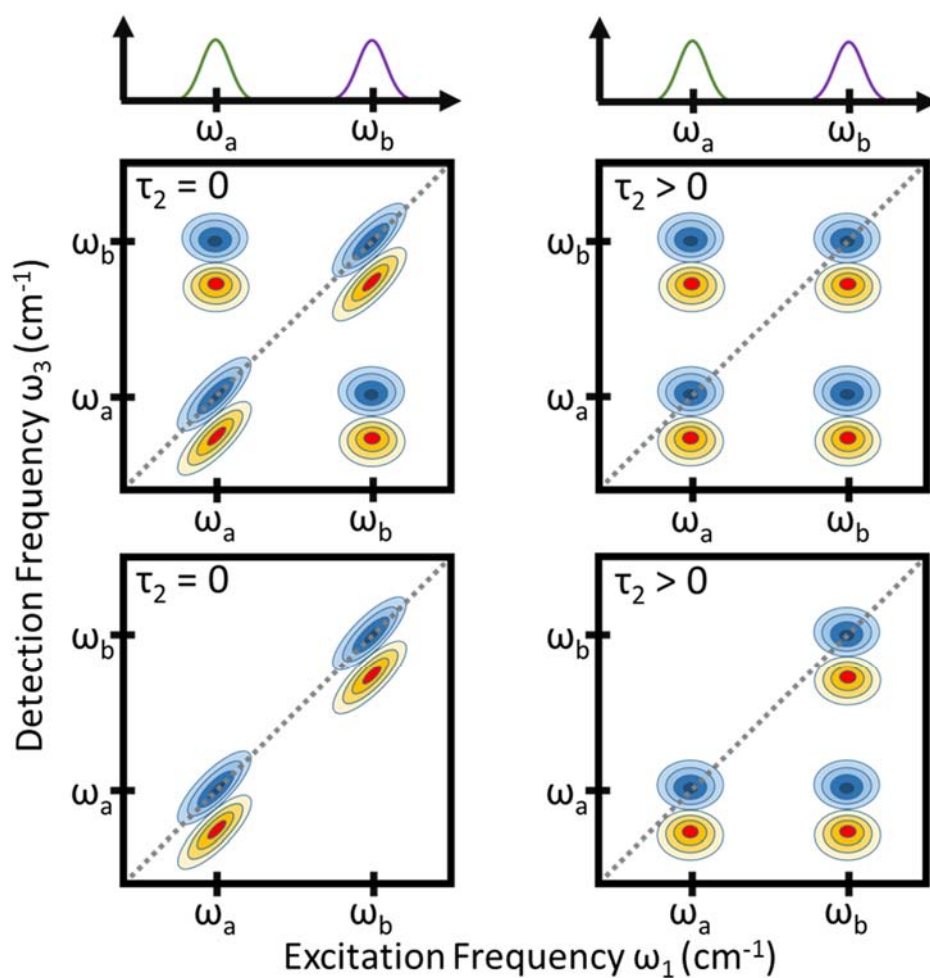


Figure 2.9: Crosspeaks in 2D spectra can be caused by vibrational coupling (top) or energy transfer (bottom). The time evolution of the peaks can be necessary to decipher the two processes.

2.4.2 Examples of 2D IR Spectra

The features described above can be observed clearly in the 2D IR spectra of many dyes. The 2D IR spectra of the thiocyanate (CN) stretch of N749 Black Dye in acetonitrile at waiting times of 0.2 and 5 ps are shown in Figure 2.10, along with the structure and linear absorption spectrum of the CN stretch. Like the schematic spectra shown in Figures 2.8, the diagonal slope of the bleach and induced absorbance are observed becoming more horizontal as a result of spectral diffusion as the waiting time increases.

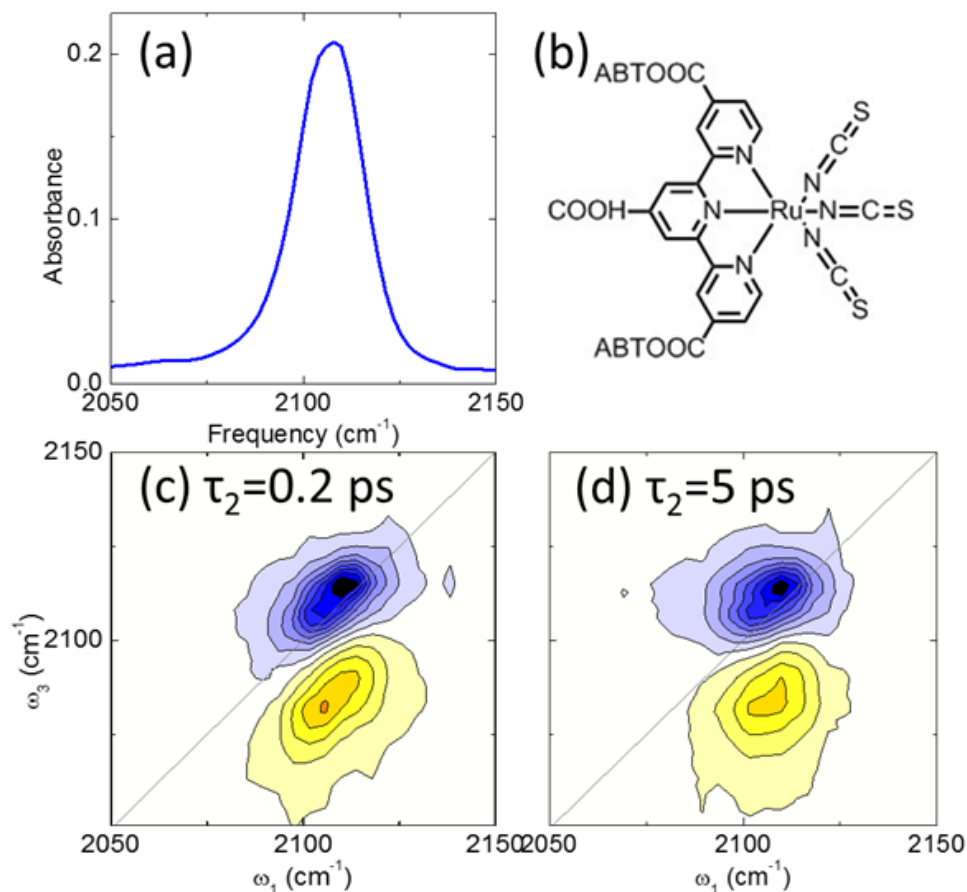


Figure 2.10: Structure (a) and FTIR spectrum (b) of the cyanide stretch of N749 Black Dye, along with the 2D spectra at 0.2 (c) and 5 ps (d), showing spectral diffusion over several ps.

The two coupled modes of RDC described in Section 2.3.4 provide a clear example of vibrational coupling in 2D IR, as seen in Figure 2.11. The dynamics of the C≡O stretch modes are clear from the pump-probes, but coupling between the modes was not observed. These features are illustrated in the 2D IR spectra. Each diagonal bleach is accompanied by an induced absorbance. However, the off diagonal bleaches have induced absorbances that are offset from the expected $1 \rightarrow 2$ transitions in the ω_3 axis. These result from the transition from the first excited state of either stretch into a combination mode, indicated by orange arrows in the level diagram in Figure 2.11. Conversely, measuring dynamics from 2D IR data requires collecting 2D surfaces at various values of τ_2 , which is significantly more complex and time-consuming than measuring pump-probes. (The negative signal along the diagonal in Figure 2.11 is an artifact due to scattered pump reaching the detector.)

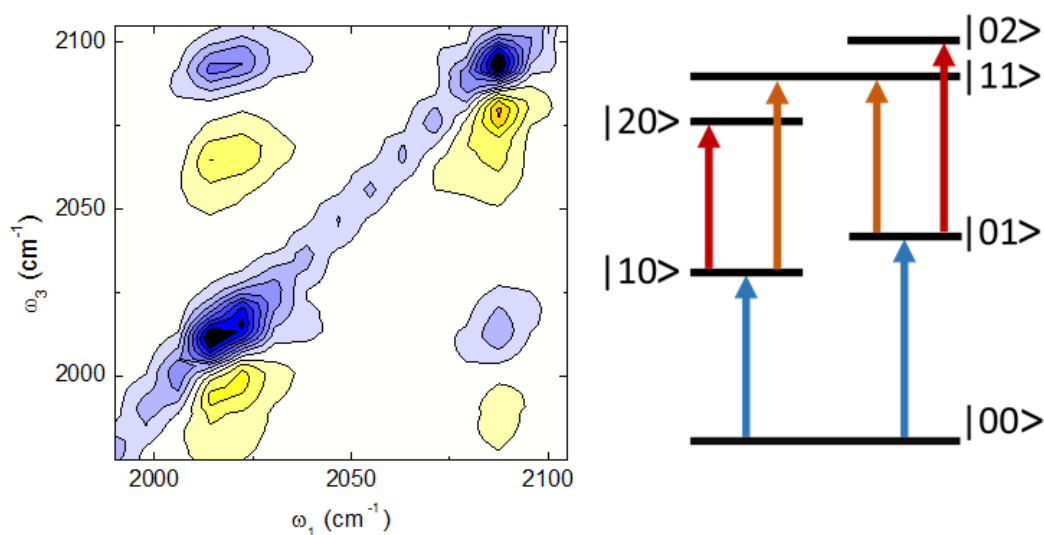


Figure 2.11: The 2D spectrum (left) of the C≡O stretches of RDC, with a noticeable offset in the induced off-diagonal feature, caused by excitation into the $|11\rangle$ mode as showed in the level diagram (right).

2.4.3 2D IR Experimental Design

2D IR spectra were measured in a pump-probe geometry^{97,98}, as shown in Figure 2.12. The generation of the mid-IR continuum probe pulse shown in the diagram is discussed in detail in the next chapter. The mid-IR pump pulse, generated by DFG mixing of the outputs of an OPA as described in Section 2.2.1, is split into two pulse pairs with a Mach-Zehnder interferometer. One pulse of each pair is chopped at 500 Hz, and the relative time delay between the two pulses is controlled with a translation stage, which is scanned to obtain coherence time, τ_1 . One pulse pair is directed to the surface-specific 2D-SFG experimental set-up, and the other is used for 2D IR measurements. This pulse pair is sent through a retroreflector on a second linear translation stage to control the waiting time τ_2 and then focused with an off-axis parabola ($f=152$ mm, protected gold, Thorlabs) and crossed with the probe pulse at the sample. This pulse pair is sent through a retroreflector on a second linear translation stage to control the waiting time τ_2 and then focused with an off-axis parabola ($f=152$ mm, protected gold, Thorlabs) and crossed with the probe pulse at the sample.

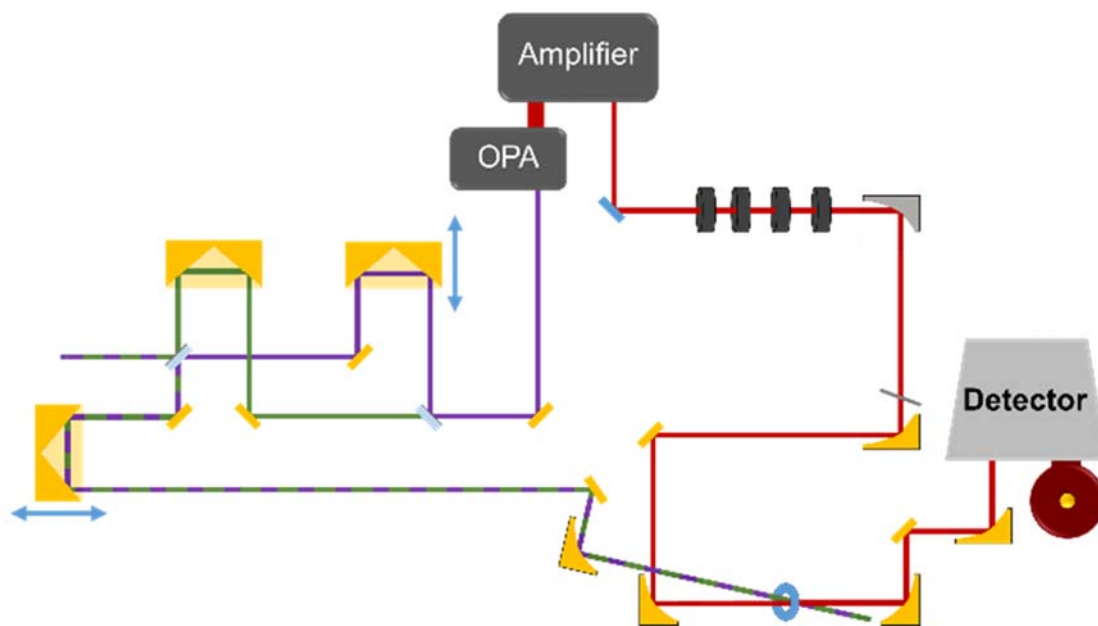


Figure 2.12: The experimental set-up for 2D IR experiments. The pump (purple) beam is generated by an OPA and split into two pulse pairs in a Mach-Zehnder interferometer. The continuum probe (red) is crossed with the pump at the sample and then recollimated and dispersed onto an MCT array detector.

In this experimental geometry, transient IR measurements can be performed by blocking one pulse of the pair and using only the chopped pulse. Since this pulse is not on a translation stage in the interferometer itself, the delay time between pump and probe is controlled by the stage that sets the waiting time. In our experiments, the detection axis ω_3 is measured directly by dispersing the probe pulse onto an array detector. This experimental design was used for the RDC spectra discussed above and the 7AI—Ac pump-probes and 2D IR experiments presented in Chapters 5 and 6.

CHAPTER 3

ULTRAFAST MID-INFRARED CONTINUUM PULSES

3.1 Overview

While ultrafast visible spectroscopy typically utilizes continuum visible pulses to probe photoinduced spectral changes across the whole visible spectrum in a single laser pulse, ultrafast IR spectroscopy is traditionally carried out using femtosecond pulses generated in optical parametric amplifiers (OPAs). These pulses are typically limited in bandwidth to about $100\text{--}500\text{ cm}^{-1}$ in a single laser shot, making observation of the full vibrational spectrum difficult.^{99–103} Scanning the probe pulse across the vibrational spectrum is possible, but this is time-consuming process and introduces additional technical difficulties such as drifts in the beam pointing and timing.^{75–77}

Recent developments in the generation of broadband continuum mid-infrared (CIR) pulses have enabled probing the entire vibrational region (<1000 to $>4000\text{ cm}^{-1}$) with a single laser pulse for transient and 2D IR spectroscopies. In a 2012 *Optics Letters* publication, we demonstrated the first implementation of the continuum pulse in transient spectroscopy in pump–CIR probe experiments,⁷⁹ and numerous ultrafast spectroscopic studies have since been undertaken with this technique.^{67,85–90,104} Further optimization of the CIR generation continues to facilitate its implementation in a wide range of applications.

3.2 Background

Broadband terahertz pulses have been generated by filamentation of 800 and 400 nm femtosecond laser pulses in air for several decades.^{105–107} In 2007, Fuji and Suzuki¹⁰⁸ extended the continuum pulses into the mid-IR by using 25 fs laser pulses and reflective optics to limit dispersion. Petersen and Tokmakoff¹⁰⁹ extended the two-color generation scheme to a three-color scheme by simultaneously focusing 800, 400, and 267 nm pulses collinearly in air. This is the method we have adopted, which is described in detail in section 3.3. The inclusion of the 267 nm pulse results in about a 10-fold increase in the power of the continuum pulse relative to the two-color scheme and the compact collinear geometry minimizes the pulse-to-pulse power fluctuations, making it possible to use the continuum source as a probe pulse in transient IR spectroscopy. This prospect stimulated several groups to pursue mid-IR continuum generation in various geometries and conditions. Khalil and co-workers¹¹⁰ studied the effect of the gas medium in continuum generation using the two-color scheme and Fuji et al¹¹¹ recently reported very short and energetic continuum pulses using the two-color scheme. The Tokmakoff^{48,85–89} and Zheng^{77,90} groups have also incorporated the mid-IR continuum into 2D IR experiments, while Shirai et al¹⁰⁴ have demonstrated its use in transient reflectivity studies.

3.3 Generation of Ultrafast Mid-Infrared Continuum Pulses

3.3.1 Experimental Design

Mid-infrared continuum pulses are generated by collinear mixing of first, second, and third harmonics of 1 mJ, 25 fs, 800 nm pulses generated by a Ti:Sapphire

amplifier (Coherent Legend Elite Duo). The fundamental pulse is propagated through a series of nonlinear crystals and other optics in four stages to generate the second and third harmonics and to control the polarization and timing of each component. These four stages are shown schematically in Figure 3.1 and described in detail below.⁷⁹

- (I) The starting pulse is linearly polarized horizontally and doubled in a Type I BBO (10x10x0.1 mm, $\theta=29.2^\circ$). The generated second harmonic is 400 nm and perpendicularly polarized.
- (II) The first and second harmonics are transmitted through a delay plate to control the temporal walk-off between the two wavelengths. This results in a temporal delay of approximately 300 fs that pre-compensates for dispersion in the third and fourth optics. Earlier experiments used a BBO delay plate (Type I, 10x10x3 mm, $\theta=66^\circ$), while a calcite crystal has been used more recently.
- (III) The temporally separated pulses are transmitted through a dual wavelength waveplate (quartz, 0.584 mm thick, 6.5λ at 800 nm, 14λ at 400 nm), which controls the relative polarization of the two harmonics. After transmission through these optics, the polarization of the second harmonic pulse is 45 degrees relative to the fundamental.
- (IV) The fourth crystal is a BBO crystal (Type I, 10x10x0.05 mm, $\theta=44.3^\circ$) supported on a silica substrate. After passing through the substrate, the first and second harmonics are temporally overlapped in the BBO and summed to generate the third harmonic at 267 nm. The third harmonic is perpendicular to the fundamental and 45 degrees relative to the second harmonic. This allows components of all three pulses to interact.

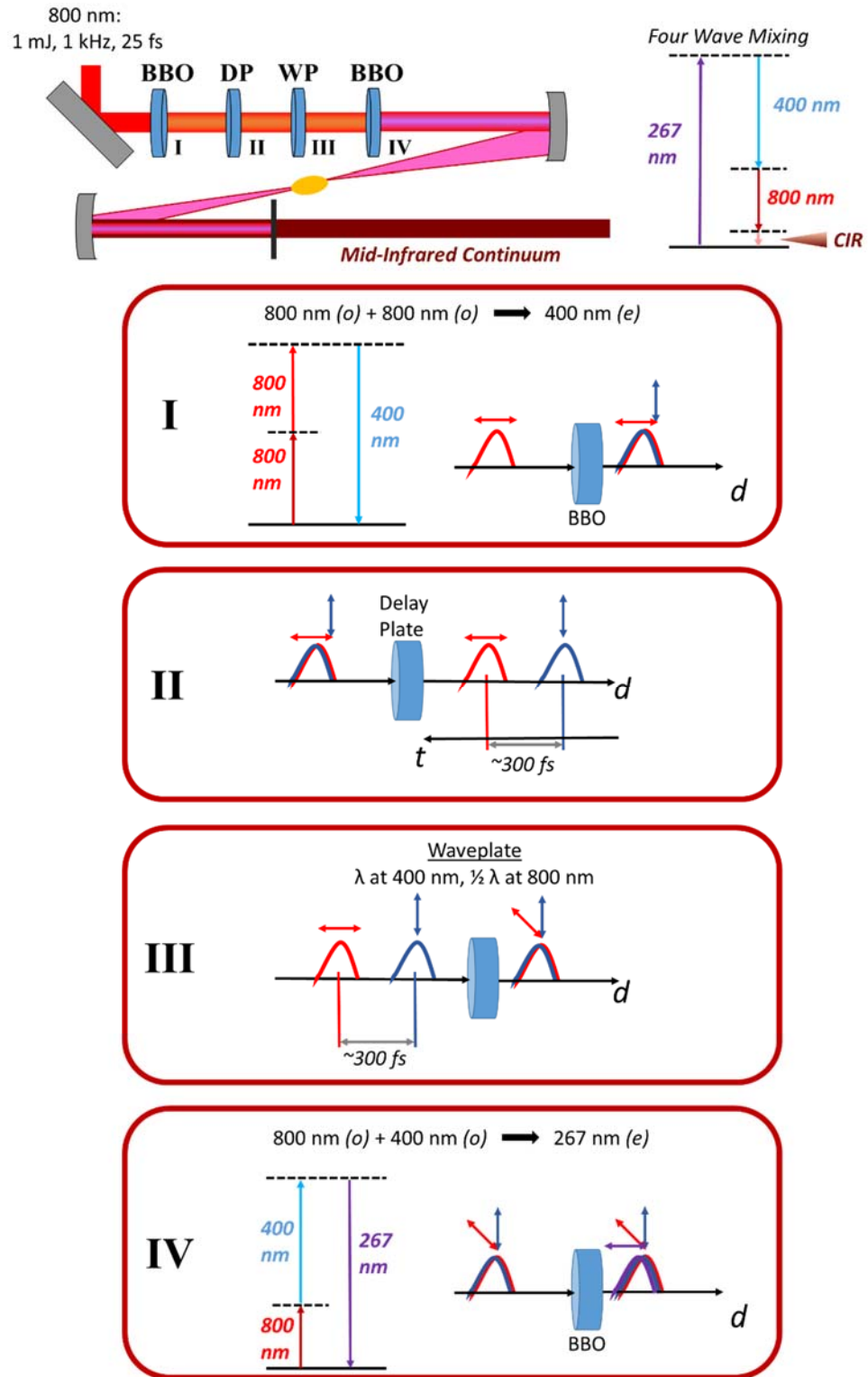


Figure 3.1: Schematic of the generation of the ultrafast, mid-IR continuum pulse by nonlinear mixing of the first, second, and third harmonics of a 25 fs, 800 nm pulse.

The three harmonics are focused together in air to generate a plasma. Four-wave mixing of the three harmonics in the plasma results in the generation of the mid-IR continuum. The initial experimental design used a 1 m focal length spherical mirror to focus the harmonics and a 0.5 m spherical mirror to recollimate the beam.⁷⁹ More recently, 90 degree off-axis parabolas have been used to focus the harmonics ($f=152$ mm, UV-enhanced aluminum, Thorlabs) and recollimate the CIR pulse ($f=152$ mm, protected gold, Thorlabs). The generated CIR pulse is vertically displaced from the three harmonics. With the long focal lengths, this displacement could be used to separate the CIR spatially. When using the shorter focal length parabolas, however, a filter is necessary to separate the CIR from the harmonics. Generally, a 500 μm , uncoated silicon wafer is used to reflect the harmonics and transmit the CIR. This results in a significant reflection loss of the CIR. The uncoated silicon was recently replaced with a 500 μm thick silicon wafer with a broadband anti-reflection coating, which increases the transmitted IR energy to a measureable value of about 700 nJ.

3.3.2 Alignment

The collimated CIR pulse is not intense enough to see on thermal paper or a pyroelectric infrared camera (Pyrocam III, Ophir). The infrared camera is capable of detecting the focused CIR spot. The beam path from the amplifier through the CIR generation and to the array detector is shown in Figure 3.2. To align the CIR beam path, the fundamental 800 nm pulse is used as a tracer beam. Although the generated continuum is displaced from the 800 nm beam, this provides a good starting point and ensures the CIR optics are aligned correctly. The beam must make several long jogs in order to match the path length to that of the OPA that generates the pump pulse.

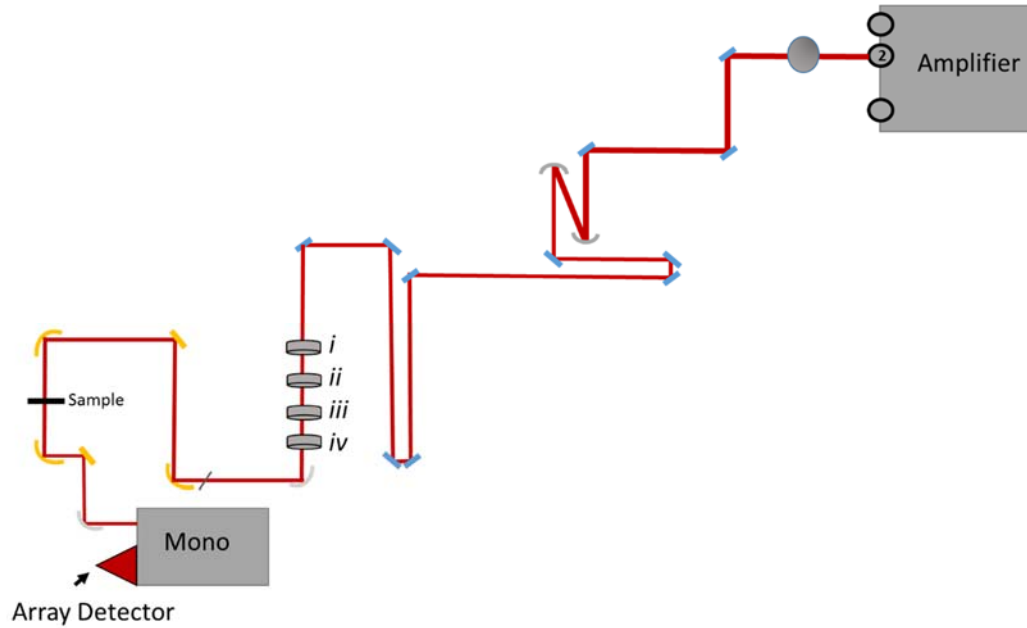


Figure 3.2: Beam path of CIR generation from the amplifier to the detector

To avoid damage to the optics from the intense 800 nm pulse, a variable neutral density (ND) filter (Newport, 2 mm thick UV-fused silica, OD 0-4) is placed at the beginning of the beam path and the OD is increased until the 800 nm spot is barely visible. The CIR generation optics are removed, and the 800 nm beam is centered on all optics up to the entrance slit of the array detector. The entrance slit must be closed to prevent damage to the sensitive detector elements and electronics. Once the 800 nm beam has been aligned, the four generation optics are put in at the optimal positions. The silicon filter is placed back in the beam after the focus, blocking the 800 nm pulse and harmonics from reaching the array detector. The intensity of the 800 nm beam is increased gradually by decreasing the OD of the variable ND filter. As the intensity increases, the filament can be seen and heard. Although the CIR is slightly displaced, it generally does reach the detector. This pointing of the displaced CIR beam can be

optimized by maximizing the signal on the array detector with the pointing of the focusing parabola. The signal intensity can be further optimized by tuning the crystal angles, pulse compression, and pointing.

3.4 Detection

3.4.1 Single Element Detection

Detecting a broadband mid-infrared continuum presents numerous technical difficulties. While visible detectors such as CCD cameras are readily available, state of the art infrared detectors are costly and generally limited to arrays of 128 detector elements. Work utilizing infrared focal plane arrays of 128 x 128 pixels is in its infancy.^{112,113} Baiz and Kubarych¹¹⁴ demonstrated the use of upconversion detection to probe a part of the continuum IR pulse (1800–2600 cm⁻¹) using a visible CCD, but the upconverted bandwidth is generally limited by the phase-matching conditions of nonlinear crystals. Fuji and coworkers^{115,104} demonstrated broadband upconversion in gases that removed this limitation. Our earliest experiments were detected by scanning a monochromator and using a single element mercury-cadmium-telluride (MCT) detector. Figure 3.3 shows the CIR spectrum measured by scanning each of three gratings and detected with a single element MCT detector, as well as the spectrum measured interferometrically with a commercial FTIR spectrometer. Scanning the monochromator to each individual frequency point is time-consuming, especially for time-resolved experiments, and limits both the temporal and spectral resolution obtainable in a reasonable amount of time.

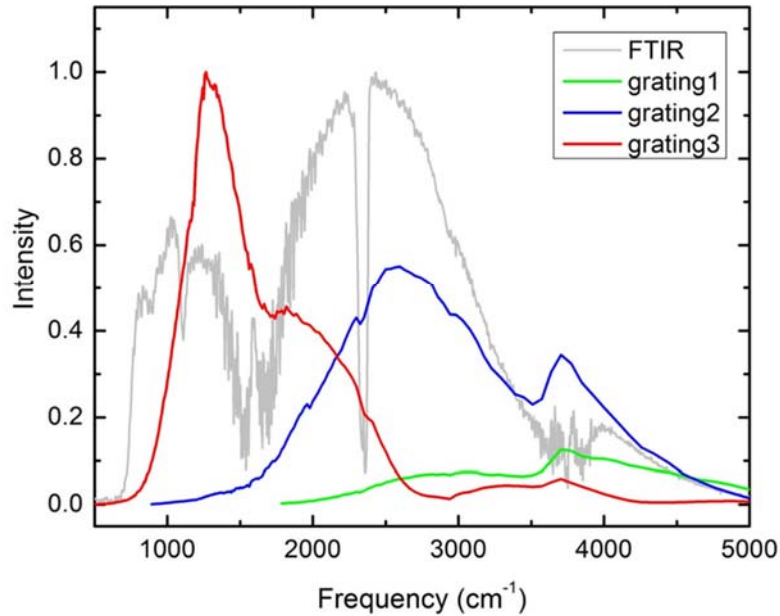


Figure 3.3: The CIR spectrum measured on a single element MCT detector by scanning each of three gratings, and measured interferometrically with a commercial FTIR spectrometer.

3.4.2 Array Detector

We have since acquired an infrared array detector (Infrared Systems/Infrared Associates), which contains 128 MCT elements divided into two rows of 64 pixels each. The elements are doped for highest response at 10 μm , giving an overall spectral response range of approximately 2 to 13 μm . An infrared monochromator (Horiba) is used to disperse the CIR pulse onto the array. The monochromator is equipped with three gratings, the specifications of which are given in Table 3.1.

Table 3.1: Horiba Monochromator Grating Specifications

Grating number	Grooves per mm	Blaze wavelength (μm)	Resolution (nm)	Resolution (cm^{-1} at 10 μm)	Resolution (cm^{-1} at 5 μm)	Resolution (cm^{-1} at 2.5 μm)
0	150	4.0	5.13	0.5	2.1	8.2
1	58	3.6	13.27	1.3	5.3	21
2	30	8.0	25.63	2.7	10	41

The transient spectra of RDC (discussed in Chapter 2) measured on each of the three gratings at time delays of 1 and 10 ps are shown in Figure 3.4. While the four main features of the RDC C≡O stretches are not well-resolved on grating 2, the high resolution of grating 0 resolves not only these four features but also the smaller ($\nu_a+\nu_s$) combination mode at $\sim 2060\text{ cm}^{-1}$. Each transient spectrum is measured at a single grating position, so these plots also represent the frequency range obtainable on each grating. While grating 0 offers the best resolution, it would also require the most grating positions to measure the full continuum spectrum, resulting in the longest acquisition time. This can be determined from the “grooves/mm” in the grating specifications. The highest resolution grating (grating 0) is five times more dispersive, resulting in a bandwidth that is about 20% of the least dispersive grating (grating 2). The resolution of each grating is constant in wavelength due to the diffractive optics, causing it to decrease with increasing frequency.

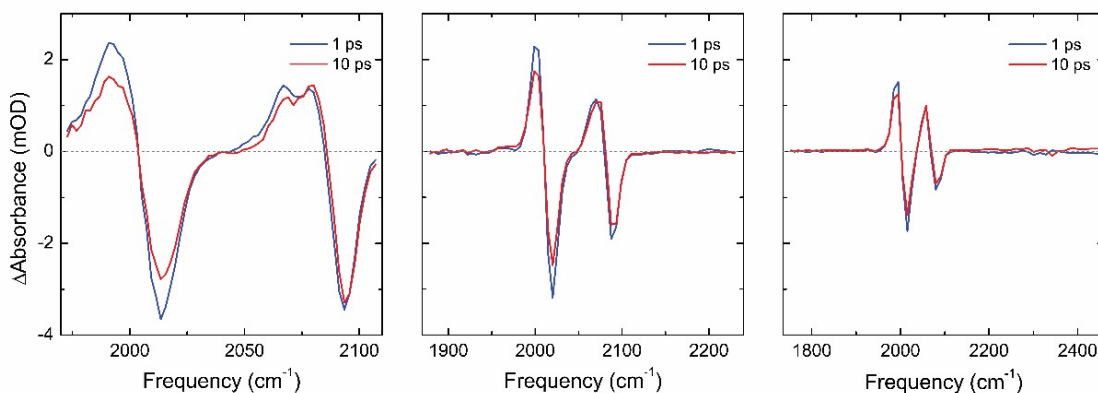


Figure 3.4: Transient spectra of RDC measured on each of the three spectrometer gratings. From left to right, the bandwidth increases while the resolution decreases.

The use of diffraction gratings for broadband pulses introduces an additional experimental consideration due to the presence of multiple diffraction orders. For example, the first order diffraction of 8000 nm occurs in the same direction as the second order 4000 nm or fourth order 2000 nm. Since the CIR pulses cover several octaves (from <2500 nm to >10000 nm), we have equipped the monochromator with four filters that allow us to isolate a single order of the spectrum from 2440 to 13000 nm. The filters are contained in a motorized 6-slot filter wheel. One of the remaining slots contains a 1 mm thick uncoated silicon wafer, and the last slot remains empty. The spectrum measured on the two regularly used gratings is shown in Figure 3.5. The measured spectrum is highly dependent on the individual grating efficiency. The sharp high frequency cut-off at about 4000 cm^{-1} is from the highest frequency filter, a longpass filter that only transmits wavelengths longer than 2440 nm.

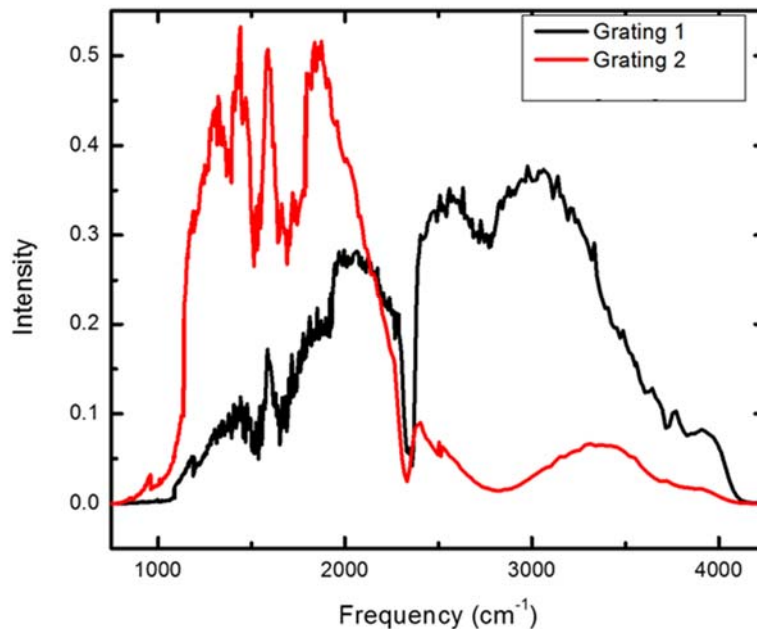


Figure 3.5: CIR spectrum measured on the MCT array detector after being dispersed by grating 1 and grating 2.

The spectral resolution of the commercial FTIR in Figure 3.3 and the array detector in Figure 3.5 allows for well resolved atmospheric absorbances of CO₂ and water vapor at 2350 cm⁻¹ and ~1600 cm⁻¹, respectively, while these absorbances are blurred significantly when measured on the single element detector in Figure 2. While the gratings could be scanned in smaller steps to achieve higher resolution in these spectra, doing so would greatly increase the acquisition time.

3.5 Characterization of Mid-IR Continuum Pulses

3.5.1 Pulse Characterization Methods

The temporal characterization of the CIR pulses is complicated by the bandwidth of the pulse itself. Typically, ultrafast pulses can be characterized by mixing the unknown pulse with a well-characterized pulse. We previously determined the temporal duration of the pulses with two methods. A portion of the CIR pulse was characterized by cross-correlation, frequency-resolved optical gating in a MgO:LiNbO₃ crystal (15×15×0.2 mm, $\theta=48^\circ$, $\phi=30^\circ$). This method uses a second, well-characterized laser pulse, in this case approximately 35 fs, 700 nm pulses generated by doubling the signal output of the OPA, to upconvert the infrared pulse. Only a portion of the CIR spectrum can be characterized with this method, however, since phase matching limitations of the crystal prevent the upconversion of the full bandwidth of the continuum pulses. An alternative method of characterizing the CIR is cross-correlation in germanium with approximately 35 fs, 1830 nm idler pulses. The results of those cross-correlations from 1000 to 4000 cm⁻¹ indicate a pulse duration ranging from 110 to 160 fs, with a small chirp of about 50 fs, across the spectrum, shown in Figure 3.6.⁷⁹ Cross-correlations in germanium provide an upper limit for the temporal resolution of CIR probe experiments and will be discussed further below.

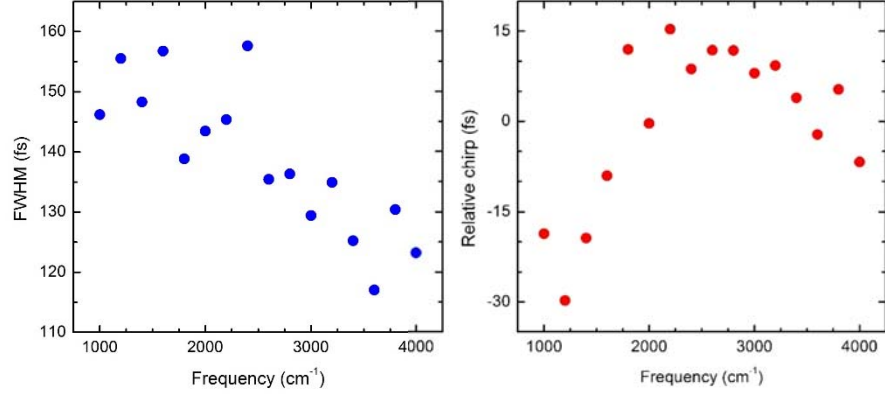


Figure 3.6: Pulse duration and spectral chirp of the CIR pulse obtained from the cross-correlation in germanium.

3.5.2 Temporal Resolution and Dispersion

Due to the large bandwidth of the CIR pulse, it is highly susceptible to dispersion in materials. Limiting transmission through material is necessary to maintain the short duration of the CIR pulses. The silicon filter used to remove the three harmonics and the sample windows all introduce temporal walk-off due to the group velocity dispersion. Carefully selecting the optics in the beam path minimizes these effects.

The temporal resolution of our experiments can be determined by cross-correlations in a semiconductor, which is a featureless pump-probe experiment in which a pump pulse excites a free carrier from the valence band to the conduction band of the semiconductor, as shown in Figure 3.7a. The high density of states in the conduction band results in a broadband IR absorbance following the pump excitation. In the cross-correlation shown above, a pump pulse of 1830 nm, corresponding to the bandgap of germanium, was used. Scanning the time delay between the pump and probe results in an error-function-shaped induced absorbance of the CIR pulse, as seen in Figure 3.7b.

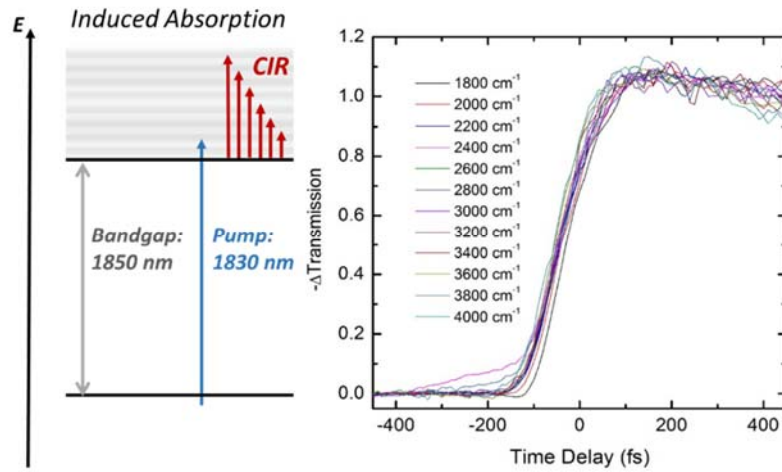


Figure 3.7: Schematic (left) and results (right) of a cross correlation between an 1830 nm idler pulse and the CIR in germanium.

This function is the convolution of the pump and probe durations with the instantaneous free carrier generation. The convolution of the pump and probe pulses is the temporal resolution of pump-probe experiments, and if one of the pulse durations is well-characterized as above, the temporal duration of the other pulse can be determined. The temporal duration of the probe pulse could be decreased to less than 50 fs by compressing the probe pulse using a pulse shaper.^{116,117}

However, germanium is also susceptible to multi-photon absorption, so that two or more photons of a longer wavelength can also be used to excite free carriers. We have observed this process to occur with pump pulses as long as 8000 nm, which requires five photons to jump the bandgap. In the other extreme, excitation with shorter wavelengths can excite multiple free carriers. The decay of the multiple excitons can be observed as a deviation from the expected step function cross-correlation. As a result, the cross-correlation can be used at any pump frequency to find the zero timing (when the pump and probe are overlapped) and upper limit of the temporal resolution. Since the pulse is stretched in the germanium itself, the true pulse duration is likely less than our measured values. With the incorporation of the array detector, this has provided a useful tool for characterizing the experiment.

At low frequencies, the CaF₂ sample windows add significant temporal dispersion. At the high frequency end, the germanium itself stretches the pulse. Similarly, the silicon filter adds a small amount of dispersion to cross-correlations. Since the germanium is not used during experiments, the temporal duration and chirp determined by these cross correlations are upper limits for the actual pulse. While the silicon filter is necessary, its thickness can be reduced to minimize its contribution to the dispersion. For most applications, it is necessary to use windows to contain the sample, but the window material and thickness can be selected to minimize dispersion in the spectral region(s) of interest.

3.6 Applications in Ultrafast Spectroscopy

3.6.1 Pump-CIR Probe Spectroscopy

The CIR pulse described in this chapter has numerous applications in ultrafast spectroscopic methods described in Chapter 2. The huge bandwidth of the pulse allows pump-probe and 2D IR experiments to be performed across nearly the entire vibrational spectrum with a single laser pulse. The inclusion of this pulse in ultrafast experiments was first demonstrated in an IR pump-CIR probe study of the carbonyl stretches in RDC. This shows the application of the CIR pulse in a well-understood system, but does not highlight the benefit of the broad bandwidth. As shown in Figure 3.8, the CIR pulse is ideal for studying the very broad vibrational spectra of hydrogen-bonded dimers, which was first demonstrated in the 7AI—Ac heterodimer using the single element detection method described in section 3.4.1.⁷⁹ The results of that study are discussed in detail in Chapter 4. Using an array detector, that first ultrafast CIR experiment was expanded into a comprehensive pump-probe and 2D IR study of the heterodimer, which is presented in Chapters 5 and 6, respectively.

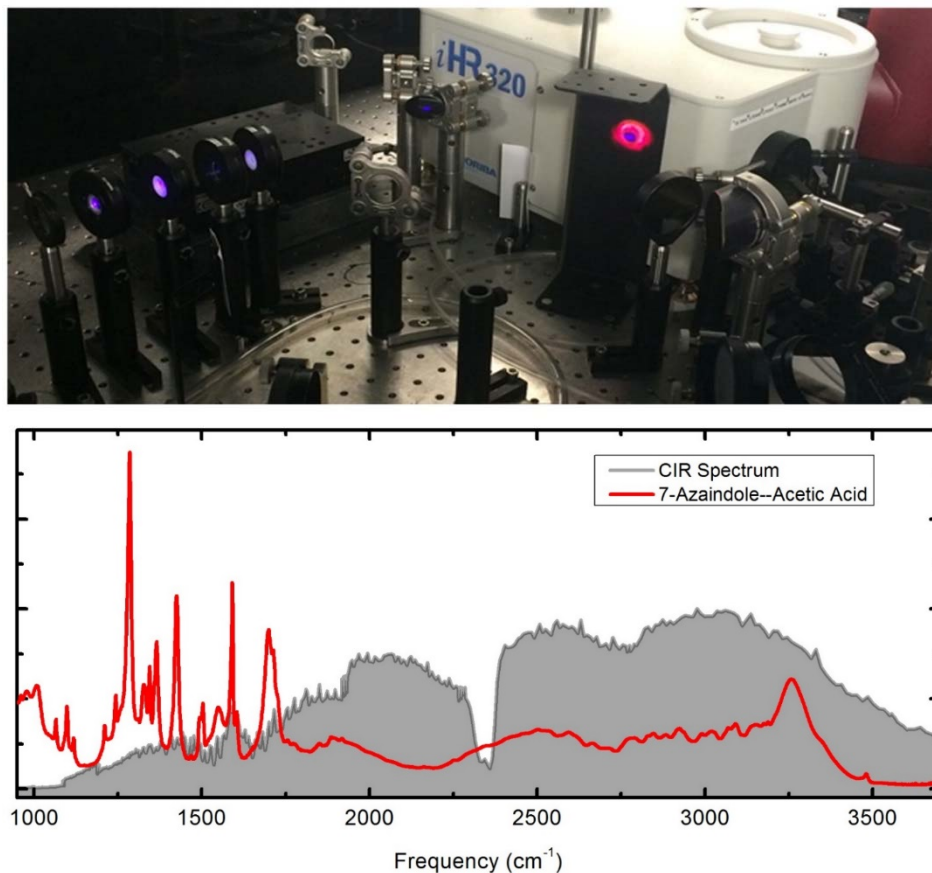


Figure 3.8: Photograph of the CIR generation (top) and the CIR spectrum with the 7AI-Ac heterodimer spectrum (bottom).

3.6.2 Probing the Full Vibrational Spectrum with 2D IR

The advantages of using continuum pulses for 2D IR experiments are illustrated in Figure 3.9. In a typical 2D IR spectrum, the pump and probe pulses are both generated with OPAs, resulting in ω_1 and ω_3 axes of several hundred cm^{-1} . Usually, a single OPA is used to generate the pump and probe pulses. This often limits the spectrum to a single mode or a few modes at the most, as seen in the RDC and N749 Black Dye spectra in Chapter 2. A second OPA can be used to study cross peaks by using different pump and probe frequencies, but this is still limited to a region of several hundred cm^{-1} in each axis. For hydrogen-bonded dimers, these pulses often cover much less than the

bandwidth of the very broad spectrum, preventing the observation of potentially important features. Additionally, induced features can be difficult to predict (as seen in the pump-probes), which makes choosing a probe wavelength less clear. Full spectrum experiments can be done by scanning both OPAs to build up a complete picture, but this is technically complex and time-consuming.^{76,77} In the schematic in Figure 3.9, the observable 2D spectrum using OPA pulses is represented by a single square. Covering the spectrum from 1000 to 4000 cm^{-1} in this manner would require 6 pump frequencies and 6 probe frequencies (assuming pulse bandwidths of 500 cm^{-1}), a total of 36 separate 2D surfaces.

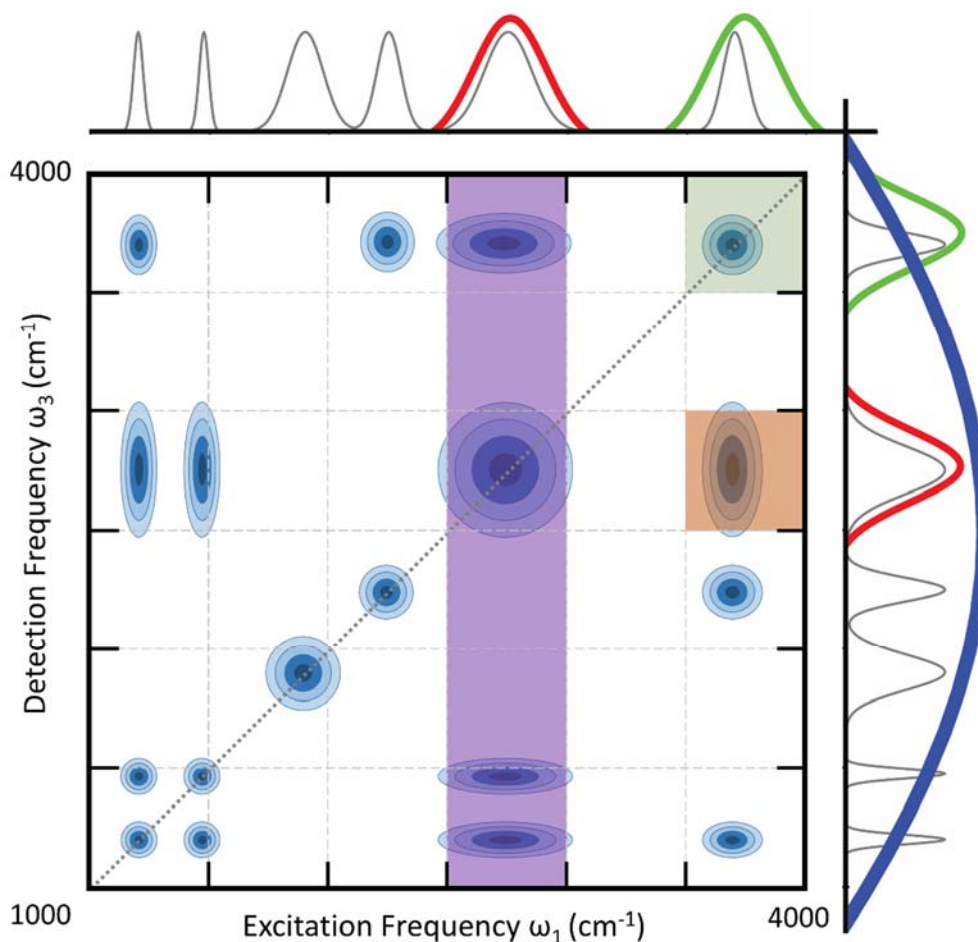


Figure 3.9: Schematic of 2D IR, showing the portion of the spectrum that can be measured with OPA pulses in a one-color (green) or two-color (orange) geometry, and the 2D spectrum measurable with an excitation pulse generated by an OPA and the CIR probe pulse (purple).

Using the CIR probe results in a detection axis that can span from less than 1000 to more than 4000 cm^{-1} in a single experiment, revealing couplings between the directly excited vibration and the rest of the vibrational spectrum. A more complete picture of vibrational coupling can be obtained with 2D IR experiments using a continuum probe and multiple pump frequencies, which would require six experiments to cover the range in the schematic above. Currently, CIR pulses do not have high enough pulse energies to be used as excitation pulses. The development of such pulses, which have the potential to facilitate full spectrum 2D IR in a single experiment, will be discussed in Chapter 8.

CHAPTER 4

MID-IR CONTINUUM SPECTROSCOPY OF THE 7-AZAINDOLE—ACETIC ACID HETERODIMER

4.1 Overview

As discussed in Chapter 1, cyclic hydrogen-bonded structures are common and important in biological systems, where they provide structural stability and mediate proton transfer. Prior to studying the mechanism of proton transfer across hydrogen-bonded interfaces, novel ultrafast continuum mid-IR spectroscopy was used to study the vibrational dynamics of the ground state 7AI—Ac heterodimer, a model system for asymmetric cyclic hydrogen-bonded structures. The structure and vibrational spectrum of this dimer was described in detail in Chapter 1 (Figure 1.3). In this initial study, the OH stretch centered at 2500 cm^{-1} was excited with a 300 cm^{-1} broad, 50 fs mid-IR pump pulse. The spectral and temporal resolution and signal-to-noise of this experiment were limited by the detection method, which has since been improved. As such, only the high-frequency portion (1650 cm^{-1} to 3400 cm^{-1}) of the spectrum was probed with the CIR probe pulse. The results of this study were published in *the Journal of Physical Chemistry B*.⁶⁷

Within the time resolution of the experiment, excitation of the acetic acid OH stretch results in a transient response in both OH modes of the acetic acid monomer and the NH stretching mode of the 7AI monomer. The response of the NH stretch, which is 750 cm^{-1} higher in energy, indicates that the two monomers are strongly coupled across

the hydrogen-bonded interface. The strong coupling of these modes is further supported by their common decay times of approximately 2.5 ps. The strong intermolecular coupling and rapid energy dissipation throughout the asymmetric dimer is likely a general property of cyclic hydrogen-bonded structures. Understanding the ground state dynamics and couplings of the high-frequency OH and NH modes will be important for understanding proton transfer across such molecular interfaces in future experiments. This first experiment was later expanded into a comprehensive study of the asymmetric 7AI—Ac heterodimer, in which the three major hydrogen-bonded modes are excited and the vibrational dynamics and couplings of the system are probed with pump-probe (Chapter 5) and 2D IR (Chapter 6) experiments.

4.2 Experimental Considerations

In this work, we applied ultrafast continuum mid-IR spectroscopy to probe the intermolecular coupling between the OH and NH stretching vibrations within the 7AI—Ac heterodimer. The heterodimer spectrum, which is discussed in detail in Chapter 1, is shown in Figure 4.1. The high-frequency portion of the spectrum consists of four main regions. The NH stretch is centered around 3250 cm^{-1} , while a double-peaked feature due to the acid OH is peaked around 2500 cm^{-1} and 1950 cm^{-1} . Following this initial study, theoretical work in our group has shown this structure is due to a Fermi resonance between the OH stretch and the overtone of the OH bend.⁶⁹ The complex substructure from 2600 to 3100 cm^{-1} is due to Fermi resonances between the high frequency modes and overtones of various fingerprint modes.^{59,61} The OH stretch is excited with a pump pulse centered at 2500 cm^{-1} . The CIR pulse was used to probe the vibrational dynamics across the high-frequency portion of the spectrum (1650 - 3400 cm^{-1}) following that excitation. The pump pulse, the CIR probe pulse, and the probed region of the 7AI—Ac spectrum are plotted in Figure 4.1.

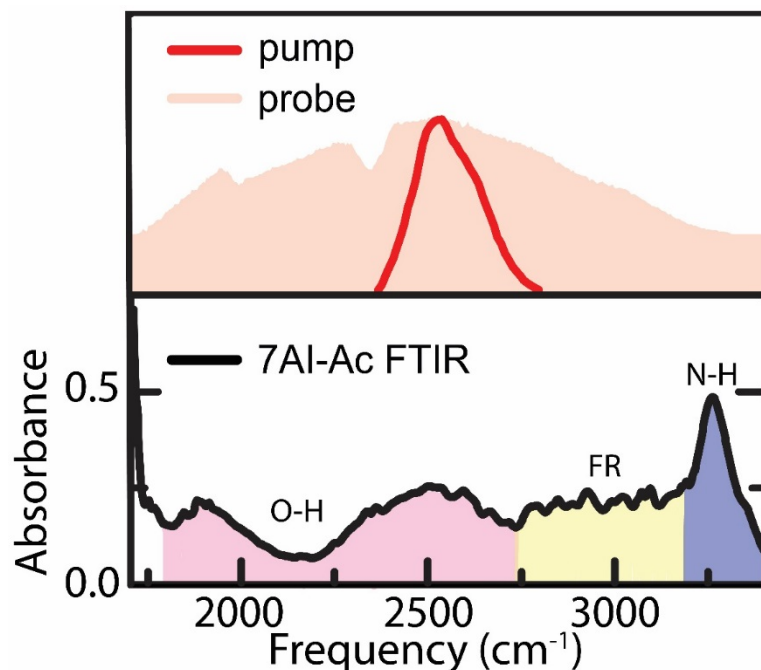


Figure 4.1: Spectrum of the pump and probe pulses (top) and FTIR of the 7AI—Ac dimer (bottom) over the studied region.

This experiment was carried out using our initial pump-CIR probe set-up using a single element MCT detector, making it necessary to scan the monochromator for each wavelength. As discussed in Chapter 3, this detection method limits the signal-to-noise and spectral and temporal resolution of the experiment. Consequently, the data presented here has a temporal resolution of 50 fs and spectral resolution of 25 cm^{-1} .

All reagents were obtained from Sigma-Aldrich and used without further purification. The 0.25 M 7AI—Ac heterodimer sample was prepared in carbon tetrachloride with an acetic acid/7AI molar ratio of approximately 0.95:1 and contained in a 100 μm thick Teflon sandwich cell between two 1 mm thick calcium fluoride windows.

4.3 Results

In this initial experiment, the OH stretch is excited with a 300 cm^{-1} full width half maximum (fwhm) bandwidth, 50 fs pump pulse centered at 2500 cm^{-1} , and the resulting transient response is measured from 1650 to 3400 cm^{-1} with the CIR probe pulse as a function of time delay between the pump and probe pulse. Transient spectra show the difference between a pumped and unpumped sample at a fixed time delay. The transient spectra of 7AI—Ac at 0.35, 1.0, and 2.5 ps are shown in Figure 4.2

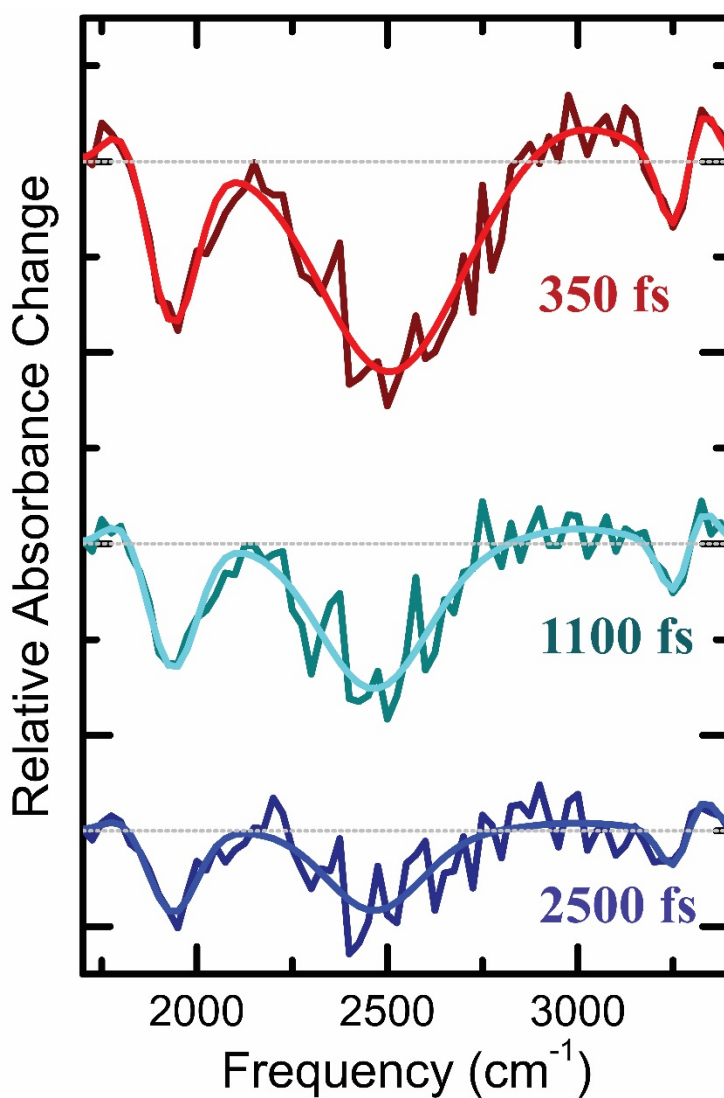


Figure 4.2: Transient spectra and fits of 7AI—Ac at time delays of 0.35, 1.0, and 2.5 ps.

The transient spectrum is composed of six main features. There are three reduced absorbances at 1938, 2500, and 3254 cm^{-1} . These correspond to the $0 \rightarrow 1$ transitions of the two OH bands and the NH stretch seen in the FTIR spectrum. Three weaker induced absorbances at 1803, 2999, and 3320 cm^{-1} are also observed. The induced features are more difficult to definitively assign, as will be discussed below.

Third-order transient, or “pump-probe”, vibrational spectroscopy is described in Chapter 2. Generally, reduced absorbances, or “bleaches”, occur at the excited $0 \rightarrow 1$ vibrational frequencies, and induced absorbances corresponding to the associated $1 \rightarrow 2$ vibrational transitions may be observed.^{94,118,119} The induced absorbances are generally at lower frequencies than the $0 \rightarrow 1$ transition because of the anharmonicity of the potential. However, the vibrational spectrum of the strongly hydrogen-bonded OH and NH modes of the 7AI—Ac dimer is complicated by very anharmonic potentials, strong coupling to low-frequency modes, and Fermi resonances.^{61,69} Additional spectral changes can be due anharmonic coupling between the modes. When the pump pulse is narrower than the probe, as is case with the CIR probe, vibrational coupling can be observed as reduced absorptions at frequencies that are not directly excited. This is observed in the transient spectra in Figure 4.2, which show strong reduced absorbances for both the 1940 cm^{-1} OH mode and the 3250 cm^{-1} NH stretch.

The anharmonicity of the 7AI—Ac vibrational spectrum makes it difficult to predict the frequencies of the $1 \rightarrow 2$ transitions that may contribute to the observed induced absorbances. These transitions sample a higher part of the anharmonic potential and can vary greatly from the fundamental transition in energy. While usually rare, additional transitions, such as the $1 \rightarrow 3$ or $0 \rightarrow 2$ transitions, may also be observed in hydrogen-bonded systems. For example, the $0 \rightarrow 2$ overtone of the shared proton ($\text{O} \cdots \text{H} \cdots \text{O}$) in hydroxide solutions was observed by 2D IR.¹²⁰

As seen in Figure 4.1, the two OH modes, the Fermi resonances, and the NH stretch result in a very congested high frequency spectrum. This continuous absorption of the strongly coupled modes further complicates the transient spectrum, which results from broad, negative reduced absorbances for the fundamental transitions and even broader, positive induced absorbances due to the $1 \rightarrow 2$ and potentially $1 \rightarrow 3$ transitions.

When this initial study was completed, the two OH modes had not yet been independently identified. As such, the pair of reduced absorbances at 1940 and 2500 cm^{-1} were assigned to the $0 \rightarrow 1$ transition of the two parts of the OH mode, and the induced absorbances at 1803 and 2999 cm^{-1} were assigned to a very broad and very anharmonic $1 \rightarrow 2$ transition. The $1 \rightarrow 3$ transition of the OH stretch was also proposed as a potential origin of the 2999 cm^{-1} feature.

The high frequency reduced absorbance (3254 cm^{-1}) and induced absorbance (3320 cm^{-1}) were originally attributed to a frequency shift in the NH vibration upon excitation of the OH stretch. This coupling could result from the weakening of the bridging hydrogen bond between the 7AI NH and the acid carbonyl, caused by the perturbation of the OH bond (and therefore the other bridging hydrogen bond and intermolecular distance). As a result, the NH bond would become stronger and the mode would increase in frequency. The extreme case would be completely breaking that intermolecular bond, which would show up an induced absorbance of the monomer free NH at 3450 cm^{-1} . The induced absorbance at an intermediate frequency instead suggests that this bond is weakened but not broken. However, the frequency range probed in this initial study did not include the free NH stretch of the monomer, which could confirm that the dimer is not breaking.

Alternatively, the reduced absorbance at the NH frequency could be due to energy transfer from the OH mode to the NH mode resulting from the strong coupling. However, such a 750 cm^{-1} uphill energy transfer would have to be accompanied by the

loss of several quanta of low-frequency vibrations, which is unlikely. Also, in this picture the induced absorbance at 3254 cm^{-1} is difficult to assign and could be due to either a blue-shifted $1\rightarrow 2$ transition or a $1\rightarrow 3$ transition of the NH stretching mode. Independent of the spectral assignment, the main conclusions remain clear: the NH and OH vibrational modes are very strongly intermolecularly coupled, and this strong coupling is due to the cyclic structure of the hydrogen-bonded interface.

While Figure 4.2 shows three representative time delays, the full data set is shown in Figure 4.3. This contour plot is composed of a transient spectrum measured at each time delay from -1000 to 2750 fs, in steps of 50 fs. Before time zero, the probe pulse reaches the sample before the pump, and no transient response is observed. At time zero, the six transient features appear within the time resolution of the experiment, and then decay back toward zero as the time delay is increased. The continuum probe allows us to observe a large portion of the spectrum change as a function of time delay with a single experiment. A global fit of this full dataset was carried out to model the dynamics of the transient vibrational spectrum, and is described in the next section.

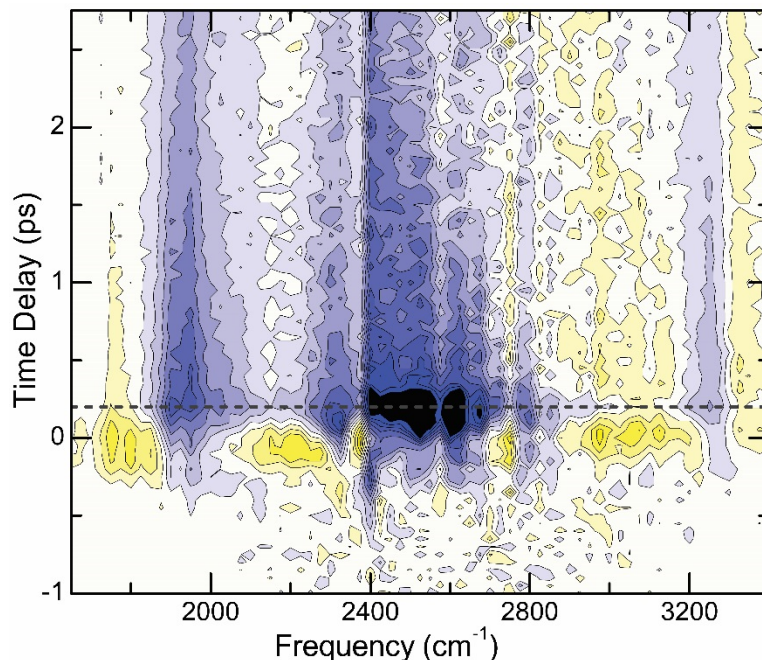


Figure 4.3: Full IR pump–CIR probe data set (absorbance change) spanning a frequency range of 1750 cm^{-1} in 25 cm^{-1} steps and a time delay of -1.0 to 2.75 ps in 50 fs steps. The plot contains 17 evenly spaced contours from -1.35 (darkest blue) to 1.35 (darkest yellow) mOD.

4.4 Fitting

At each time delay, the transient spectrum was modeled as sum of six Gaussian peaks corresponding to the six major features observed. The fits of the transient spectra at 0.35 , 1.0 , and 2.5 ps are overlaid on the actual data in Figure 4.2. While the spectra are more complex than this simplified model, Gaussian peaks are sufficient to reproduce the observed transient response within the current level of analysis and the data quality of this initial study. The 350 fs transient spectrum, the six component peaks, and the overall sum are shown in Figure 4.4.

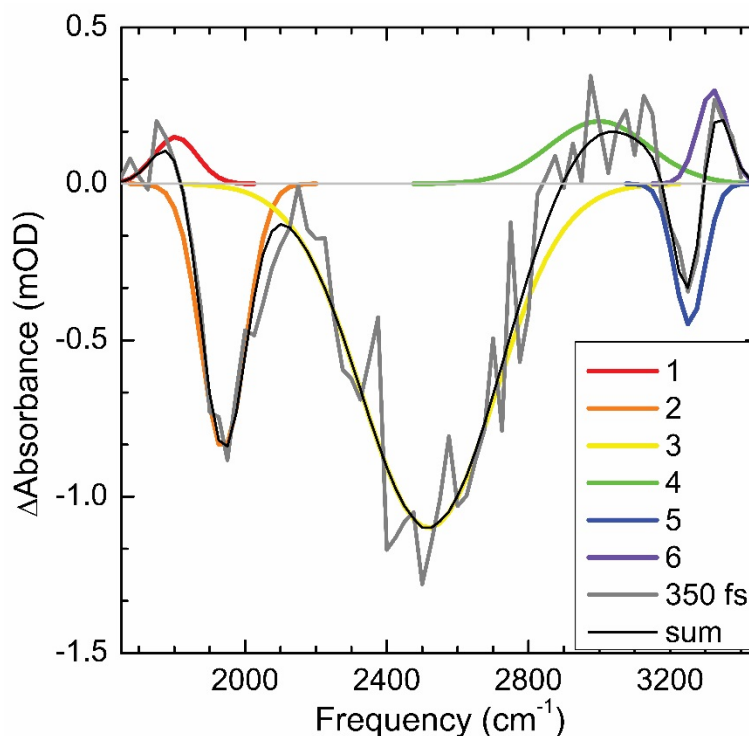


Figure 4.4: Fitting of the transient spectrum at 350 fs with the sum of six Gaussians, each corresponding to one of the observed features.

The $0 \rightarrow 1$ transition of the OH stretch at 2500 cm^{-1} was directly excited in this experiment, while all of the other features are due to energy transfer, vibrational coupling, or excited state absorption. Spectral diffusion following excitation leads to a frequency shift and narrowing of the 2500 cm^{-1} reduced absorbance. The remaining five peaks change only in amplitude, not frequency or width, as a function of delay time. A global fit of the full data set from 200 to 2500 fs was performed. The center frequency, peak width, and amplitude of the OH stretch mode were all allowed to vary. However, the center frequencies and peak widths of the other five Gaussians were fixed at the average values determined by independently fitting each time point from 200 to 2500 fs with floating parameters. These fixed parameters are given in Table 4.1. The fit of the full dataset is shown in Figure 4.5, along with the residuals.

Table 4.1: Fixed parameters for fitting 7AI—Ac transient response

	1	2	4	5	6
Center Frequency (cm^{-1})	1795	1939	3000	3260	3333
Peak width (cm^{-1})	61	63	140	43	42

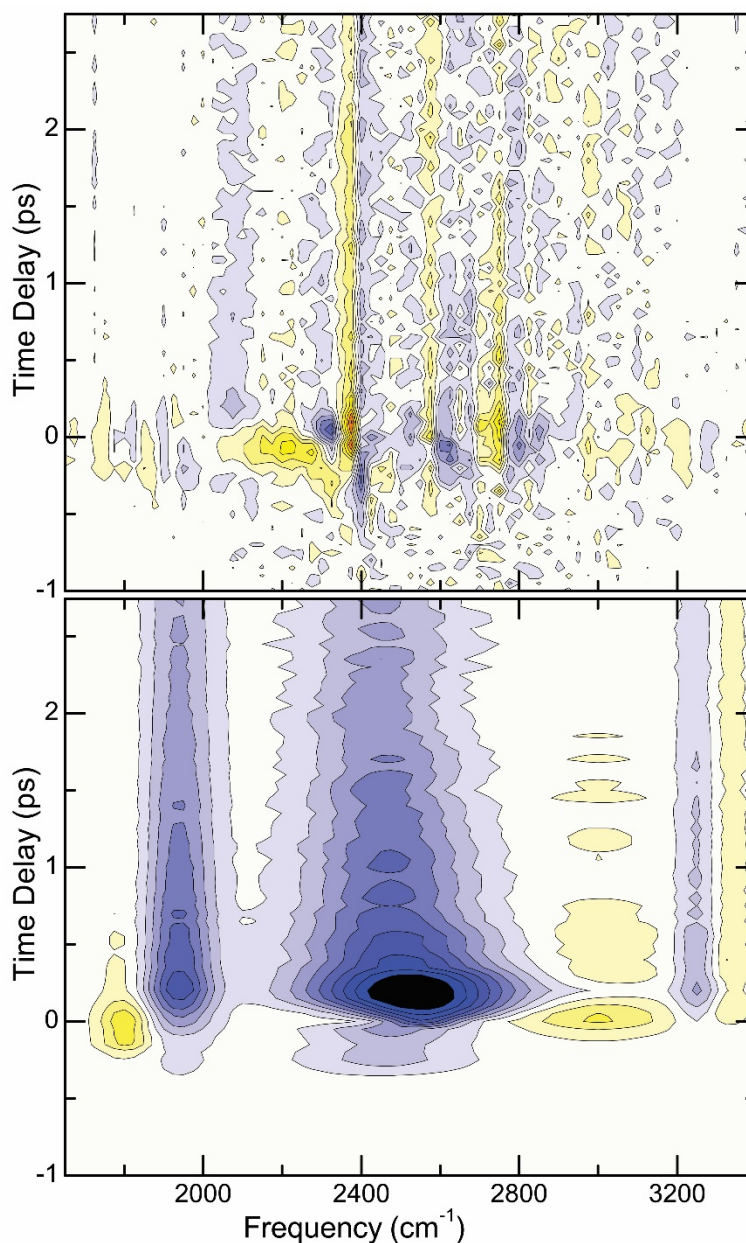


Figure 4.5: The spectral fit (bottom) and residual (top) are shown from -1.00 to 2.75 ps. The plot contains 17 evenly spaced contours from -1.35 (darkest blue) to 1.35 (darkest yellow) mOD.

The fitted amplitudes of each peak is plotted as a function of time delay in Figure 4.5. At short time delays, a coherent artifact due to nonresonant signal is generated by the pump and probe pulses overlapping in the sample windows. Since the fwhm of the pulse overlap is less than 160 fs, the data is fit from 300 fs, well after the coherent artifact. The amplitudes of all five fixed Gaussians can be fitted with single-exponential decays with a common time constant of approximately 2.5 ps. The directly excited 2500 cm^{-1} peak is fit with a double-exponential decay and exhibits both the same 2.5 ps time constant and a second ultrafast time component that is faster than our temporal resolution of 150 fs. The common time scale supports the assignment of the NH vibrational dynamics to a frequency shift upon excitation of the OH vibration.

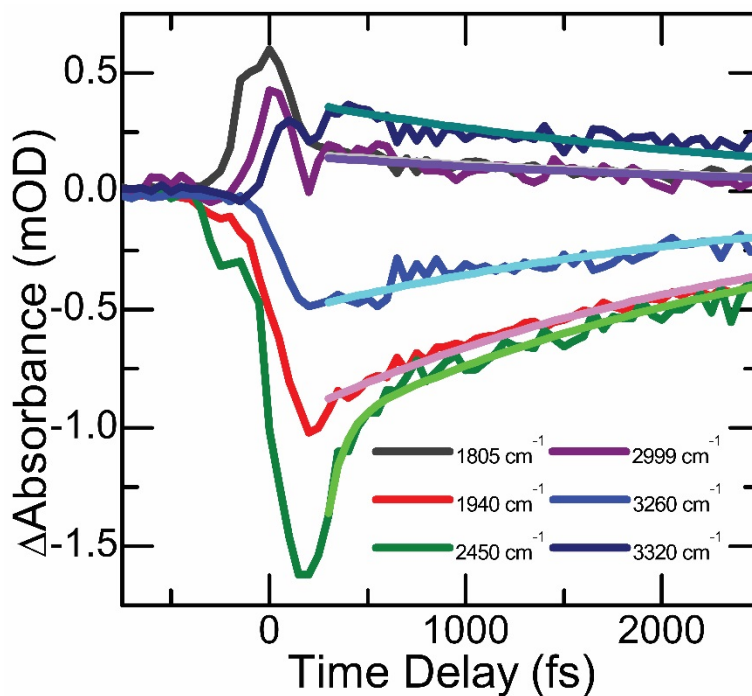


Figure 4.6: Fitted amplitudes of the six Gaussian peaks. The legend gives the five fixed center frequencies (1795, 1939, 3000, 3260, and 3320 cm^{-1}) and the average center frequency value of the floating peak (2450 cm^{-1}).

Previously, shorter decay times of less than a ps have been observed in homodimers of 7AI and acetic acid,^{54–60} as well as in DNA base pairs.^{43,66,121,122} In those systems, the OH or NH bands are on top of the Fermi resonances, which results in very strong coupling to the bend overtones. In this study, a faster time component may be obscured due to the data quality. Alternatively, the NH and OH bands of the heterodimer may be less strongly coupled since they are shifted to either side of the Fermi resonances. This would result slower energy transfer into the low frequency modes and a correspondingly longer decay time.

While the amplitude of the directly excited 2500 cm^{-1} peak has similar vibrational relaxation dynamics to the other five modes, the OH stretch also exhibits spectral diffusion dynamics that were reproduced by allowing the center frequency and bandwidth of this peak to vary with the time delay. The floating center parameters for this peak are shown in Figure 4.6.

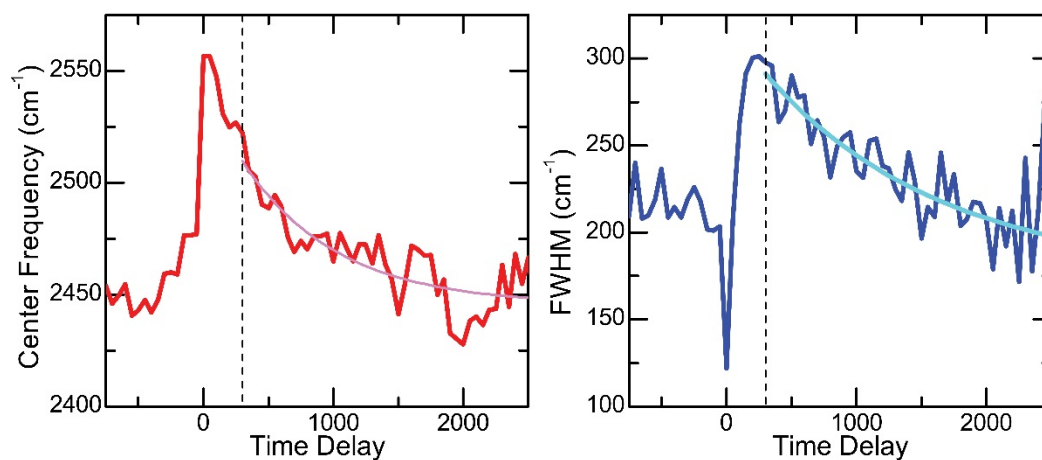


Figure 4.7: Center frequency and peak width (fwhm) of the sixth Gaussian peak, which were allowed to vary as a function of the pump–probe time delay. The dashed vertical line at 0.3 ps indicates the start of the single-exponential fits with time constants of 0.6 and 1.3 ps, respectively, as described in the text.

These spectral diffusion dynamics are observed because the pump intensity is not constant across the very broad OH spectrum. Additionally, the transition dipole moment may vary across the bandwidth of broad features. Both of these can contribute to the nonequilibrium excitation observed here, which relaxes to the equilibrium center frequency and peak width in 0.6 and 1.3 ps, respectively. No noticeable spectral diffusion dynamics were observed in the low-frequency part of the OH mode or the NH mode, which were fit with fixed center frequencies and widths, as discussed above.

4.5 Conclusions

This chapter summarizes the first ultrafast continuum mid-IR spectroscopy measurements of the 7AI—Ac heterodimer vibrational dynamics. Excitation of the OH stretching band leads to spectral changes across 1750 cm^{-1} . The broad transient spectrum is attributed to excitation of both OH bands within the time resolution of the experiment and an induced frequency shift of the NH stretch. This indicates very strong intermolecular coupling between the OH vibration of the acetic acid and the NH vibration of the 7AI mediated through the cyclic hydrogen-bonded structure. The strong coupling is further supported by the common lifetime of the OH and NH vibrations of about 2.5 ps, which is significantly longer than those previously observed for the corresponding homodimers. The complex transient spectrum is not fully understood and will benefit from further experimental and theoretical work.

Since the strong coupling is caused by the cyclic hydrogen-bonded structure, it is likely a general property of such systems. Given the abundance of similar structures in biological systems, we believe that the strong coupling observed here could be important for understanding the mechanism of biochemical energy dissipation and transfer as well as proton transfer reactions. The insight gained in this initial study and the implementation of an infrared array detector provided the motivation and technical

ability to expand these preliminary results into a comprehensive study of the vibrational dynamics of the 7AI—Ac heterodimer following the excitation of not only the OH stretch, but also the lower frequency OH band and the higher frequency NH stretch. The results of that study are presented in the following chapter.

CHAPTER 5

A COMPREHENSIVE STUDY OF THE VIBRATIONAL DYNAMICS OF THE 7-AZAINDOLE—ACETIC ACID HETERODIMER

5.1 Overview

A comprehensive pump-probe and 2D IR study of the 7AI—Ac heterodimer was performed by probing the vibrational spectrum from 1000 to 3500 cm^{-1} following three different excitations. In the previous chapter, the results of our initial transient mid-IR spectroscopic study of this dimer were presented. In that work, the OH stretch at 2500 cm^{-1} was excited and the high frequency portion (1650 to 3400 cm^{-1}) of the vibrational spectrum was probed with the CIR pulse. That study revealed an instantaneous response of the entire high frequency end of the spectrum, including the NH stretch 750 cm^{-1} higher in energy, indicating that the hydrogen-bonded interface plays a pivotal role in the dissipation of vibration energy across asymmetric hydrogen bonded interfaces.⁶⁷ Since that work, the incorporation of an array detector as described in Chapter 3 has greatly improved the data acquisition time and obtainable data quality. In this chapter, the pump-probe results at three excitation frequencies are presented. This expanded study includes time resolved pump-probe measurements mapping out the energy transfer throughout the dimer following three different excitations. The three pump frequencies were selected to correspond to the broad hydrogen-bonded NH and the two features of the OH vibration of the heterodimer, which have been assigned previously.^{61,69} The NH stretch of the 7AI is centered at approximately 3250 cm^{-1} , while

the acid OH stretch is centered at 2500 cm^{-1} . The third pump frequency of 1900 cm^{-1} corresponds to a Fermi resonance between the OH stretch and the overtone of the COH bend, which is centered at 1950 cm^{-1} .⁶⁹ The CIR probe pulse spans from less than 1000 to more than 3500 cm^{-1} , revealing the dynamics of nearly the entire vibrational spectrum following each excitation. The incorporation of an MCT array detector also enabled measuring 2D IR spectra, which are presented in Chapter 6 and reveal the strong couplings across the vibrational spectrum caused by the bridging hydrogen bonds.

5.2 Experimental Design and Considerations

Pump-probe and 2D IR experiments were measured in the updated experimental design described in Chapter 2 and shown in Figure 2.12. The generation of mid-infrared continuum (CIR) probe pulses is described in detail in Chapter 3.^{79,109} Pump pulses centered at 2500 , 3250 , or 1900 cm^{-1} with a bandwidth of about 250 cm^{-1} (fwhm) and total pulse energies of 31 , 30 , and $15\text{ }\mu\text{J}$, respectively, were generated as described in Chapter 2 by non-collinear difference frequency mixing of the signal and idler outputs of a commercial OPA (Coherent OPerA Solo). Individual pump pulse energies at the sample ranged from 1.6 to $5.5\text{ }\mu\text{J}$. The probe pulse was detected with the MCT array detector described in section 3.4.2, resulting in a frequency resolution ranging from 2 to 16 cm^{-1} . The 0.25 M 7AI—Ac sample was prepared in the same manner as that used in the initial study described in Chapter 4.

5.3 Mid-IR Pump—CIR Probe Results and Discussion

5.3.1 High Frequency Transient Response of the 7AI—Ac Heterodimer

In Chapter 2, transient IR spectroscopy was described and demonstrated in the relatively straightforward example of RDC. Generally, a transient signal is observed as a reduced absorbance, or bleach, of the $0 \rightarrow 1$ transition accompanied by an induced absorbance of the $1 \rightarrow 2$, which typically occurs at a slightly lower frequency than the fundamental mode due to anharmonicity of the potential. While this transient behavior was clear in RDC, the transient spectrum of the 7AI—Ac dimer is complicated by the large anharmonicity of the system, the congestion of the vibrational spectrum, and the number and strength of couplings across the entire spectrum. The earlier work presented in Chapter 4 studied the dynamics of the 7AI—Ac heterodimer following excitation of the OH stretch at 2500 cm^{-1} . In that study, an instantaneous response was observed across the high-frequency region (1650 to 3400 cm^{-1}) with limited spectral resolution. In addition to the bleach of the two main OH features, the NH stretch, which occurs 750 cm^{-1} higher in energy than the excitation pulse, is also bleached and surrounded by two induced absorbance features. While the assignment of the bleach features was clear, the assignment of the induced features was not definitive due to the limited spectral coverage and absence of a 2D IR spectrum.⁶⁷ In the present study, the probed region is expanded to include fingerprint modes down to 1000 cm^{-1} and the high frequency side is extended to 3500 cm^{-1} with greater spectral resolution and improved data quality.

The transient spectrum at 200 fs following each of the three excitations is seen in Figure 5.1, along with the FTIR of the heterodimer and the three pump pulses. The high frequency region of the transient response following excitation of the hydroxyl stretch at 2500 cm^{-1} is in agreement with the results presented in the previous chapter. The transient spectrum contains three bleaches at 1940, 2500, and 3250 cm^{-1} , corresponding to the $0 \rightarrow 1$ transitions of the three hydrogen-bonded modes, and three induced absorbances at approximately 1800, 3000, and 3320 cm^{-1} . In the previous study, the induced absorbances at 1800 and 3000 cm^{-1} were tentatively assigned to the $1 \rightarrow 2$ transition of the OH modes, while the 3320 cm^{-1} induced absorbance was assigned to a frequency shift of the NH stretch caused by the intermolecular coupling of the OH and NH across the hydrogen bonded interface.⁶⁷

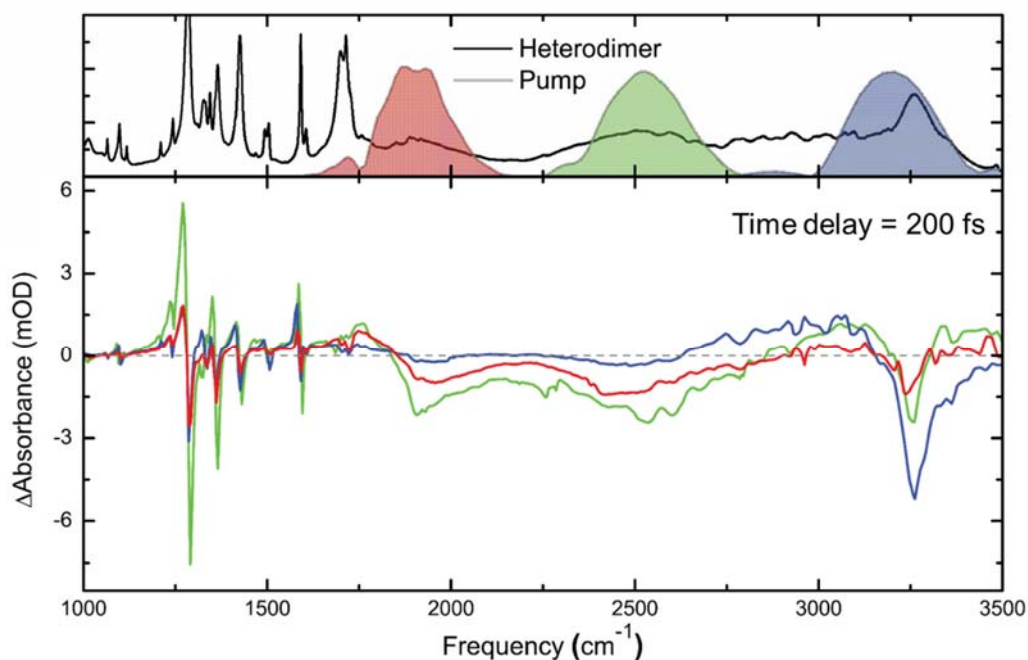


Figure 5.1: Transient spectra of the 7AI—Ac heterodimer at 200 fs (bottom) after each of three excitation pulses shown with the FTIR at top

While the excitation of either OH mode couples strongly with the higher energy NH mode, direct excitation of the 3250 cm^{-1} mode results in only a weak response from the OH modes at the same 200 fs time delay. Following that excitation, a strong induced absorbance is also observed in the Fermi resonances from about 2600 to 3100 cm^{-1} , while the higher frequency induced absorbance (3320 cm^{-1}) is not observed.

Figure 5.2 shows the dynamics of the vibrational spectrum following excitation at 2500 cm^{-1} . As observed previously, all modes appear in the transient spectrum within the time resolution of the experiment. In addition to this instantaneous response across the probed region, the improved signal-to-noise of this experiment reveals an oscillatory modulation of the transient signal. This can be observed more clearly by taking cuts of the contour plot to observe the dynamics of specific peaks. Figure 5.3a shows the dynamics at the three high frequency regions of interest: 1900 , 2500 , and 3250 cm^{-1} . Each of these modes has an ultrafast decay and an oscillation with a period of about 200 fs, corresponding to the intermolecular hydrogen-bond mode at 140 cm^{-1} . This beating pattern was observed previously for the heterodimer following excitation of the NH stretch,⁶¹ and similar modulations caused by low frequency hydrogen bond modes have been observed in various symmetric and asymmetric hydrogen-bonded systems, including the 7AI homodimer, acetic acid dimer, and DNA base pairs.^{46,56,58,60,61,68}

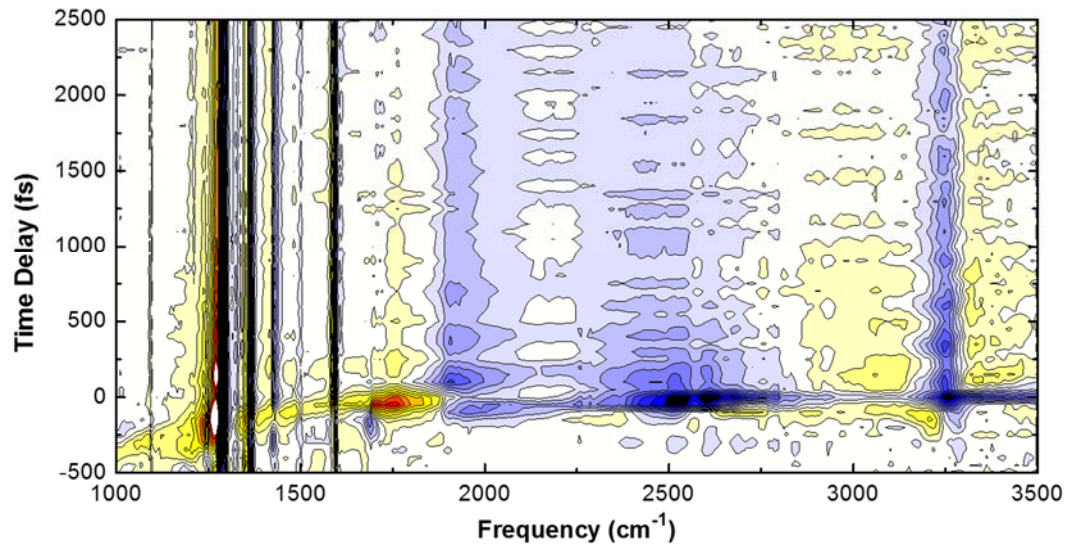


Figure 5.2: Transient response of the 7AI—Ac dimer following excitation of the OH stretch centered at 2500 cm^{-1}

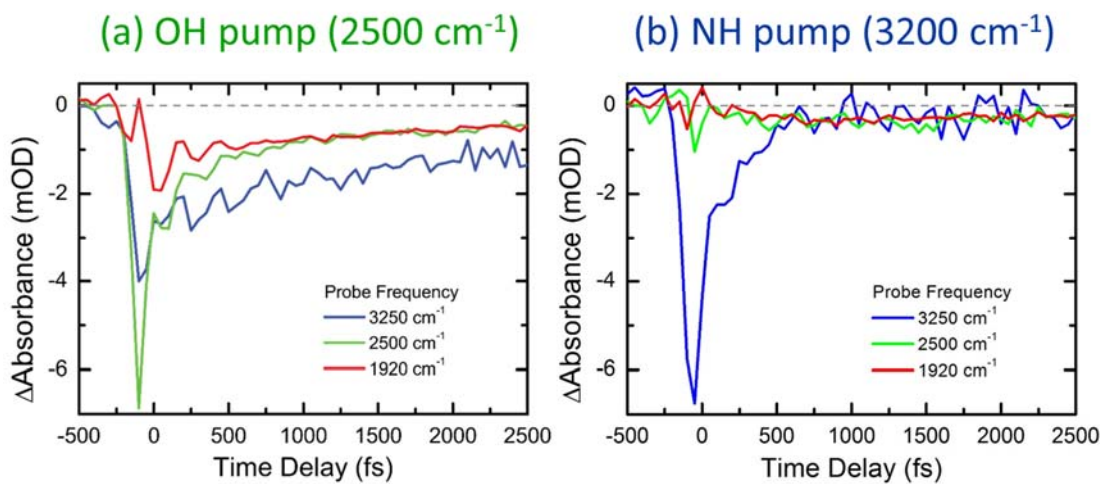


Figure 5.3: Dynamics of the three high frequency modes following excitation of the OH stretch (a) and NH stretch (b)

The full transient response following excitation at 1900 cm^{-1} , shown in Figure 5.4, is weaker but qualitatively similar to the excitation at 2500 cm^{-1} . An instantaneous response is observed at each of the three high frequency modes, along with the induced absorbances at 1800 , 3000 , and 3320 cm^{-1} . However, excitation of the amino NH at 3250 cm^{-1} , shown in Figure 5.3b and 5.5, results in markedly different vibrational dynamics.

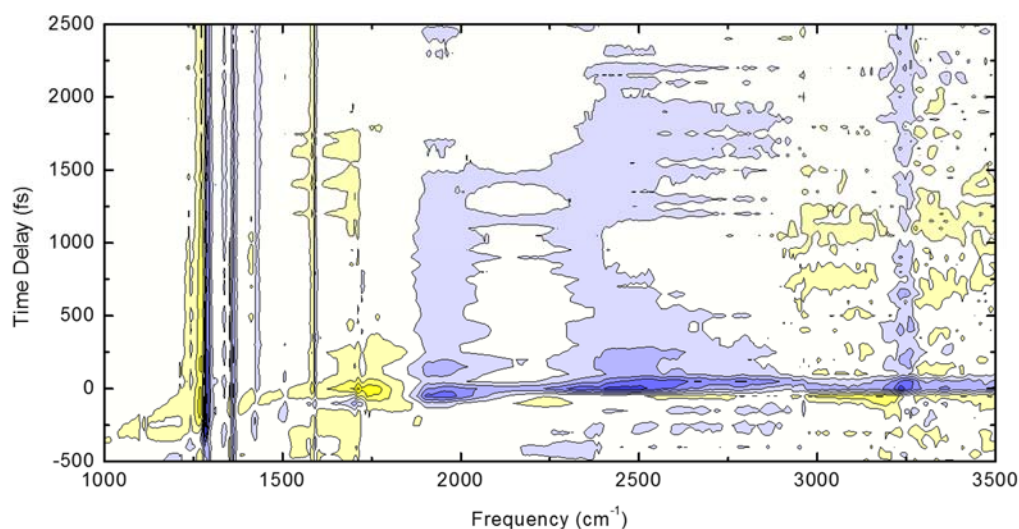


Figure 5.4: Transient response of the 7AI—Ac dimer following excitation of the coupled OH mode centered at 1940 cm^{-1}

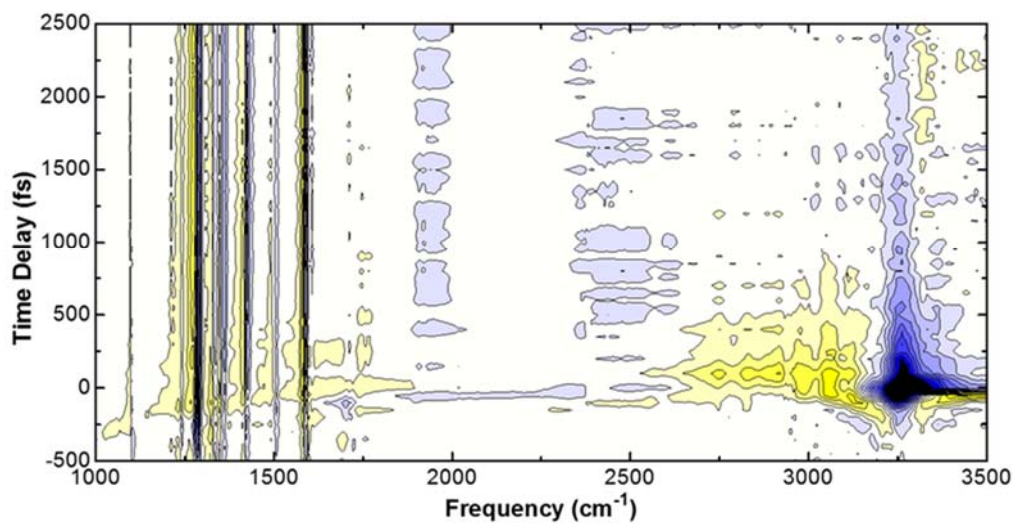


Figure 5.5: Transient response of the 7AI—Ac dimer following excitation of the NH stretch centered at 3250 cm^{-1}

Direct excitation of the NH stretch results in an instantaneous bleach and subsequent decay of that mode, but the OH modes at 1940 and 2500 cm^{-1} grow in with a rise time of about 300 fs. The broad induced absorbance at 3000 cm^{-1} , which clearly displays the same Fermi resonance substructure seen in the linear absorbance spectrum, decays at a similar rate. These induced absorbances are excited instantaneously, but decay rapidly on time scales similar to the rise of the OH signal. An induced absorbance at approximately 3000 cm^{-1} appears regardless of excitation frequency, but the feature observed following either OH excitation is narrower and weaker compared to that following the NH excitation, and also lacks the clear Fermi resonance substructure. This suggests that two different induced features may occur around 3000 cm^{-1} . The other two induced absorbances observed previously following the 2500 cm^{-1} excitation at 1800 and 3450 cm^{-1} appear only weakly following 3250 cm^{-1} excitation. This supports the possibility that these features are due to very anharmonic overtone or combination modes of the OH.

5.3.2 Fingerprint modes

In the full contour plots, it is clear that the fingerprint modes are much narrower than the broad hydrogen-bonded modes at high frequencies, making them difficult to interpret when displayed on the frequency axis. Figure 5.6 expands the transient spectrum from 1200 to 1650 cm^{-1} following the 2500 and 3250 cm^{-1} excitations. This spectral region is dominated by a series of ring-bending and deformation modes and was not included in our previous study.

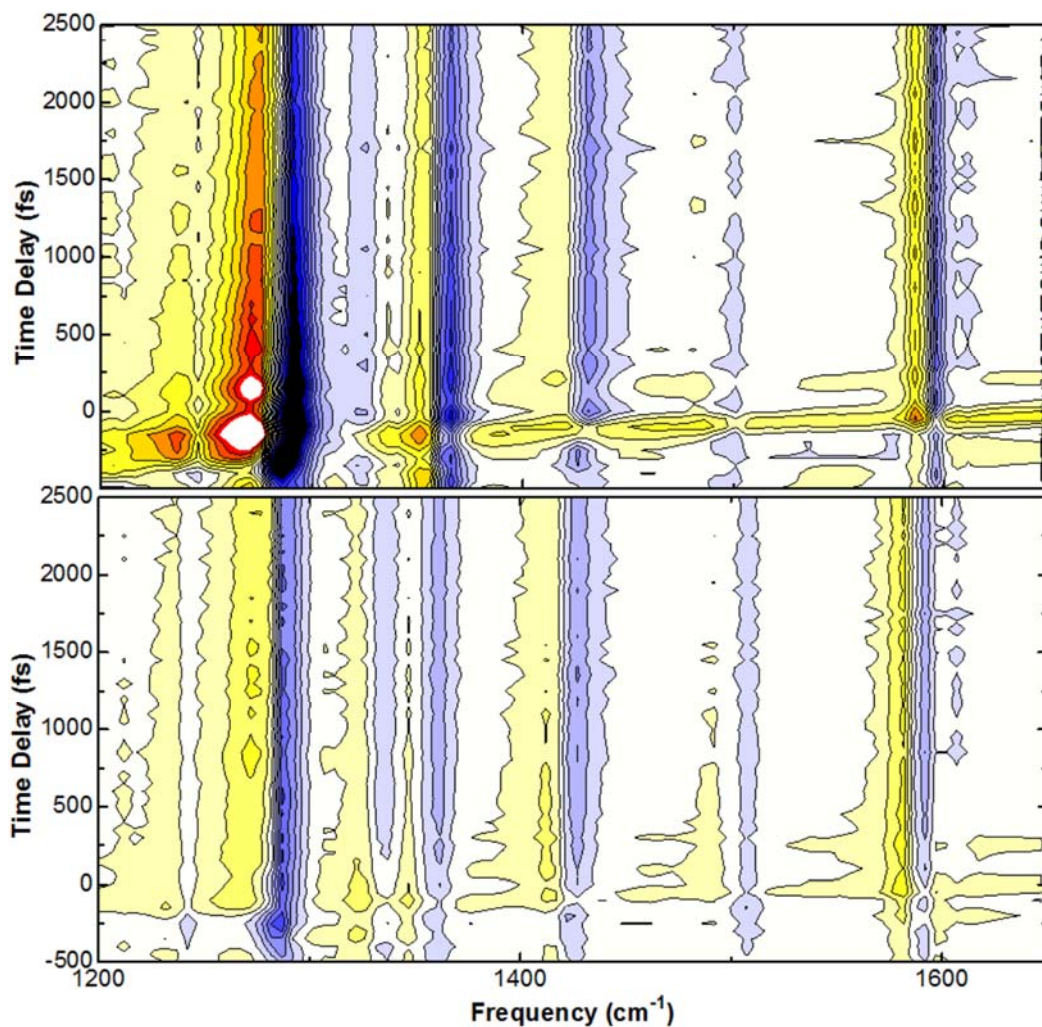


Figure 5.6: Transient response of the fingerprint modes following excitation at 2500 cm^{-1} (top) and 3250 cm^{-1} (bottom)

Generally, the fingerprint modes show up as the normally expected bleach and induced absorbance pair, indicating these modes are excited following both high frequency excitations. However, a pair of artifacts affects the transient response at low frequencies. The signal observed before zero time at the low frequencies is the perturbed free induction decay of the probe pulse. This is not directly frequency-dependent, but has a greater effect on narrower peaks and is seen in the fingerprint modes as a result.¹²³

A chirp of about 300 fs from 1500 to 1000 cm^{-1} is observed as a result of dispersion of the CIR probe pulse in the 0.5 mm Si filter and the 1 mm CaF_2 window in front of the sample, as discussed in Chapter 3.

Figure 5.7 shows the low frequency dynamics following excitation of both the OH and NH stretches. The short (2.5 ps) and long (13 ps) dynamics of each of three modes centered at approximately 1290, 1360, and 1430 cm^{-1} are shown. (These three modes will be discussed in more detail in Chapter 6.)

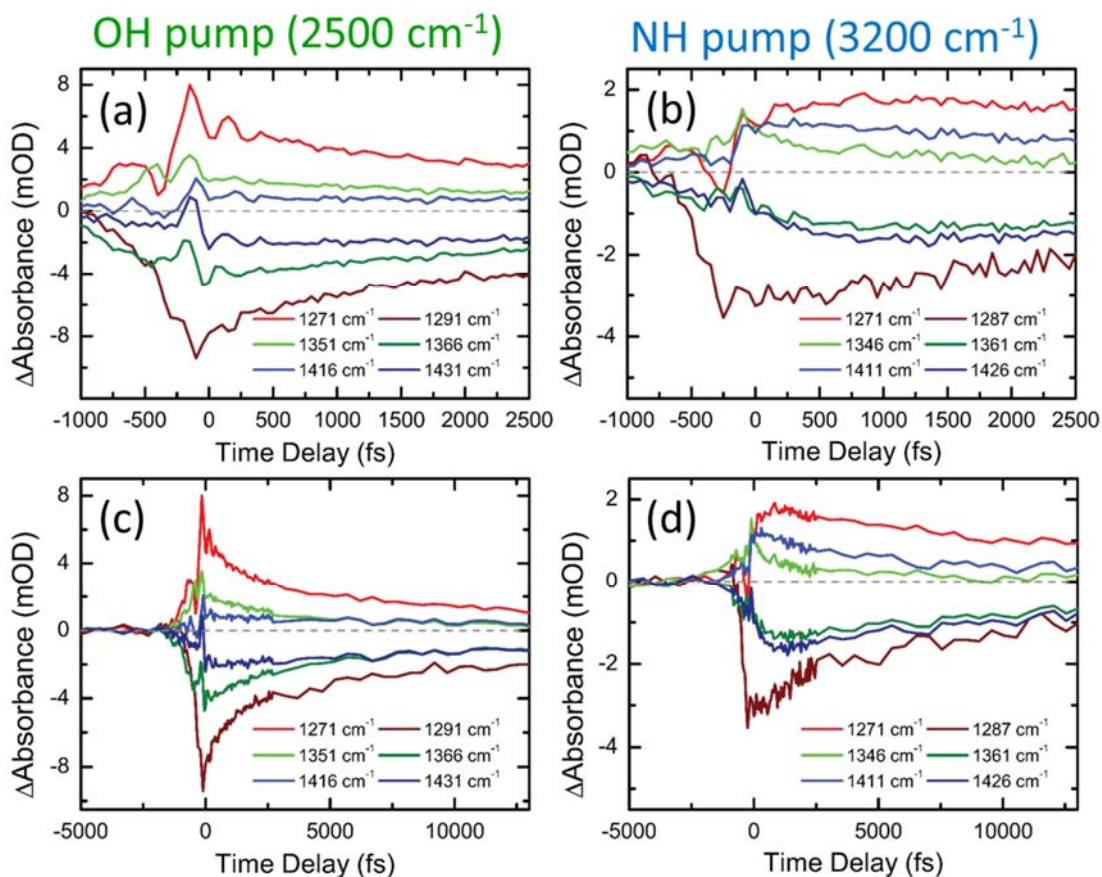


Figure 5.7: Dynamics of three fingerprint modes following excitation of the OH (a,c) and NH stretches (b,d) on short (a,b) and long (c,d) time scales.

The short time dynamics shown in Figures 5.7a and 5.7b allow us to resolve the time a mode takes to become excited, while the long time dynamics in Figures 5.7c and 5.7d reveal the lifetime of the excitations. In the short time dynamics following the 2500 cm^{-1} excitation in Figure 5.7a, the fingerprint modes, like the high frequency modes, are immediately excited and oscillate due to the modulation of the low frequency hydrogen-bond mode. The long time dynamics of these modes, shown in Figure 5.7c, exhibit differing dynamics at short times but eventually decay to the same slow (>5 ps) decay. This is clear in the decay of the peaks at 1360 and 1430 cm^{-1} and the corresponding induced absorbances.

However, the same modes show differing kinetic behaviors following the 3250 cm^{-1} excitation. While some vibrations, including the very strong 1290 cm^{-1} mode, are excited immediately, others, such as those at 1360 and 1430 cm^{-1} , show the same rise time of about 250-300 fs seen in the high frequency OH modes. The decays of both the high frequency NH stretch bleach and Fermi resonance induced absorbance also share this time scale. Understanding the structural differences in the fingerprint modes with different kinetic behaviors is vital to understanding how vibrational energy is dissipated throughout the hydrogen-bonded system.

5.3.3 Energy Transfer and Vibrational Coupling

The 7AI and acetic acid homodimers were previously studied with transient IR absorption spectroscopy by Nibbering and coworkers.^{56,58,60} Those studies focused on the high-frequency NH and OH stretch spectral regions and attributed the rapid spectral changes to an ultrafast decay into what they referred to as the hot ground state. In this

state, the observed XH stretch has returned to the ground state, but other modes remain vibrationally excited. This energy transfer to other vibrational modes through the dimers is facilitated by the strong coupling and anharmonicity of the hydrogen-bonded structures. However, the bandwidth of the traditional OPA pulses used in those experiments prevented direct observation of the other modes. Using the broadband CIR probe, we directly observe that ultrafast energy transfer from the NH stretching mode into the OH modes and various fingerprint modes. The instantaneous response across the spectrum, combined with the modulation of the hydrogen bond, suggests that the vibrational energy deposited in the OH mode is quickly dissipated across the hydrogen-bonded interface, resulting in delocalized excitation of the entire dimer unit in less than 200 fs. Following the 2500 cm^{-1} excitation, all of the fingerprint modes and their corresponding induced absorbances were excited within the time resolution of the experiment, suggesting strong coupling. The 200-300 fs relaxation of the NH stretch and the corresponding rise times of various high-frequency and fingerprint modes suggest a slower transfer of vibrational energy from the 7AI to the acetic acid.

The instantaneously excited vibrations are located predominantly on the 7AI monomer, while the modes with a clear rise time involve more acetic acid motion. The energy absorbed by the 7AI amino group is delocalized throughout that monomer in less than 200 fs, but takes longer to spread across the hydrogen-bonded interface into modes with high acetic acid character. The conjugated heterocycle has many ring bending and deformation modes that likely provide more pathways for energy dissipation than the smaller acetic acid monomer.

5.4 Conclusions

This comprehensive pump-probe study revealed the dynamics of the vibrational spectrum of the 7AI—Ac heterodimer. The excitation frequency dependence can be observed in the dynamics across the entire vibrational spectrum. Regardless of excitation frequency, the directly excited mode is instantaneously excited and decays rapidly in 300 fs. Following excitation of the OH stretch, all three high frequency modes are bleached instantaneously and continue to decay with a slower time scale of several ps. When the NH is directly excited, bleaches of the two OH modes grow in with a rise time of 300 fs (roughly the same as the rapid decay of the directly excited mode) before decaying. Additionally, the modulation caused by the intermolecular hydrogen-bonded intradimer mode at 140 cm^{-1} is much stronger following excitation of the OH stretch, suggesting that the coupling across the hydrogen-bonded interface is more significant when the acetic acid modes are directly excited. In comparison, excitation of the amino group of the 7AI results in both strong coupling to some fingerprint modes and energy transfer across the interface. To further understand the structure, couplings, and dynamics of this system, 2D IR spectra were measured at each of the three excitation frequencies and probed with the CIR. Those results are discussed in the next chapter.

CHAPTER 6

TWO DIMENSIONAL INFRARED SPECTROSCOPY OF THE 7-AZAINDOLE— ACETIC ACID HETERODIMER

6.1 Overview

The IR pump—CIR probe experiments presented in the previous chapter revealed interesting dynamics across the vibrational spectrum of the 7AI—Ac heterodimer that are dependent on the excitation frequency. To gain further insight into the strong couplings of the dimer, 2D IR spectra were measured at each of the three pump frequencies, 1900, 2500, and 3250 cm^{-1} , and probed with the mid-IR continuum. Like the pump-probe experiments, the implementation of the CIR probe uncovers information across nearly the entire vibrational spectrum of 7AI—Ac. This reveals strong interactions between nearly all of the modes, with some fingerprint modes coupling to the OH and NH features differently. The coupled modes provide further evidence for the localization of energy on the 7AI monomer prior to delocalization across the dimer. In this chapter, the results of the 7AI—Ac 2D IR experiments are presented and discussed. The heterodimer acid carbonyl is also discussed briefly.

6.2 2D IR of the 7AI—Ac Heterodimer

6.2.1 Experimental

The vibrational spectrum was probed from 1000 to 3500 cm^{-1} with the CIR pulse following excitation by each of the three excitation frequencies previously discussed (1900, 2500, and 3250 cm^{-1}). These spectra were measured in the pump-probe geometry described in Chapter 3. The coherence time τ_1 was scanned from -200 to +1000 fs in 2 fs steps, and the sample was probed at a waiting time τ_2 of 200 fs. For the full spectra, the pump polarizations were parallel to the probe, and measured on the MCT array detector as described in Chapter 3. The 0.25 M heterodimer sample was prepared in the same manner as the pump-probe samples in Chapters 4 and 5.

6.2.2 Results

The 2D IR spectra measured at each of the three pump frequencies and probed with the mid-IR continuum are shown in Figure 6.1. Bleaching of the high frequency spectrum is observed along the diagonal of all three spectra, spanning from the carbonyl at 1700 cm^{-1} to above the NH stretch at 3250 cm^{-1} . Additionally, the three main hydrogen-bonded modes are bleached regardless of the excitation frequency. While the intensity of all three bleaches are similar following either OH excitation, the OH bleaches couple only weakly with the NH stretch excitation. This indicates that coupling, rather than energy transfer, causes the response of the higher energy NH stretch following the 2500 cm^{-1} excitation. While coupling can cause a response in higher energy modes following excitation, energy transfer is more favorable from high to low energy modes. These 2D IR results are in agreement with the pump-probe results presented in the previous chapter.

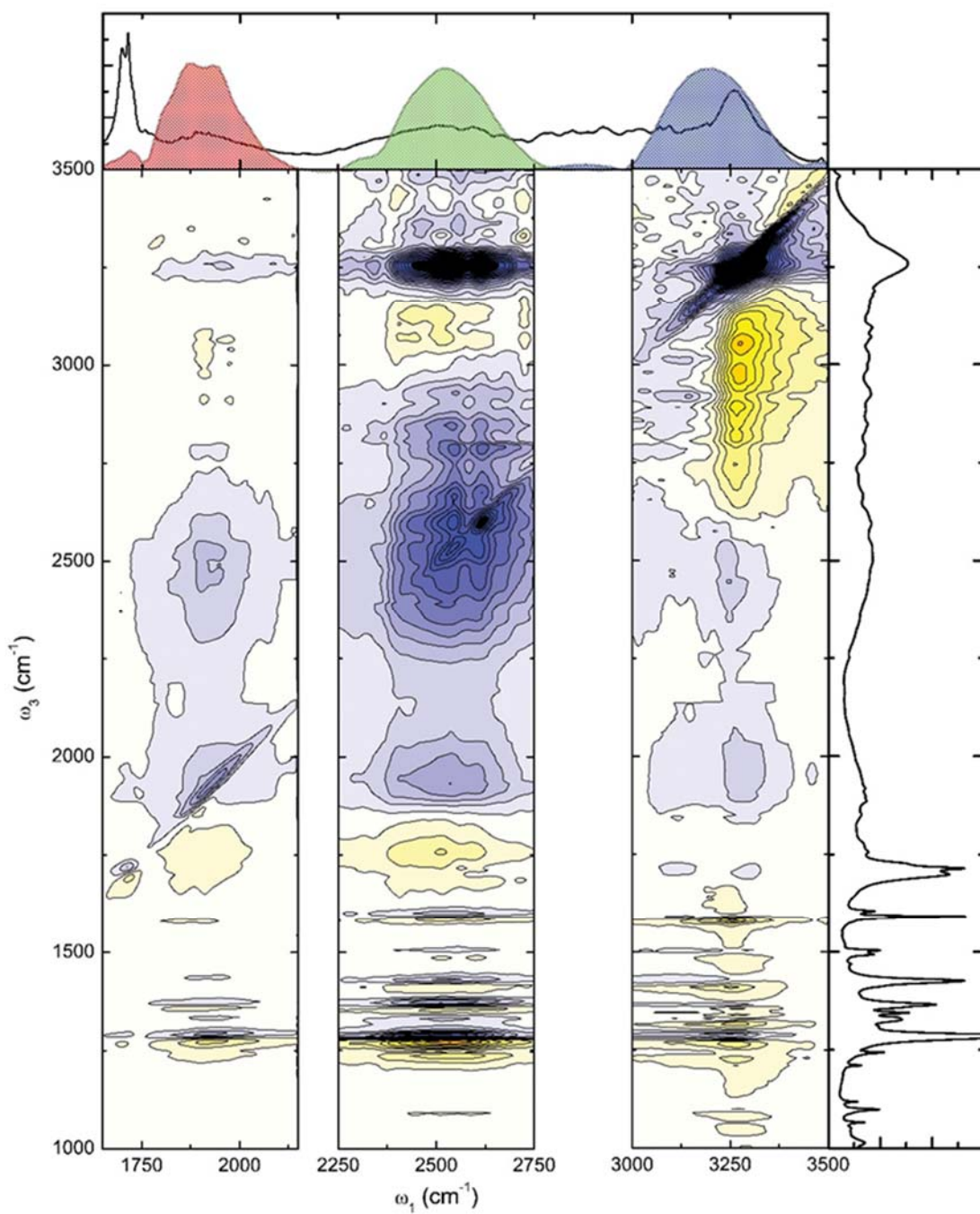


Figure 6.1: 2D IR spectrum of 7AI—Ac measured with three excitation pulses (shown on the FTIR at top) and probed with the CIR pulse.

The three high-frequency induced absorbances are less consistent across the pump axis. The highest frequency induced absorbance, observed at 3320 cm^{-1} in the pump-probes, is generally not present here. A bleach and induced absorbance pair occurs near the monomer peak around 3450 cm^{-1} . In the 7AI homodimer study by Nibbering et al⁵⁸, the monomer peak is shown to have a normal transient spectrum, with a bleach indicative of a $0\rightarrow 1$ and a lower frequency induced absorbance assigned to the $1\rightarrow 2$ transitions. In this 2D spectrum, however, the features observed here are broader and the induced absorbance occurs at higher energy than the bleach, suggesting these peaks come from a different source. The induced absorbance around 1800 cm^{-1} appears strongly coupled with both OH excitations, but this cross peak is completely absent with the high-frequency NH excitation. This is consistent with the previous assignment as the $1\rightarrow 2$ hot band of the OH stretch.

The final induced absorbance observed in the pump-probes occurs around 3000 cm^{-1} . In the pump-probes, the induced signal around 3000 cm^{-1} was observed regardless of the pump frequency, but the bandwidth and substructure of that feature varied. In the 2D spectra, this induced absorbance occurs across most, but not all, of the pump axis, and the cross peaks vary with excitation frequencies. A very strong induced absorbance cross peak occurs there between the NH stretch excitation and the Fermi resonances. While that cross peak clearly has the Fermi resonance substructure seen in the linear absorbance spectrum, a weaker induced absorbance at similar frequencies is coupled with both OH modes but is much narrower (in ω_3) and lacks that clear substructure. The different induced absorbances were clear in the pump-probe spectra, but there is an additional feature that is only clear from the 2D experiments: when the high frequency

Fermi resonances (3000 through 3200 cm^{-1}) are directly excited, they form a bleached cross peak through the lower frequency Fermi resonances and into the OH stretch, separating the induced features at (2500,3000) and (3250,3000). In the pump-probe, the induced feature dominates and the bleach is not observed. In contrast, when the low frequency edge of the Fermi resonances is pumped directly ($\sim 2700 \text{ cm}^{-1}$), the Fermi resonances are bleached through about 3000 cm^{-1} , and then an induced feature is observed between the Fermi resonances and the NH stretch bleach. The different substructure and coupling of these peaks suggests there may be multiple overlapping features in this range. In our earlier work, the $1 \rightarrow 2$ or very anharmonic $1 \rightarrow 3$ overtone of the OH stretch were suggested as a possible assignments for this feature. Assuming that the OH and NH cross peaks at 3000 cm^{-1} do in fact have different origins, as the 2D experiment suggests, both the 1800 and 3000 cm^{-1} induced absorbances couple with the OH bands but not the NH. This indicates they may have a common source, so one or both of the $1 \rightarrow 2$ or $1 \rightarrow 3$ transitions remain possible assignments.

As seen in the pump-probes, the much narrower fingerprint modes are difficult to see in the full 2D surfaces. The fingerprint region from 1200 to 1625 cm^{-1} is expanded in Figure 6.2. Many of the low frequency fingerprint modes, particularly those with energies in the range of 1250 to 1600 cm^{-1} , couple differently with the NH and Fermi resonances as compared to the OH modes. These are of particular interest, as the overtones and combination modes of these fingerprint vibrations correspond to energies that could feasibly form Fermi resonances with the OH and NH modes ($0 \rightarrow 2$ frequencies in the range of 2500-3200 cm^{-1}). These Fermi resonances provide a pathway

for rapid energy dissipation from the high-frequency modes into the fingerprint modes, which was observed in the pump-probe dynamics in the previous chapter.

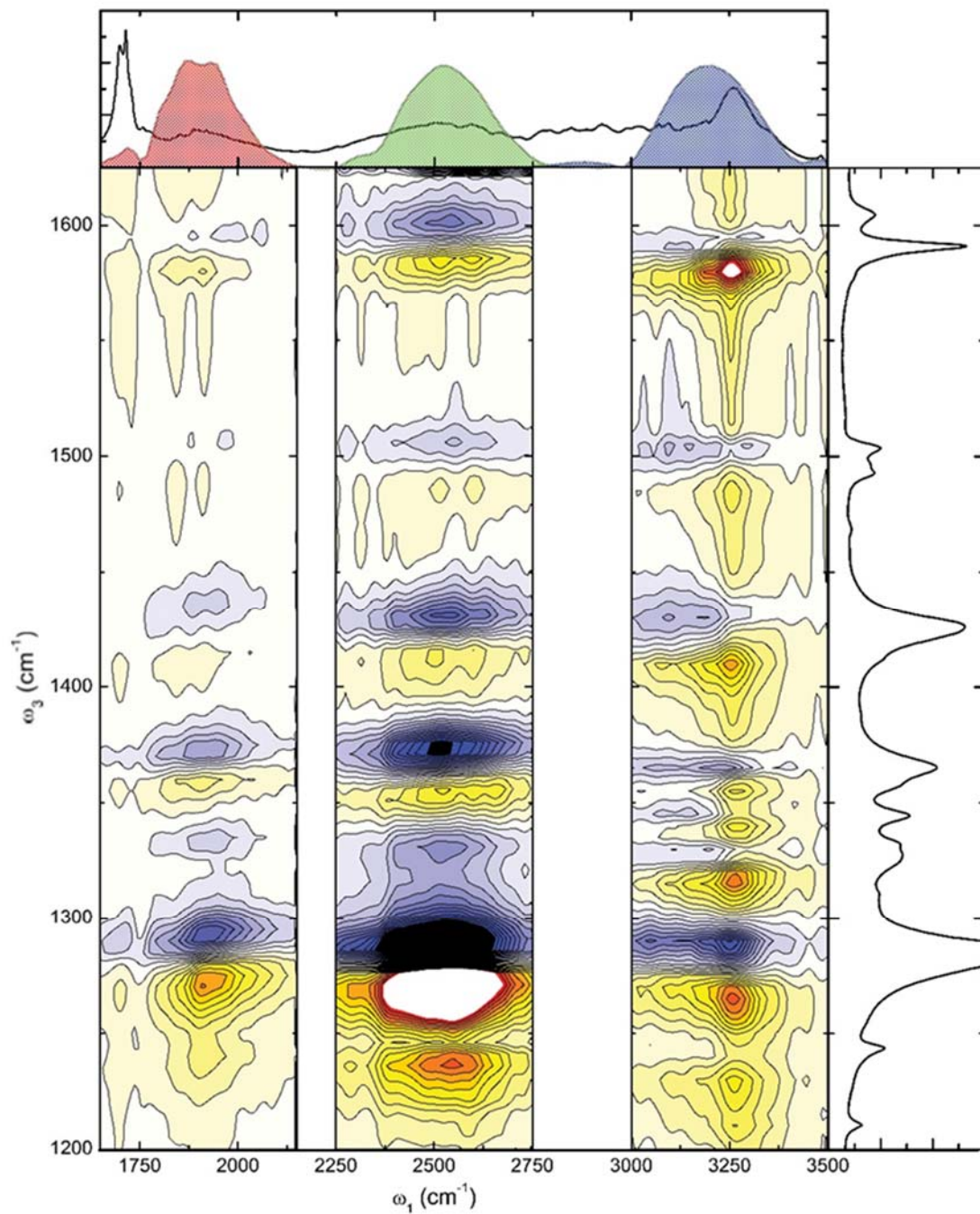


Figure 6.2: The fingerprint region of the 2D IR spectrum of 7AI—Ac measured with three excitation pulses (shown on the FTIR at top) and probed with the CIR pulse.

The vibration at about 1290 cm^{-1} , which has strong CN and CO (from COH and CNH) character, displays an immediate and very strong bleach regardless of excitation frequency in the pump-probes. The cross peak of this vibration is the only fingerprint bleach that couples strongly with the entire high frequency spectrum. Since this vibration greatly influences the intramolecular cyclic hydrogen-bonded structure and has strong COH and CNH bend character for each monomer, it follows that any perturbation of the hydrogen-bonded modes also induces a strong response from this mode. Additionally, the overtone ($0\rightarrow 2$) of this mode may be strongly coupled to both the OH stretch and the NH through the Fermi resonances. This mode is clearly important for the dissipation of vibrational energy, and will likely be important for proton transfer across this interface.

There are a series of fingerprint modes from about 1300 to 1450 cm^{-1} that couple differently to the different high-frequency modes. These modes include the 1360 and 1430 cm^{-1} modes that were looked at in the previous chapter. Both of these modes are predominately localized on the acetic acid monomer, with little contribution from 7AI vibrations. Each of these modes couples with both OH modes through the Fermi resonances, but neither couples with the NH stretch. The different coupling with the Fermi resonances and the NH stretch could also explain the different dynamics of these modes. Considering the pump-probe as the 2D spectrum integrated along the pump axis and collapsed onto the detection axis, these peaks in the transient response represent an average of the positive and negative features.

Nearly all of the fingerprint modes form induced absorbances with the NH excitation. This is clear in the shape of the cross peaks, many of which share the peak width of the NH stretch in the excitation axis, unlike many other modes that appear as continuous bands across much of the spectrum. In contrast, the cross peaks across the OH region consists of an induced absorbance at 1355 cm^{-1} with broad bleaches on either side from below 1300 to almost 1400 cm^{-1} .

Specifically, the modes from 1300 to 1400 cm^{-1} couple differently with the NH pump, where there are bleached cross peaks with the Fermi resonances excitation (3000 - 3200 cm^{-1}) at 1325 , 1350 , and 1375 cm^{-1} , but induced features with the NH stretch excitation (3250 cm^{-1}) at 1315 , 1340 and 1355 cm^{-1} . The positive peak at $(3250, 1315)$ does not appear at any other excitation frequencies. While broadband induced absorbances can be indicative of proton transfer (which will be discussed in Chapter 7), ground state proton transfer is unlikely.

The presence of the narrower (in ω_3) crosspeaks with the NH pump could be due to interferences between the Fermi resonance peaks and the NH. Adding a fourth 2D surface with an excitation pulse spanning the Fermi resonances from about 2700 to 3200 cm^{-1} could provide more information by revealing the frequencies at which the continuous bands split into multiple features. The interference of two modes with ultrafast decays and opposite signs could also result in pump-probe dynamics with a rise time followed by a slower decay, as is observed in these modes following the NH excitation. However, such overlapping features are not observed at the OH modes (1900 - 2500 cm^{-1}), where the same rise time is clearly observed.

6.3 The Elusive Carbonyl

In the pump-probes and 2D IR spectra, there is very little response from the acid carbonyl at 1700 cm^{-1} , which also falls within the bandwidth of the 1900 cm^{-1} pump pulse. Considering the strong linear absorbance of that peak and its involvement in the doubly hydrogen bonded intramolecular ring, this is surprising. In all of the transient spectra, the carbonyl peak at $\sim 1700\text{ cm}^{-1}$ is only weakly bleached, suggesting it is only weakly involved in the transfer of energy through the dimer despite being directly hydrogen-bonded to the NH. The localization of this mode may contribute to the weaker intradimer coupling observed following excitation of the NH. It is also overlapping with the strong induced absorbance at 1800 cm^{-1} , which has the effect of making a weak signal appear even weaker.

As mentioned in the experimental section, the pump-probe and 2D spectra were all collected with the probe polarization parallel to the pump. The polarized pump beam only excites dipoles that are aligned with the polarization of the beam. From the heterodimer structure, it is clear that the C=O is not parallel with either the OH or NH modes, although it is also not completely perpendicular. The weak signal in the parallel polarization may be due in part to the transition dipole angle, however even when directly excited by the 1900 cm^{-1} pump, the carbonyl bleach is relatively weak. This indicates the carbonyl stretch is much more localized than the other vibrations involved in the hydrogen-bonded structure. In Figure 6.1 above, the signs of the carbonyl cross peaks match those of the coupled OH mode and the OH stretch modes. However, these cross peaks do not appear with every fingerprint mode like the OH modes. Since the pump intensity is quite low at 1700 cm^{-1} , these cross peaks may be too weak to see.

Centering a pump pulse over the carbonyl may provide more information. Figure 6.3 shows 2D IR spectra of the carbonyl diagonal and cross peaks in both parallel and perpendicular polarizations. The parallel spectra are the same data shown in Figure 6.1, expanded and with more contours to show the features of the carbonyl peak. In these, the carbonyl shows up as a diagonal peak following the 1900 cm^{-1} excitation, and a pair of slightly displaced cross peaks following the NH excitation. The NH and Fermi resonances couple separately with the two peaks of the carbonyl that appear in the linear infrared spectrum. The carbonyl is completely absent following the OH stretch excitation.

When probed in the perpendicular polarization, however, the carbonyl cross peaks all show up more strongly, while the diagonal peak is significantly weaker. The induced absorbances on either side of the carbonyl are quite weak in the perpendicular, even though the broad induced absorbance is very strong when measured in the parallel polarization. In the acetic acid dimer, Lim and Hochstrasser⁵⁴ observed that the anharmonicity shifted the $1\rightarrow 2$ transition only 8 cm^{-1} from the fundamental C=O stretch, while the carbonyl anharmonicity observed here in the heterodimer is nearly 30 cm^{-1} . While a larger anharmonicity is observed in the heterodimer than in the homodimer, the frequency of the fundamental vibration is nearly identical (see Figure 1.3). Combined with the weak pump-probe signal, the carbonyl stretch seems largely decoupled from the rest of the delocalized cyclic hydrogen bonded structure. This provides experimental evidence that ground state proton transfer is not occurring, since the proton would be transferring from the NH to this carbonyl, and would a large response from the carbonyl would be expected.

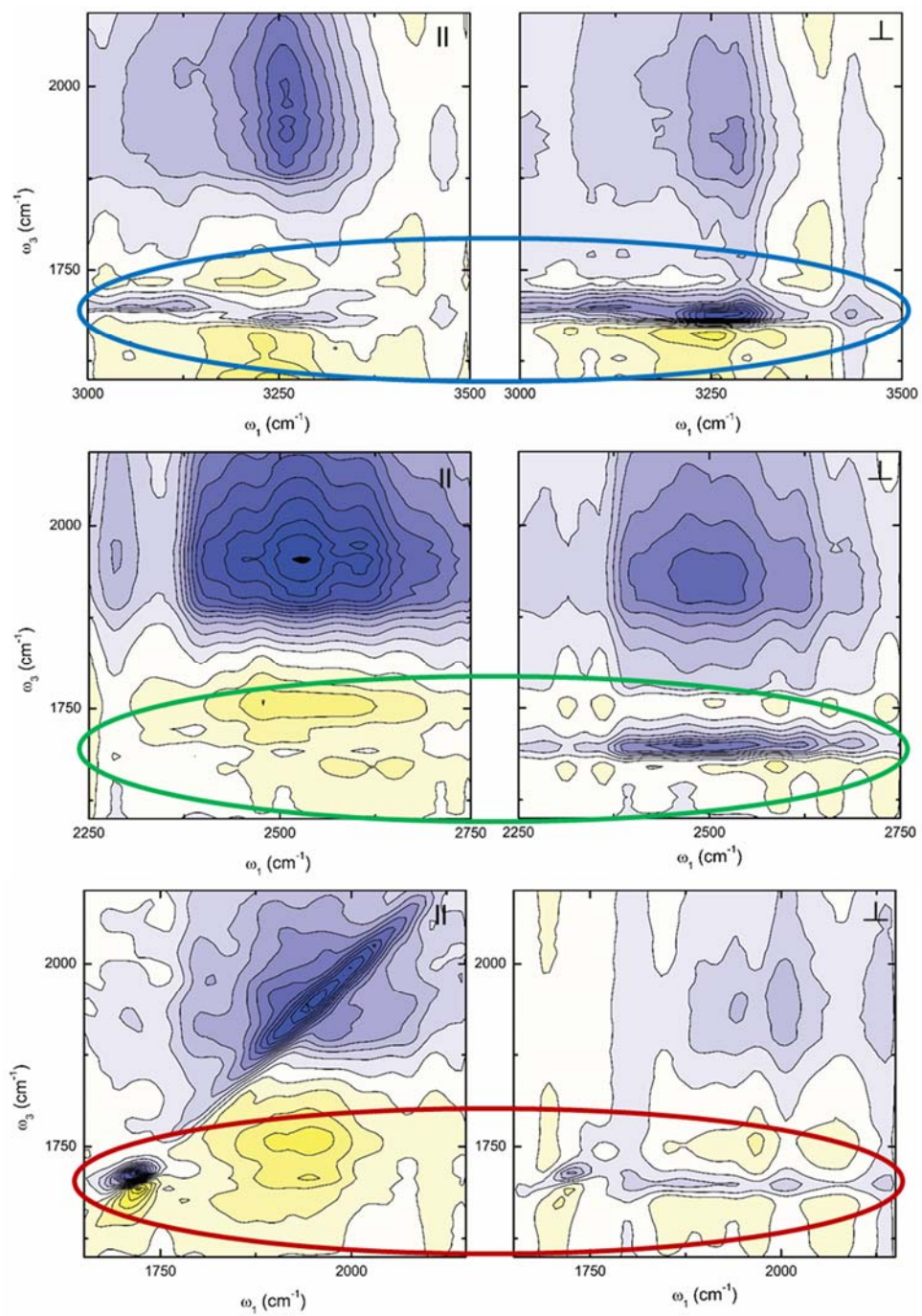


Figure 6.3: The carbonyl diagonal and cross peaks at each excitation pulse in parallel (left) and perpendicular (right) polarizations

6.4 Conclusions from 2D IR

2D IR spectra measured with a CIR probe pulse reveal strong and complicated coupling across the vibrational spectrum of the 7AI-Ac heterodimer. While virtually all of the fingerprint modes couple with the high frequency modes, these cross peaks vary across the excitation axis. The addition of 2D spectra to the transient IR measurements presented in the previous chapter confirms the strong coupling across the hydrogen-bonded intradimer interface.

CHAPTER 7

PHOTOINDUCED PROTON TRANSFER IN THE 7-AZAINDOLE HOMODIMER

7.1 Overview

As discussed in Chapter 1, proton transfer across hydrogen-bonded interfaces is vital to many biological processes. Photoinduced double proton transfer has been demonstrated in several model systems, including the 7AI homodimer,^{10,12,70} as shown in Figure 7.1. Various time-resolved electronic spectroscopies have been employed to understand the proton transfer, but the mechanism of this process remains controversial.^{23,25–27,33,34} While UV and visible spectroscopies are sensitive to electronic state transitions and solvent reorganization, vibrational spectroscopy directly probes the involved XH bonds. To explore this, we have studied the vibrational dynamics of the 7AI homodimer following UV excitation with UV pump-CIR probe spectroscopy.

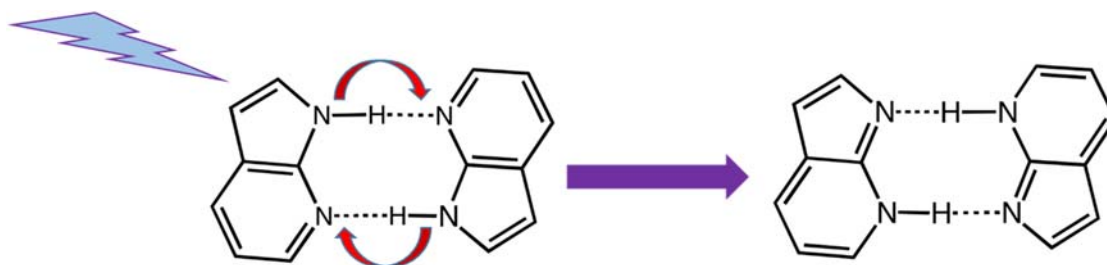


Figure 7.1: Photoinduced tautomerization of the 7-azaindole homodimer occurs following UV excitation.

Incorporating the UV pump into this experiment requires several experimental changes and technical developments. In this chapter, these experimental considerations, and the preliminary results of the UV pump—CIR probe experiment are discussed. While solvent effects complicate the spectrum, the transient vibrational spectrum confirms that the dimer is undergoing photoinduced tautomerization, and the results provide some insight into the dynamics of this process. Reproducing these results under different experimental conditions is necessary to confirm these preliminary results in order to draw definitive conclusions about the mechanism of proton transfer.

7.2 Experimental Considerations and Design

7.2.1 Generation of UV Pump

The 7AI homodimer undergoes double-proton transfer following excitation by a UV pulse.^{10,12} The UV absorbance spectrum of 7AI is shown in Figure 7.2, along with the spectrum of the pump pulse. The 300 nm pulse used to induce tautomerization is generated by quadrupling the signal output of a commercial OPA at 1200 nm, as shown in Figure 7.2. The 1200 nm pulse is first doubled to 600 nm in a BBO crystal (Castech, 21.4°, 0.4 mm thick), and then reflected through a pair of dichroic mirrors (Layertec, 104080) that transmit the 1200 nm pulse and reflect only the second harmonic. The 600 nm pulse is then transmitted through a second nonlinear crystal (BBO, Castech, 38.4°, 0.1 mm thick) and the harmonics are separated by another pair of dichroic mirrors (Layertec, 106163). The beam is focused with a lens (Thorlabs, 4158-UV, f=250 mm). Starting with 350 μ J of 1200 nm, this method produces about 1 μ J of 300 nm light.

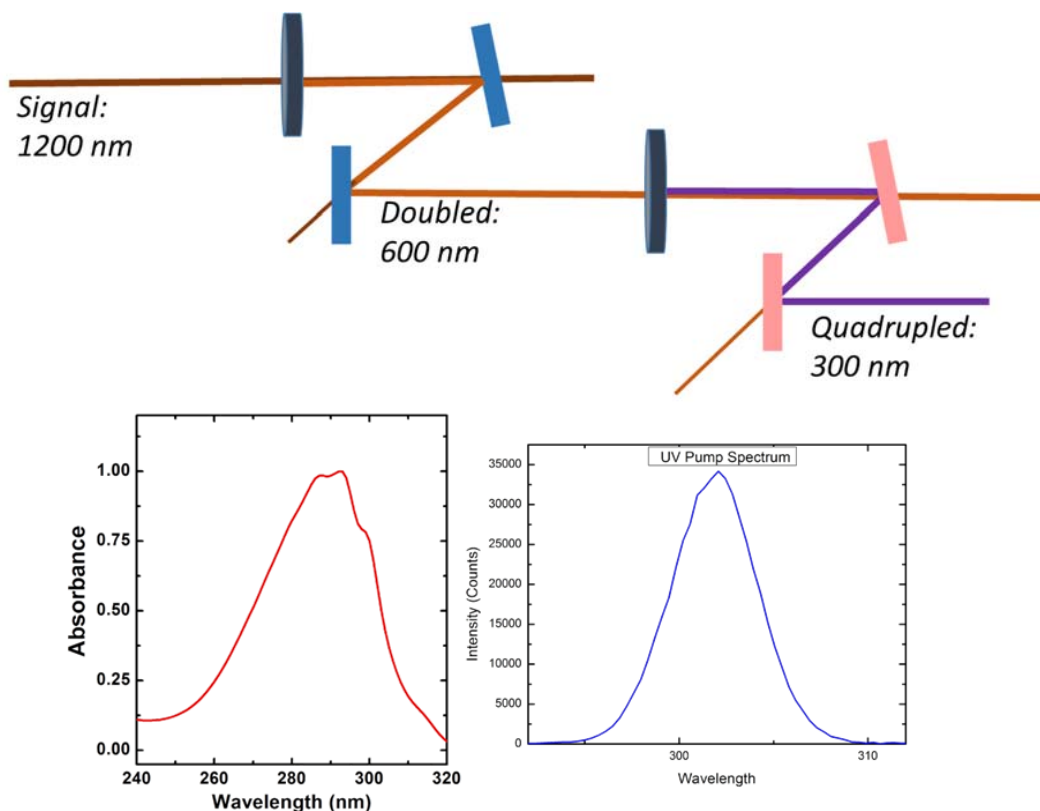


Figure 7.2: The generation of the 300 nm pump pulse by quadrupling of the 1200 nm signal beam (top), and the resulting pulse spectrum (bottom right) and the UV absorbance spectrum of the 7AI homodimer (bottom left).

7.2.2 Flowjet

UV excitation of the sample introduces additional experimental difficulties. First, the sample may degrade over time, which leads to two potential issues. In UV and visible experiments, the sample must be flowed continuously to prevent photodamage. This can be done in various ways. In some cases, a commercially available flow cell (DLC2, Harrick Scientific) can be used. However, a second issue caused by breakdown of the sample is the build-up of photoproducts on the sample windows, which can absorb and scatter both the pump and probe beams differently than the sample of interest. In addition, UV pulses produce large coherent artifacts in sample windows. To prevent

these issues, a windowless wire-guided flowjet, modified from a design by Bradforth and coworkers,¹²⁴ is used. The jet is shown in Figure 7.3 and consists of a cylindrical volumetric separatory funnel modified with a nozzle consisting of Viton tubing, a stainless steel reducing coupling, a stainless steel tube, and 0.005 to 0.007” diameter stainless steel wire.

A short (~1” long) loop of the wire is held between the compressed edges of the metal tube and connected to the fitting with a piece of Viton tubing. A second piece of Viton tubing is used on the other side of the fitting to connect the nozzle to the stem of the separatory funnel. The sample contained in the funnel is drained through the nozzle, creating a thin, windowless sample film. The flowing sample is drained into a reservoir and pumped back into the separatory funnel with a peristaltic pump.

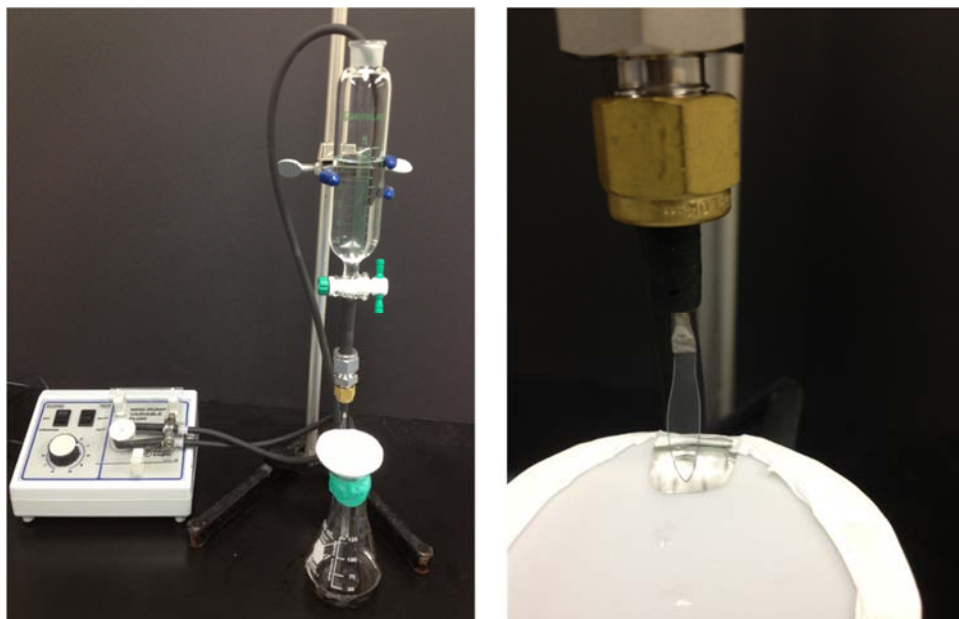


Figure 7.3: The flow jet used for flowing samples for the UV pump—CIR probe experiments (left) and a close-up of the nozzle with a thin film of solvent flowing through the wire loop (right).

7.2.3 Sample Considerations

While the IR excitation experiments in previous chapters were performed in carbon tetrachloride (CCl_4), the UV pump experiment requires a different solvent. Due to the windowless flowjet, solvent evaporation is increased, so a less volatile solvent is needed. Additionally, halogenated solvents are susceptible to photodissociation under UV excitation. For preliminary experiments, anhydrous cyclohexane was used. The vibrational spectrum of 7AI in cyclohexane and CCl_4 are compared in Figure 7.4. Since the CH stretch modes of the cyclohexane occur at frequencies within the broad dimer absorbance, deuterated cyclohexane will be used in future experiments. Since this may obscure some of the lower frequency peaks, experiments in both protonated and deuterated cyclohexane will likely be required to obtain a complete picture.

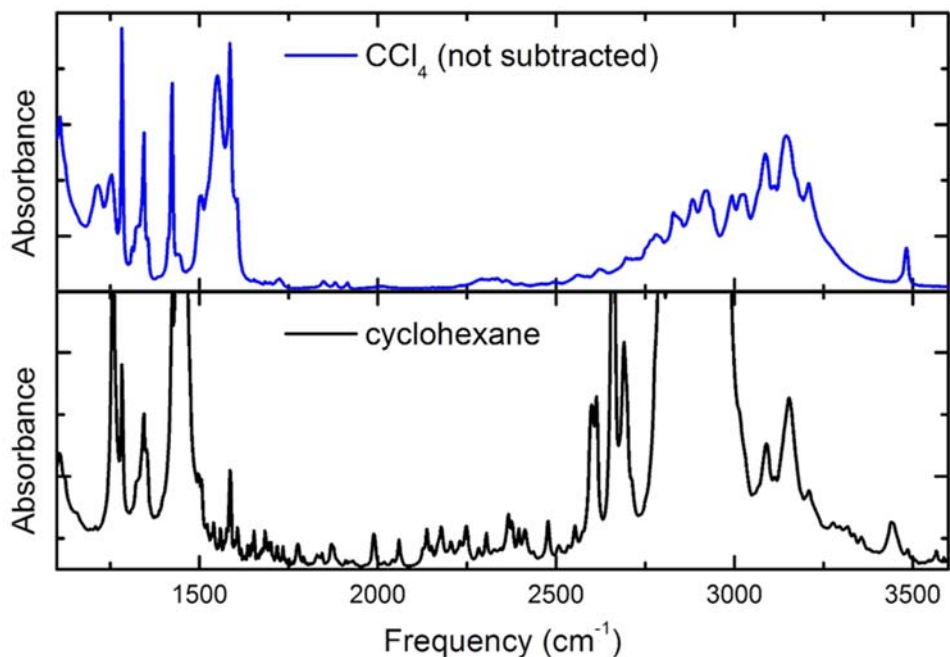


Figure 7.4: FTIR spectrum of the 7AI homodimer in both carbon tetrachloride and cyclohexane.

The sample concentration in this experiment was approximately 0.10 M 7AI (equivalent to a 0.05 M dimer concentration). The thickness of the film produced in the wire-guided jet is about 150 μm . Another consideration is the differing 7AI absorbance levels in the UV and IR. While the IR experiments have been carried out at dimer concentrations of 0.25 M, resulting in vibrational absorbances around 0.1 to 0.5 in a 100 μm sample, the UV absorbance is much stronger. If the pump pulse is absorbed entirely in only a small fraction of the sample, the remainder of the sample contributes only noise, not signal.

The sample concentration and thickness are then a compromise between having a strong enough signal to be measurable without adding unnecessary noise to the experiment. This can be controlled by the wire thickness of the flow jet and the actual sample concentration. The sample concentration in this case is limited by the solubility of 7AI in cyclohexane. Ideally, a saturated solution would be used to maximize dimer formation (relative to monomer concentration), but the free-flowing sample is subject to evaporation. As the solvent evaporates, the solute precipitates out of the solution, disturbing the flow of the sample, potentially clogging the jet, and reducing the smoothness of the sample film. As such, pure solvent is added to the sample regularly to maintain a relatively constant volume.

7.3 Preliminary Results

The preliminary UV pump—CIR probe spectrum is shown in Figure 7.5 along with transient spectra at time delays of 100 fs and 15 ps. The infrared spectrum is saturated by solvent peaks at two regions, 1450 and 2900 cm^{-1} , with additional strong absorbances (relative to the dimer) at 1255 and 2660 cm^{-1} . A reduced absorbance around 3120 cm^{-1} is seen to grow in over several ps, while the remainder of the high frequency spectrum is dominated by induced absorbances. Sharp negative and positive features can be seen at low frequencies, indicative of changing fingerprint modes. At short times (100 fs), much of the spectrum is dominated by a broadband induced absorbance, which is consistent with transferring protons. It is well-documented that the hydrogen bond strength significantly impacts the frequency of the covalent XH vibration.^{39,125}

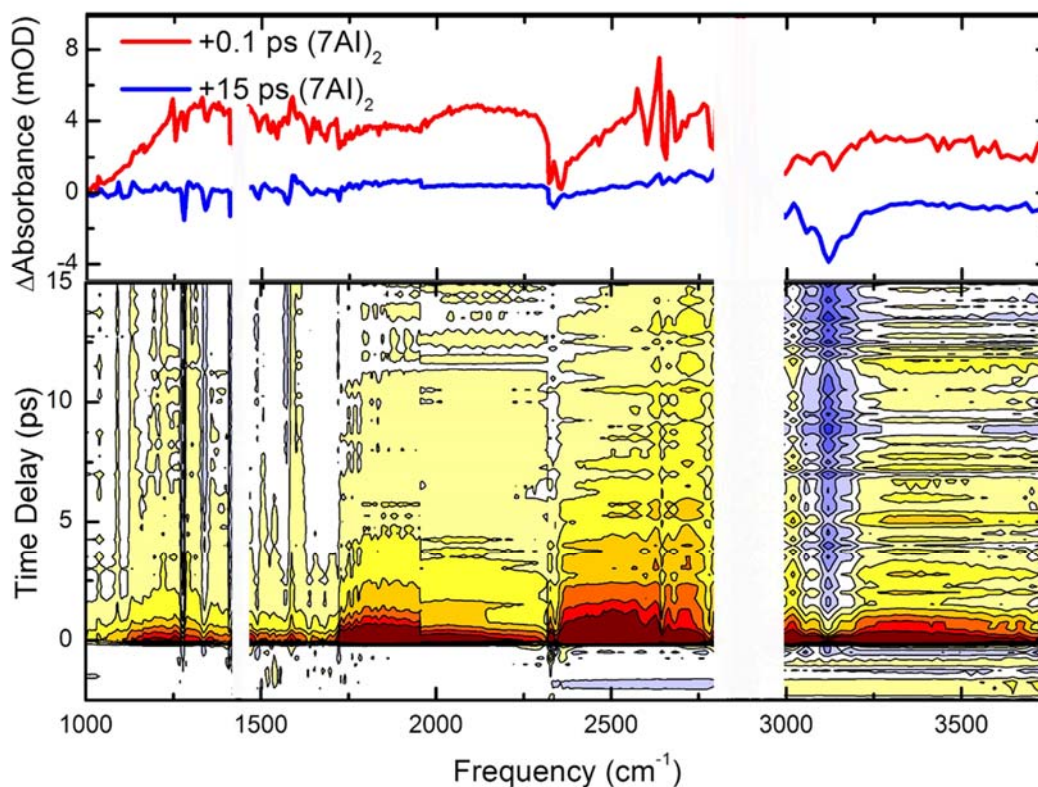


Figure 7.5: Transient spectra of 7AI homodimer at time delays of 0.1 and 15 ps (top), and as a function of time (bottom).

The moving proton during tautomerization will cause the NH peak to shift rapidly across much of the observable spectrum as the hydrogen bond strength modulates the NH frequency on an ultrafast time scale. The broadband induced absorbance occurs almost exclusively at lower frequencies than the dimer NH stretch, which is expected for a feature associated with weakening of the NH bond.

At late times (15 ps), the transient spectrum is the difference spectrum between the normal dimer and the proton transferred tautomer. No change is seen in the monomer peak following UV excitation, showing that while the dimer structure is altered, it is not simply broken into monomers. The bleach at 3120 cm^{-1} indicates the loss of the normal dimer. The corresponding induced absorbance of the tautomer is likely obscured by the cyclohexane absorbance, although some weak induced absorbances are still visible. The complicated Fermi resonance substructure will likely also change with the proton transfer, as both the N-H stretch and contributing overtones will shift. Simultaneously observing these shifts in both the high frequency and fingerprint regions may provide information on both proton transfer and the complicated vibrational spectrum of these dimers. As in the vibrational experiments, the fingerprint modes are narrower and more defined than the complex high frequency bands. This can be observed in the transient response probed from 1000 to 1800 cm^{-1} , shown in Figure 7.6.

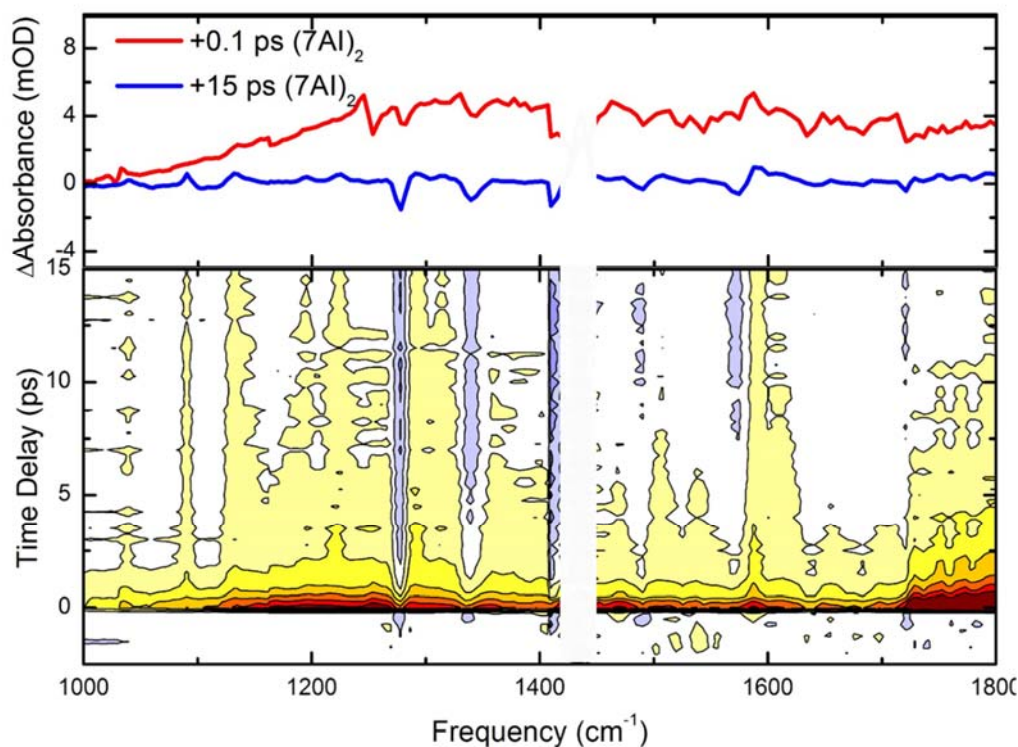


Figure 7.6: The transient response of the fingerprint modes measured from -2.5 to 15 ps in 250 fs steps shows the broad induced absorbance decay away while a few narrower fingerprint modes remain at long times. The cyclohexane saturates the spectrum at $\sim 1425 \text{ cm}^{-1}$.

Fingerprint modes are somewhat difficult to observe at short times due to the broadband induced absorbances, especially in the contour plot. In individual cuts of the spectrum, the peaks can be seen as sharp deviations from the smooth, broad positive feature. However, at late times, bleaches at 1275 and 1340 cm^{-1} become apparent. In the vibrational dynamics of the heterodimer, it was clear that the analogous modes are strongly influenced by the intradimer structure. In those results, a third strong peak was observed at 1430 cm^{-1} . While this region is obscured by the strong cyclohexane absorption, bleaches are observed on either side, at 1410 and 1490 cm^{-1} .

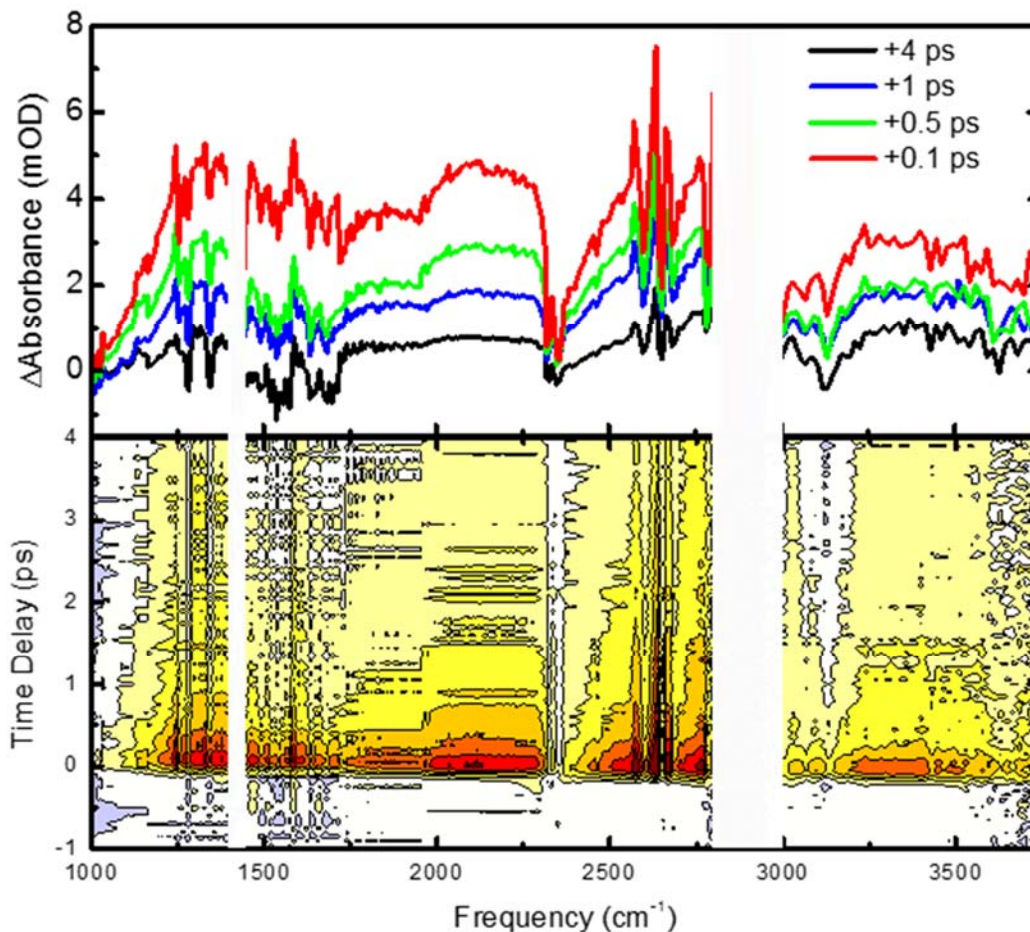


Figure 7.7: Pump-probe spectrum measured from -1 to 4 ps in 50 fs steps (bottom) and transient spectra at time delays of -1, 0.1, 0.5, 1 and 4 ps (top). The cyclohexane saturation is blocked at ~ 1425 and 2900 cm^{-1} .

Since visible experiments have resulted in time scales of 200 and 1100 fs, the short time response was measured with greater temporal resolution. A pump-probe spectrum was scanned from -1 to 4 ps in 50 fs steps and is shown in Figure 7.7, along with transient spectra at -1, 0.1, 0.5, 1 and 4 ps.

The pure solvent also shows a transient response. In the dimer transient spectra, small peaks with rapid dynamics, such as those at 1255 and 2377 cm^{-1} , correspond to linear absorbance peaks in the cyclohexane and are likely due to photolysis of the solvent.^{126,127} Reducing the power of the UV pulse should eliminate this effect, but will

also reduce the signal strength of the dimer response. Creating a thicker film by using a larger diameter wire in the nozzle could increase the signal while decreasing the solvated electron effect. This possibility was explored, but the thicker jet was more prone to surface disruption that introduced noise and artifacts to the signal. Another possibility is to increase the spot sizes of the laser beams at the sample rather than decreasing the overall power. This will reduce the energy density (and the solvent photolysis) but measure the weaker response over a greater sample area, increasing the total signal.

One feature of experimental interest is the much smaller chirp across the spectrum, shown in Figure 7.8. The temporal walkoff in the IR experiments presented in Chapter 5 was about 300 fs, but is reduced to less than 100 fs here since the pulses in this study were not transmitted through a 1 mm CaF₂ sample window. The only material the CIR pulse is transmitted through after generation is the 500 μm silicon that filters the fundamental 800 nm and its harmonics. The dispersion from these substrates was discussed in Chapter 3. Unlike the heterodimer experiments, this UV pump study was not purged with dry, CO₂ free air, so the effect of atmospheric absorbances on the spectrum and pulses can also be seen at short times.

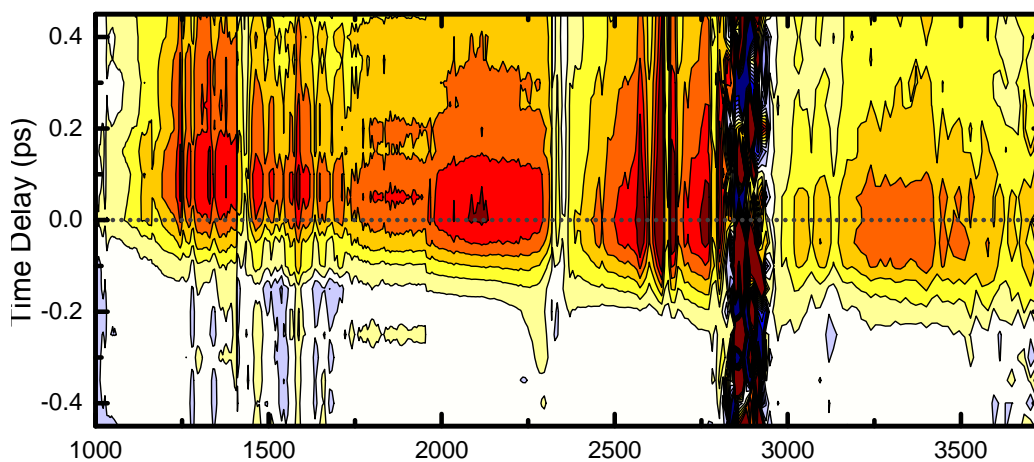


Figure 7.8: The 7AI homodimer transient response from -450 to 450 fs shows the fast rise time and small chirp across the entire spectrum.

7.4 Conclusions and Future Directions

We have demonstrated how ultrafast mid-IR continuum spectroscopy can be applied to interpret the mechanism of proton transfer in cyclically hydrogen-bonded model systems using UV pump-CIR probe experiments. While the data is consistent with the tautomerization of the 7AI homodimer, several more issues need to be resolved to draw definitive conclusions on the mechanism of proton transfer. Since acquiring this data, several improvements have been made in the continuum generation, data acquisition, and experimental design that will increase the signal-to-noise and provide a clearer picture of proton transfer. With other experimental issues resolved, this study can be repeated in another solvent and at lower pump powers, which should reduce or remove the experimental artifacts. After the homodimer has been characterized, the same method can be applied to other model systems, such as the heterodimer studied extensively in Chapters 4, 5, and 6, and eventually on biologically important systems, such as DNA base pairs.

CHAPTER 8

GENERATION OF MICROJOULE MID-INFRARED SUPERCONTINUUM PULSES IN CHALCOGENIDE GLASSES

8.1 Overview

Nonlinear optical spectroscopies focused on molecular vibrations and intraband transitions require high-energy [several microjoule (μJ)] laser pulses in the mid-IR. Current methods of generating such pulses provide either high-energy laser pulses with a limited spectral bandwidth or low-energy laser pulses with broad spectral coverage, such as that described in Chapter 3 and used in the work presented in Chapters 4 through 7. While that pulse has been successfully used as a probe pulse in nonlinear spectroscopy, it is not strong enough to act as a pump pulse. This chapter presents the generation of high-energy mid-IR supercontinuum laser pulses by focusing 70 fs, 30 μJ mid-IR pulses in commercially-available bulk chalcogenide glasses. The resulting supercontinuum pulses exhibit pulse energies of several μJ , remain temporally short, and span more than two octaves from less than 2.5 μm to more than 10 μm at the 20 dB level. This facilitates capturing most of the fundamental mid-infrared vibrational transitions from 1000 to 4000 cm^{-1} in a wide range of applications including nonlinear optical spectroscopy. This is demonstrated by incorporating the pulse into our sum frequency generation experiment, producing the broadest SFG spectrum generated with a single experiment.

8.2 Background

8.2.1 Pulses for Nonlinear Infrared Spectroscopy

Nonlinear optical spectroscopy requires short, high-energy (several μJ) laser pulses, but generating mid-IR pulses with wide spectral coverage and high energies simultaneously is challenging. High-energy mid-IR pulses for nonlinear mid-IR spectroscopy are typically generated through nonlinear mixing of the outputs of optical parametric amplifiers (OPAs) and span only a few hundred nm. Nonlinear spectroscopic experiments can be performed by scanning the spectral envelope of such pulses over a wide spectral region, but this is a time consuming process and introduces additional technical difficulties, such as correcting for changes in the beam pointing and temporal overlap.^{76,90,128} Recently, fs mid-IR supercontinuum laser pulses spanning the entire vibrational range (<2.5 to >16.5 μm) were generated by focusing multiple fs pulses of different wavelengths in the near-IR through ultraviolet range in gases.^{79,109,110,108} While this offers a great advantage for probing the vibrational spectrum, these sub- μJ continuum mid-IR light pulses are only intense enough to act as probe pulses,^{67,79,85} and not strong enough to use as excitation pulses in time-resolved and nonlinear spectroscopies.

8.2.2 Mid-Infrared Supercontinuum Generation in Materials

Supercontinuum generation in solids has been extended into the mid-IR by the use of various mid-IR transparent materials. This includes the generation of spectrally broadened pulses in fibers and waveguides^{129–148} and by propagation through bulk materials.^{149–156} However, none of these studies have resulted in μJ pulses covering

more than two octaves in the fundamental and fingerprint vibrational frequency range, and to our knowledge have not been incorporated in nonlinear optical applications.

Several materials have been used to generate supercontinua spanning from the visible and into the mid-IR range. Supercontinuum generation has been demonstrated in both tellurite and ZBLAN using readily available NIR incident pulses. However, these materials are limited by transmission at the long wavelength edge and the majority of the supercontinuum power is contained within the NIR range.¹³⁰ In fibers, spectral broadening in these materials extends to about 4.5 μm .^{129–131} (For direct comparison throughout this chapter, all bandwidths will be given at a 20 dB level unless otherwise noted.) These sources have the potential to probe vibrational overtones in the NIR and high-frequency fundamental transitions, but cannot probe lower frequency fundamental modes or fingerprint modes. Liao et al^{149,150} extended this range as far as 6.1 and 7.4 μm using bulk fluoride and tellurite glasses, respectively, but with optical damage to the material, and Silva et al¹⁵² generated a supercontinuum in a YAG plate that spans from 2500-4000 nm at 20 dB (reported as 450 to 4500 nm at 35 dB).

Chalcogenide glasses have been studied extensively due to their transmission across the full mid-IR range, including the fingerprint region (6-20 μm). Supercontinua generated in chalcogenide fibers can cover the full vibrational spectrum and have recently approached μJ pulse intensities.^{132–148,156} Recently, Bang and coworkers¹³² reported a spectrum spanning 1.4-13.3 μm in a chalcogenide fiber, but the energy of these pulses was limited to 150 nJ, an average power of 150 μW at 1 kHz. Although high average power can be obtained at high laser repetition rates,^{138,144} nonlinear optical applications require high peak power. The highest energy supercontinuum pulses

generated in fibers were demonstrated by Theberge et al,¹³³ and extend from the NIR to approximately 7 μm with pulse energies up to about 0.5 μJ in As_2S_3 fibers.

In bulk chalcogenides, supercontinua have been generated with a variety of pump durations and wavelengths. This was first demonstrated by Corkum et al¹⁵³ in 1985 by propagating high energy, 9.3 μm ps pulses through 6 cm thick GaAs. Pigeon et al¹⁵⁴ used 10 μm , ps pulses to generate broadening from 2 to 20 μm at the 50 dB level. While supercontinua generated by ps pulses can be quite broad, the broadened spectral components are several orders of magnitude less intense than the transmitted pump pulse. In 2009, Ashihara and Kawahara¹⁵⁵ generated a spectrum spanning 3.5 to 7 μm by propagating 5 μm , fs pulses with several μJ energies through a 5 mm sample of bulk GaAs. While an anti-reflection coating on the substrate increased linear transmission, nonlinear absorption causes losses of up to 80%, resulting in sub- μJ continuum pulses. Recently, Lanin et al¹⁵⁷ demonstrated broadening of 5 to 10 μm at 20 dB (reported as 3-18 μm at 60 dB) of a 2 μJ incident pulse in 5 mm GaAs. This technique was extended to other chalcogenide materials by Yu et al,¹⁵⁶ who demonstrated broadening of several μJ , 150 fs, 5.3 μm pulses in $\text{Ge}_{11.5}\text{As}_{24}\text{S}_{64.5}$ that spanned at least 2.5 to 7.5 μm .

8.3 Method

Here we present the first demonstration of the generation of supercontinuum pulses spanning more than two octaves in the mid-IR with energies of several μJ and higher and demonstrate the use of these pulses in nonlinear spectroscopy. This is achieved by focusing high-energy fs mid-IR laser pulses through 2 mm thick windows of several commercially-available chalcogenide glasses, which are transparent in the

mid-IR wavelength range. This provides a method for generating continuum mid-IR laser pulses spanning almost the entire fundamental mid-IR vibrational spectrum that can be readily implemented with the technologies already available in many ultrafast laboratories.

A schematic of the experimental set-up used to generate high energy mid-IR supercontinuum pulses is shown in Figure 8.1. A commercial OPA (Coherent OPerA Solo) is pumped by 1 kHz, 3.3 W, 25 fs, 800 nm pulses from a regenerative Ti:sapphire amplifier (Coherent Legend Elite Duo). Mid-IR pulses with a spectral bandwidth around 300 cm^{-1} , pulse energy of $30\text{ }\mu\text{J}$, and pulse duration of approximately 70 fs are generated by non-collinear DFG mixing of the OPA output. These mid-IR pulses with a beam diameter of 4 mm are focused through a chalcogenide window and re-collimated using off-axis parabolas ($f=101\text{ mm}$, protected gold), with the chalcogenide placed in the optical path near the focus of the incident pulses.

To prevent optical damage, the material is continuously moved in the two lateral dimensions using motorized actuators (Newport NewStep). The generated spectra were measured with the MCT array detector (IR Associates/IR Systems) described in Chapter 3. Two gratings were used to measure the spectra: 58 grooves/mm blazed at $3.6\text{ }\mu\text{m}$ and 30 grooves/mm blazed at $8\text{ }\mu\text{m}$. The monochromator is equipped with order-sorting filters from $2.44\text{ }\mu\text{m}$ to $13\text{ }\mu\text{m}$.

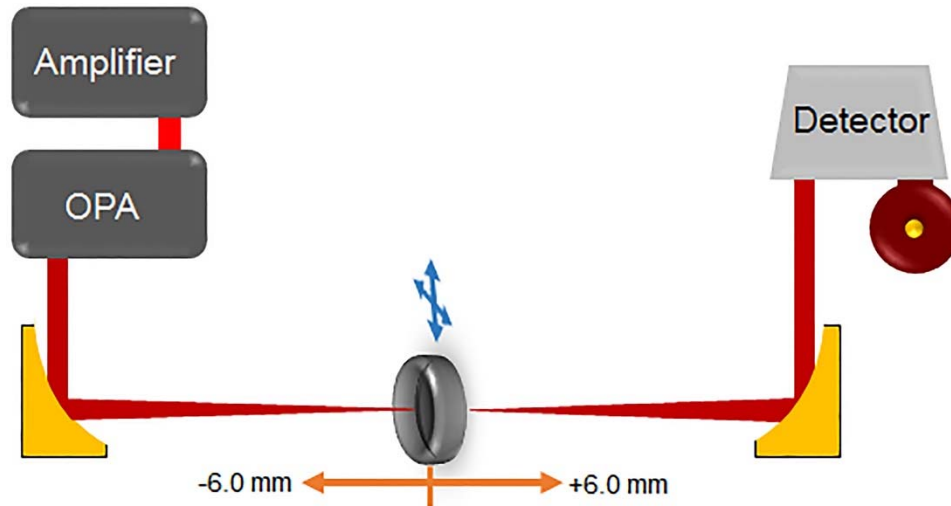


Figure 8.1: Experimental set-up for generation of mid-IR supercontinuum pulses in bulk chalcogenide glasses

We have tested five different chalcogenide glasses (IG2, IG3, IG4, IG5, and IG6) acquired from Naked Optics. Each glass window was 2 mm thick and 1 inch in diameter. The composition of the chalcogenide glasses, as given by the manufacturer, are $\text{Ge}_{33}\text{As}_{12}\text{Se}_{55}$, $\text{Ge}_{30}\text{As}_{13}\text{Se}_{32}\text{Te}_{25}$, $\text{Ge}_{10}\text{As}_{40}\text{Se}_{50}$, $\text{Ge}_{28}\text{Sb}_{12}\text{Se}_{60}$, and $\text{As}_{40}\text{Se}_{60}$, respectively. In this study we examine the supercontinuum generation dependence on glass composition, incident wavelength, and incident pulse power density, which is controlled by translating the window relative to the focus.

8.4 Results

Figure 8.2 shows the pulse spectra generated in each of the glasses, measured on the two different gratings, with the glasses 3.5 mm in front of the focus of the 3750 nm incident pulse. For all experiments, the incident pulse energy was held at 30 μJ ,

corresponding to a peak power of 430 MW. At a distance of 3.5 mm from the focus, the beam spot is approximately 425 μm , corresponding to an energy density of 300 GW/cm².

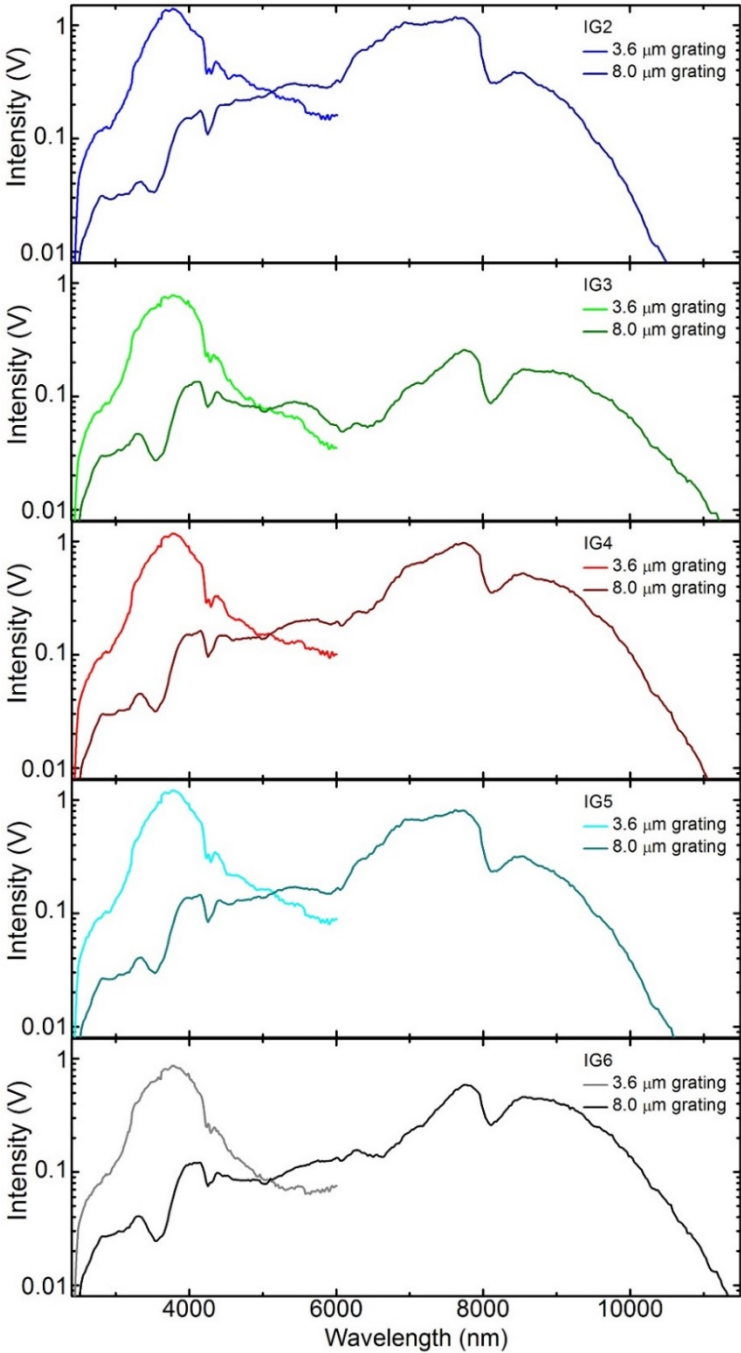


Figure 8.2: Spectra of mid-infrared supercontinuum generated in the chalcogenide glasses, measured on both spectrometer gratings with glasses located 3.5 mm in front of the focus of the 30 μJ , 3750 nm incident pulse

As the figure illustrates, the generated laser pulses cover the spectral range from <2.5 to $11 \mu\text{m}$ at about the 20 dB. At the 10% level, which is more relevant to spectroscopic applications, the bandwidth spans 2.5 to $10 \mu\text{m}$. This corresponds to 1000 to 4000 cm^{-1} , covering most of the fundamental vibrational frequency range including the fingerprint region. The supercontinua generated in the different glasses are qualitatively very similar. It is difficult to capture the full spectral shape of continuum infrared pulses due to the limited spectral bandwidth of the detecting optics. The grating efficiency, in particular, limits the measured spectrum. The sharp cutoff at short wavelengths is caused by the 2440 nm order sorting filter in the monochromator.

The overall pulse energy is significantly reduced after propagation through the chalcogenide glass due to multiphoton absorption, which also causes problems with photodamage. IG2 and IG6 were chosen for further study. The energy of the supercontinuum generated in IG2 is highest of the five glasses, while IG6 produces the broadest spectrum without burning. IG3 has the broadest spectrum but a lower damage threshold and produces lower energy supercontinuum pulses.

The generated pulse spectra depend on the energy density of the incident light, which we vary by changing the position of the material with respect to the focus of the incident laser pulses. As the IR-transparent material is moved closer to the focus of the incident beam, greater spectral broadening and decreased pulse energy is observed. This provides some flexibility in the spectral coverage versus pulse energy that can be tailored to a given application. The pulse energies as the glass is varied from 6 mm in front of to 6 mm behind the focus are listed in Table 8.1 and the associated spectra for IG2 and IG6 are shown in Figure 8.3.

Table 8.1. Pulse Energies (μJ) of Supercontinuum Pulses Generated in Chalcogenide Glasses at Positions Relative to the Focus of the Incident 3750 nm Beam and Estimated Spot Size at Each Position)

Distance	Spot Size	IG2	IG3	IG4	IG5	IG6
-6.0 mm	520 μm	9.6	--	--	--	6.2
-3.5 mm	425 μm	5.7	3.0	4.9	5.3	3.8
0.0 mm	300 μm	3.9	1.9	3.0	--	2.2
+1.0 mm	335 μm	4.1	--	--	--	2.7
+3.5 mm	425 μm	6.3	3.1	5.1	5.5	4.2
+6.0 mm	520 μm	7.0	--	--	--	4.6

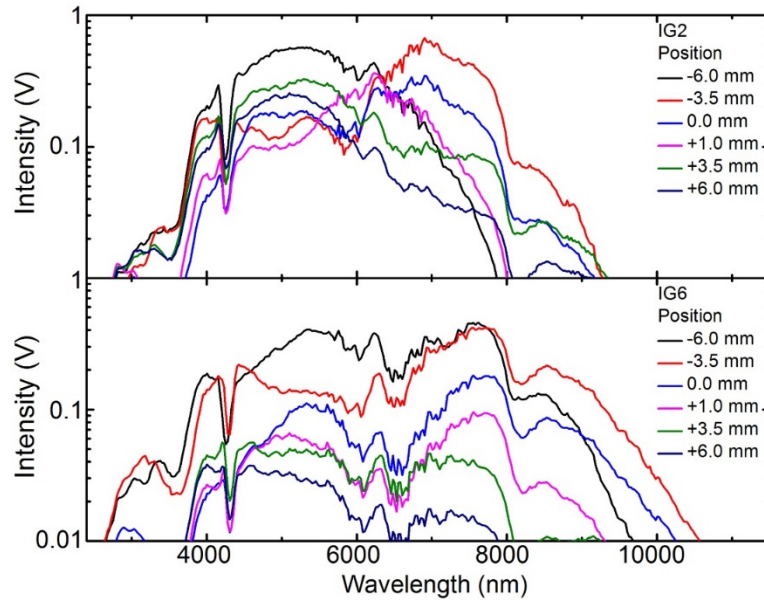


Figure 8.3. Mid-infrared supercontinuum generated in IG2 (top) and IG6 (bottom) as a function of glass position with an incident 30 μJ , 3750 nm pulse

When the material is near the focus of the incident beam, the transmitted supercontinuum pulse energies are around 10% of the incident energy. As the material is moved farther away from the focus, resulting in a narrower spectrum, the pulse energy increases to about half. The loss far from the focus is mostly due to reflection loss at normal incidence. Putting the material at Brewster's angle should minimize the reflection loss and increase the pulse energy but has the additional complexity of having to move the material in two dimensions without translating the material along the beam propagation direction. Anti-reflection coatings have been demonstrated to decrease the reflection loss and increase the energy of the generated supercontinuum pulse, but nonlinear absorption loss remains significant, reducing the transmitted energy to as little as 20% of the incident pulse.¹⁵⁵ When the focus exists in the material, damage to the optical surface occurs despite lateral translation of the sample. For IG2 and IG6, positioning the glass 3.5 mm in front of the focus of the incident pulses produced the widest pulse spectrum without damaging the windows. The pulse energies obtained here were 5.7 and 3.8 μJ , respectively, which are strong enough for nonlinear optical applications.

The generated pulse spectrum depends greatly on the wavelength of the incident laser pulses. Figure 8.4 shows the generated pulse spectra in IG2 and IG6 with incident wavelengths of 3750 nm, 4000 nm, and 5000 nm. Using incident pulses of shorter wavelengths leads to rapid photodamage that cannot be prevented by translating the material in the lateral dimensions. Increasing the input wavelength results in less broadening to shorter wavelengths, but higher output energy of the supercontinuum pulse.

Compared to methods based on non-linear mixing in gases, this approach provides about an order of magnitude higher overall pulse energy. However, since most of the energy in the previous method was at long wavelengths beyond our detection range, the new method produces about 3 orders of magnitude higher spectral intensity (intensity per wavelength unit) in the mid-IR range. This is demonstrated by the mid-IR array detector registering the same number of counts at 4 μm using the new method with a neutral density filter with an optical density of 3, as the previous method without a neutral density filter.

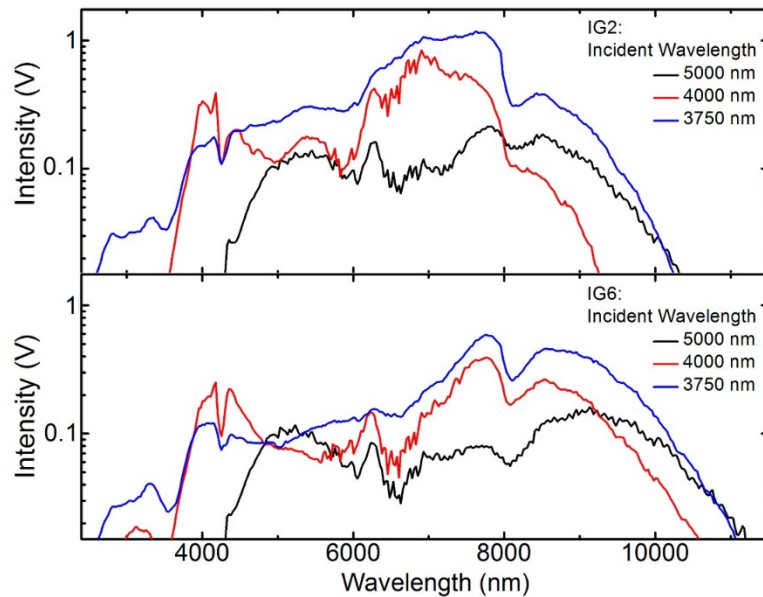


Figure 8.4. Broadening of mid-infrared supercontinuum generated in IG2 (top) and IG6 (bottom) as a function of the input wavelength, with the window located 3.5 mm in front of the focus of the incident pulse. Incident pulse energies were held constant at 30 μJ .

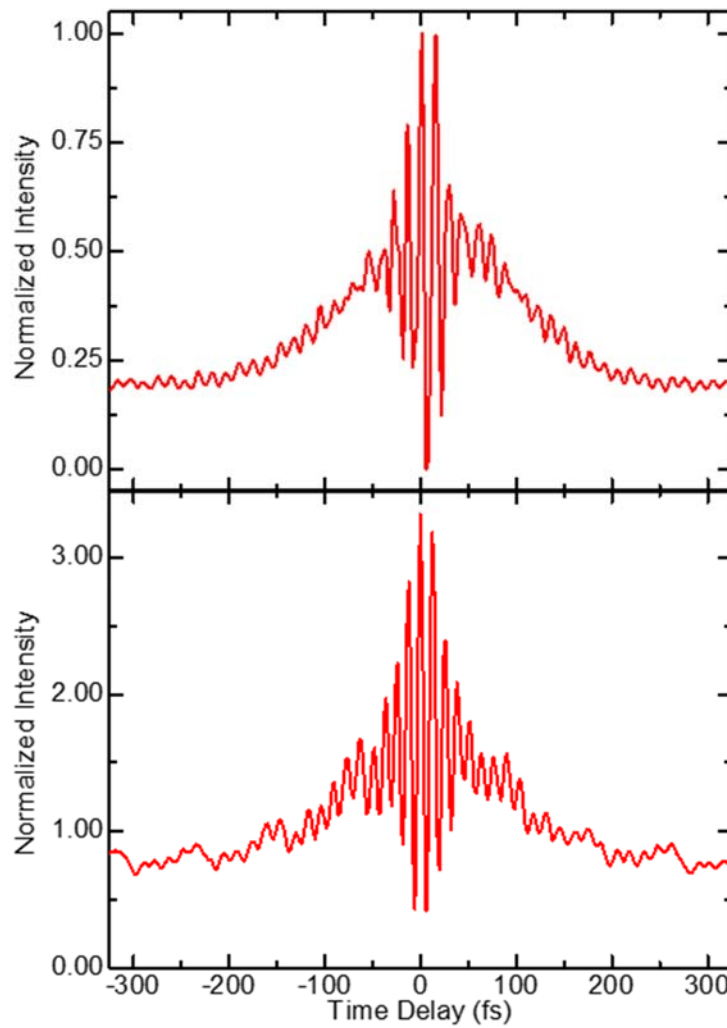


Figure 8.5: Second order autocorrelation of the supercontinuum pulses generated in IG6 in a 0.3 mm thick GaSe crystal with no compression (top) and with 13 mm CaF2 in the beam.

The broadening of high intensity, short mid-IR laser pulses propagated through bulk material is due primarily to self-phase modulation with other nonlinear processes, such as stimulated Raman scattering, generation of harmonic frequencies, and four-wave mixing also contributing to the increased spectral bandwidth of the pulse.^{152–155,157} As a result of these processes and nonlinear dispersion, the pulse duration is lengthened

by propagation through the chalcogenide material. Figure 8.5 shows the second order autocorrelation in a 0.3 mm thick GaSe crystal of the supercontinuum pulse generated in IG6, illustrating that the pulses, although chirped, remain relatively temporally short. The pulses can be compressed by propagating the pulses through other materials, using optical prisms, or a pulse shaper.^{116,117,158} This is demonstrated in Figure 8.5 by putting 13 mm of CaF₂ into the beam after supercontinuum generation. The tails on the edge of the autocorrelation are suppressed due to a more compressed pulse, but have steps due to surface reflections in the series of CaF₂ windows required to achieve a total of 13 mm.

8.5 Supercontinuum Sum Frequency Generation

The supercontinuum pulse generated in IG6 was incorporated into our sum frequency generation experiment^{159–161} and used to measure the non-resonant SFG spectrum of gold and the resonant surface vibrational spectrum of a collagen film, shown in Figure 8.6.

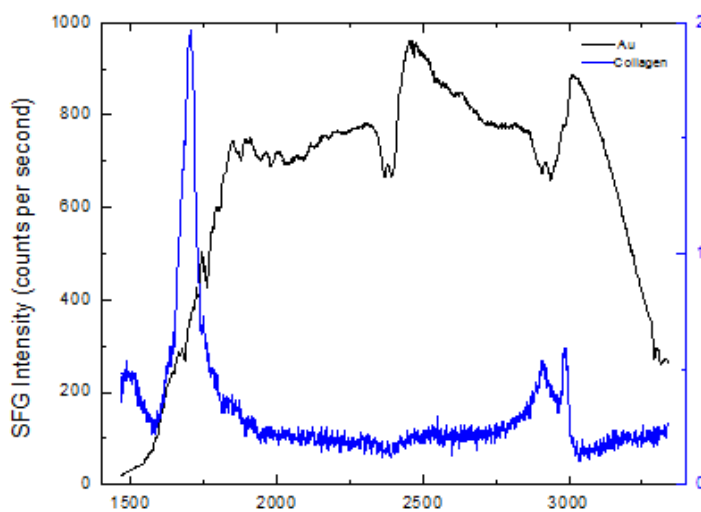


Figure 8.6: SFG spectrum of gold (black) and collagen (blue) measured with supercontinuum pulse generated in IG6.

The up-converted spectrum, while not as broad as the IR spectrum measured directly, represents the broadest SFG spectrum to date, spanning from the amide I band to the CH stretch vibrational region.

8.6 Conclusions and Future Prospects

In summary, we have generated mid-IR supercontinuum pulses of several μJ pulse energy spanning more than 2.5-10 μm using commercially available chalcogenide glasses and technologies already available in many ultrafast laboratories, and demonstrated the use of this pulse in sum frequency generation. The generated supercontinuum pulses are chirped due to self-phase modulation and dispersion in the chalcogenide glass but remain temporally short. The high-energy and short duration of these mid-IR supercontinuum pulses facilitates nonlinear optical applications for advanced spectroscopic characterization. Further nonlinear spectroscopic experiments, including optimization of sum-frequency generation spectroscopy and 2D IR, utilizing the high energy mid-IR supercontinuum pulses are currently underway.

While our current CIR probe method expands traditional 2D IR to cover the full spectrum in the probe axis, high energy continuum pulses open up the possibility of also exciting the full spectrum. Since 2D IR is frequency-resolved in the excitation axis, this method would reveal couplings across the entire spectrum in both dimensions with a single experiment. As such, the supercontinuum pulse generation described here has the potential to increase the information gained by 2D IR experiments while simultaneously reducing data acquisition time.

CHAPTER 9

CONCLUSIONS AND FUTURE PROSPECTS

9.1 Summary

An ultrafast mid-infrared continuum laser pulse has been incorporated as the probe pulse in several vibrational spectroscopies and used to study the vibrational dynamics and proton transfer of cyclic, hydrogen-bonded dimers. Unlike traditional ultrafast vibrational spectroscopy, which is limited to a few hundred cm^{-1} of bandwidth in a single experiment, ultrafast mid-IR continuum spectroscopy allows vibrational dynamics and coupling to be observed across the full vibrational spectrum. The vibrational dynamics of the 7AI—Ac heterodimer were studied with IR pump—CIR probe and 2D IR, while photoinduced proton transfer has been studied in the 7AI homodimer with UV pump—CIR probe experiments. Additionally, the development of high energy ultrafast continuum mid-IR pulses that could be used as excitation pulses has been explored.

9.2 Ultrafast Vibrational Spectroscopy of the 7AI-Ac Heterodimer

The dynamics and couplings of the 7AI—Ac heterodimer have been explored in detail. Preliminary results and a comprehensive pump-probe and 2D IR study indicate strong coupling across the spectrum and very fast energy transfer across the bridging hydrogen bonds. While the pump-probe experiments provided interesting dynamic information, the 2D IR spectra provided evidence of the largely homogeneous coupling across the spectrum.

A significant advantage of 2D IR spectroscopy is the ability to frequency-resolve the excitation axis. This can often be used to identify and understand the coupling of

different vibrational modes in a molecule, as shown in RDC and N749 Black Dye in Chapter 2. However, ligands on metal centers are much simpler systems with very few vibrational modes relative to the complicated dimers studied here. Ideally, the 2D IR spectra of these dimers would reveal clear couplings between specific modes, especially between the Fermi resonances and fingerprint modes. Instead, the very strong coupling presents as nearly homogeneous peaks spanning most of ω_1 . This suggests that considering only normal modes or coupling between otherwise isolated modes will be insufficient to explain the complex energy pathways and couplings of these systems.

9.3 Proton Transfer in the 7AI Homodimer

The potential for UV pump—CIR probe spectroscopy has been demonstrated in the 7AI homodimer. Several technical advances and modifications were undertaken to make this experiment possible. Despite some experimental limitations, the results indicate the ultrafast movement of protons across the hydrogen-bonded interface and show the formation of the doubly proton-transferred tautomer. This demonstrated the use of UV pump—CIR probe experiments to track moving protons, and progress has since been made in overcoming the remaining limitations to make this experiment widely applicable.

9.4 Future Prospects for Ultrafast Continuum IR Spectroscopy

9.4.1 Limitless Applications of Ultrafast CIR Spectroscopy

The work presented here demonstrates the development of ultrafast continuum mid-IR spectroscopy as a valuable tool for studying the vibrational dynamics of complex systems. With the information gained over the course of these experiments and the use of the widely tunable (<300 nm to 15 μm) pump, these techniques can be applied to virtually any system to probe the vibrational spectrum.

9.4.2 IR Pump—CIR Probe

Although the continuum probe is well-suited for studying proton transfer and the characteristically broad spectra of hydrogen-bonded systems, it also offers information across the full vibrational spectrum for any system. This experimental technique also provides benefits when probing the entire spectrum is not necessary or informative. The IR pump—CIR probe experiment can be used to probe any region or regions of the spectrum following the tunable pump. It can be employed as a traditional one-color experiment, as demonstrated in Chapter 2, where this method was used to probe a small frequency range to study the vibrational dynamics of N749 Black Dye and the coupling of RDC. The CIR probe also enables performing a two-color experiment (or a series of two-color experiments) without having to independently tune the frequencies of both pulses. This is useful for systems with broad features that span more than the bandwidth of an OPA pulse, or with multiple features that are separated by more than a few hundred cm^{-1} . The ability to scan the CIR probe over the full vibrational spectrum to look for unexpected transient features is another advantage over traditional transient IR experiments. The IR pump—CIR probe experiment is ideal for systems with broad vibrational spectra that are not well-defined, such as bulk water or the excess proton in water.^{85,86,120,162–164} The structure and solvation of the proton is expected to convert rapidly between Zundel and Eigen structures shown in Figure 9.1.

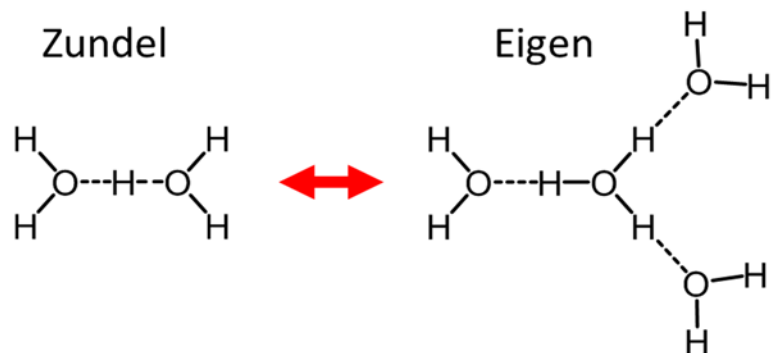


Figure 9.1: The Zundel and Eigen structures for the excess proton in bulk water

Each of these structures has broad vibrational features spread across the infrared spectrum. Using the tunable IR pump, we can pump various features, such as the Zundel proton at 1200 cm^{-1} , the Eigen stretch at 2700 cm^{-1} , or the water stretch at 3500 cm^{-1} , and observe the dynamics and couplings across the full spectrum with both IR pump—CIR probe and 2D IR experiments.⁸⁶ In this manner, we can preferentially excite the one of the structures and see interconversion between the excess proton structures and bulk water.

9.4.3 UV Pump—CIR Probe

This includes reproducing and expanding the proton transfer experiment in other solvents and with other dimers of interest, including the 7AI—Ac heterodimer and actual DNA base pairs. This technique also has the potential to probe the moving protons in numerous other systems, such as photoacids and hydrogen-bonded bulk systems. Photoacids release a proton following excitation, which has the effect of significantly changing the pH with light. Whether the proton travels directly from donor to acceptor or is mediated through the solvent remains controversial. Previous studies have observed the proton leaving the acid or arriving at the base, but have not been able to watch the moving proton.^{165,166}

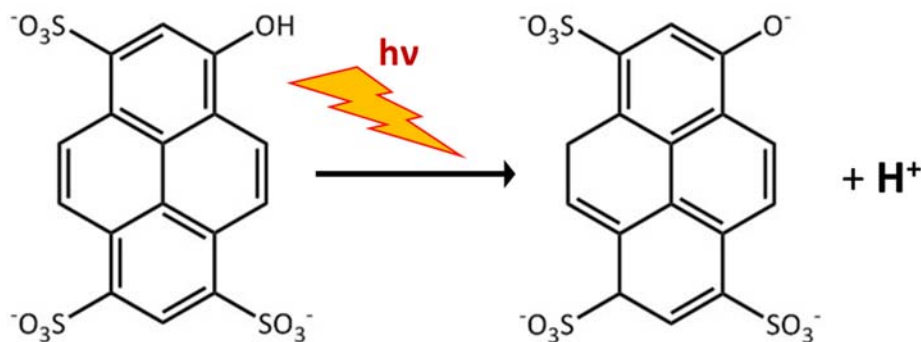


Figure 9.2: The photoacid HPTS (hydroxypyrenetrisulfonate) releases a proton following excitation at 400 nm.

The UV-Vis pump—CIR probe can be used to study the excited state vibrational dynamics in any system. With the incorporation of a third beam (which is currently limited to wavelengths of 800 nm or its harmonics), transient 2D IR measurements can be undertaken across the full vibrational spectrum to determine coupling in the excited state. This technique has been performed with traditional OPA pulses,¹⁶⁷ but the CIR probe would significantly increase the information gained from transient 2D IR.

9.4.4 Beyond Vibrational Experiments

The germanium cross correlation described in Chapter 3 demonstrates that the CIR probe can be applied to study any infrared absorbance, which is not limited to vibrational spectroscopy. Various structures such as quantum dots or nanocrystals have similar properties. Following an interband transition induced with UV through near-IR pump pulses, the intraband dynamics in the conduction band can be probed with mid-IR light.¹⁶⁸ The CIR probe provides a valuable advantage to these studies because this movement of free carriers can have very broad and ill-defined infrared absorbances, like the moving protons observed in proton transfer.

REFERENCES

1. Crick, F. H. C. & Watson, J. D. Molecular Structure of Nucleic Acids. *Nature* **737–738** (1953). at <http://www.nature.com/nature/journal/v171/n4356/pdf/171737a0.pdf>
2. Middleton, C. T. *et al.* DNA excited-state dynamics: from single bases to the double helix. *Annu. Rev. Phys. Chem.* **60**, 217–239 (2009).
3. Zhang, Y., de La Harpe, K., Beckstead, A. A., Improta, R. & Kohler, B. UV-Induced Proton Transfer between DNA Strands. *J. Am. Chem. Soc.* **137**, 7059–62 (2015).
4. Röttger, K. *et al.* Ultraviolet Absorption Induces Hydrogen-Atom Transfer in G-C Watson-Crick DNA Base Pairs in Solution. *Angew. Chem. Int. Ed. Engl.* **54**, 14719–22 (2015).
5. Stoner-Ma, D. *et al.* Observation of excited-state proton transfer in green fluorescent protein using ultrafast vibrational spectroscopy. *J. Am. Chem. Soc.* **127**, 2864–5 (2005).
6. Cukier, R. I. & Nocera, D. G. Proton-coupled electron transfer. *Annu. Rev. Phys. Chem.* **49**, 337–369 (1998).
7. Hammes-Schiffer, S. & Stuchebrukhov, A. A. Theory of coupled electron and proton transfer reactions. *Chem. Rev.* **110**, 6939–6960 (2010).
8. Eigen, M. Proton Transfer, Acid-Base Catalysis, and Enzymatic Hydrolysis. Part I: ELEMENTARY PROCESSES. *Angew. Chemie Int. Ed. English* **3**, 1–19 (1964).
9. Löwdin, P.-O. Proton Tunneling in DNA and its Biological Implications. *Rev. Mod. Phys.* **35**, 724–732 (1963).
10. Taylor, C. A., El-Bayoumi, M. A. & Kasha, M. EXCITED-STATE TWO-PROTON TAUTOMERISM IN HYDROGEN-BONDED N-

HETEROCYCLIC BASE PAIRS. *Proc. Natl. Acad. Sci.* **63**, 253–260 (1969).

11. Ingham, K. C., Abu-Elgheit, M. & El-Bayoumi, M. A. Confirmation of biprotonic phototautomerism in 7-azaindole hydrogen-bonded dimers. *J. Am. Chem. Soc.* **93**, 5023–5025 (1971).
12. Ingham, K. & El-Bayoumi, M. A. Photoinduced double proton transfer in a model hydrogen bonded base pair. Effects of temperature and deuterium substitution. *J. Am. Chem. Soc.* **96**, 1674–1682 (1974).
13. Bardez, E., Devol, I., Larrey, B. & Valeur, B. Excited-State Processes in 8-Hydroxyquinoline: Photoinduced Tautomerization and Solvation Effects. *J. Phys. Chem. B* **101**, 7786–7793 (1997).
14. Chou, P.-T. *et al.* Photoinduced Double Proton Tautomerism in 4-Azabenzimidazole. *J. Phys. Chem. B* **103**, 10042–10052 (1999).
15. Chou, P.-T. *et al.* Excited-State Amine–Imine Double Proton Transfer in 7-Azaindoline. *J. Phys. Chem. B* **104**, 7818–7829 (2000).
16. Chang, C.-P., Wen-Chi, H., Meng-Shin, K., Chou, P.-T. & Clements, J. H. Acid Catalysis of Excited-State Double-Proton Transfer in 7-Azaindole. *J. Phys. Chem.* **98**, 8801–8805 (1994).
17. Chou, P.-T. *et al.* Proton-Transfer Tautomerism of β -Carbolines Mediated by Hydrogen-Bonded Complexes. *J. Phys. Chem. B* **105**, 10674–10683 (2001).
18. Cheatum, C. M., Heckscher, M. M. & Fleming Crim, F. Excited-state dynamics in 8-hydroxyquinoline dimers. *Chem. Phys. Lett.* **349**, 37–42 (2001).
19. Ishikawa, H., Iwata, K. & Hamaguchi, H. Picosecond Dynamics of Stepwise Double Proton-Transfer Reaction in the Excited State of the 2-Aminopyridine/Acetic Acid System †. *J. Phys. Chem. A* **106**, 2305–2312 (2002).
20. Mukherjee, M., Karmakar, S. & Chakraborty, T. Excited state tautomerization of 7-azaindole in a 1:1 complex with δ -valerolactam: a comparative study with the homodimer. *J. Phys. Chem. A* **116**, 9888–96 (2012).

21. Ogawa, A. K. *et al.* A Phototautomerizable Model DNA Base Pair. *J. Am. Chem. Soc.* **122**, 9917–9920 (2000).
22. Tseng, H.-W. *et al.* Harnessing Excited-State Intramolecular Proton-Transfer Reaction via a Series of Amino-Type Hydrogen-Bonding Molecules. *J. Phys. Chem. Lett.* **6**, 1477–86 (2015).
23. Hetherington, W. M., Micheels, R. H. & Eisinger, K. E. Picosecond dynamics of double proton transfer in 7-azaindole dimers. *Chem. Phys. Lett.* **66**, 230–233 (1979).
24. Fuke, K. & Kaya, K. Dynamics of double-proton-transfer reaction in the excited-state model hydrogen-bonded base pairs. *J. Phys. Chem.* **93**, 614–621 (1989).
25. Share, P., Pereira, M., Sarisky, M., Repinec, S. & Hochstrasser, R. M. Dynamics of proton transfer in 7-azaindole. *J. Lumin.* **48-49**, 204–208 (1991).
26. Douhal, A., Kim, S. K. & Zewail, A. H. Femtosecond molecular dynamics of tautomerization in model base pairs. *Nature* **378**, 260–3 (1995).
27. Takeuchi, S. & Tahara, T. Observation of dimer excited-state dynamics in the double proton transfer reaction of 7-azaindole by femtosecond fluorescence up-conversion. *Chem. Phys. Lett.* **277**, 340–346 (1997).
28. Chachisvilis, M., Fiebig, T., Douhal, A. & Zewail, A. H. Femtosecond Dynamics of a Hydrogen-Bonded Model Base Pair in the Condensed Phase: Double Proton Transfer in 7-Azaindole. *J. Phys. Chem. A* **102**, 669–673 (1998).
29. Takeuchi, S. & Tahara, T. Femtosecond Ultraviolet–Visible Fluorescence Study of the Excited-State Proton-Transfer Reaction of 7-Azaindole Dimer. *J. Phys. Chem. A* **102**, 7740–7753 (1998).
30. Fiebig, T. *et al.* Femtosecond Dynamics of Double Proton Transfer in a Model DNA Base Pair: 7-Azaindole Dimers in the Condensed Phase. *J. Phys. Chem. A* **103**, 7419–7431 (1999).
31. Folmer, D. E., Wisniewski, E. S. & Castleman, A. W. Excited state double

- proton transfer in the 7-azaindole dimer revisited. *Chem. Phys. Lett.* **318**, 637–643 (2000).
32. Takeuchi, S. & Tahara, T. Excitation-wavelength dependence of the femtosecond fluorescence dynamics of 7-azaindole dimer: further evidence for the concerted double proton transfer in solution. *Chem. Phys. Lett.* **347**, 108–114 (2001).
 33. Kwon, O.-H. & Zewail, A. H. Double proton transfer dynamics of model DNA base pairs in the condensed phase. *Proc. Natl. Acad. Sci. U. S. A.* **104**, 8703–8 (2007).
 34. Takeuchi, S. & Tahara, T. The answer to concerted versus step-wise controversy for the double proton transfer mechanism of 7-azaindole dimer in solution. *Proc. Natl. Acad. Sci. U. S. A.* **104**, 5285–90 (2007).
 35. Guallar, V., Batista, V. S. & Miller, W. H. Semiclassical molecular dynamics simulations of excited state double-proton transfer in 7-azaindole dimers. *J. Chem. Phys.* **110**, 9922 (1999).
 36. Catalán, J. & Kasha, M. Photophysics of 7-Azaindole, Its Doubly-H-Bonded Base-Pair, and Corresponding Proton-Transfer-Tautomer Dimeric Species, via Defining Experimental and Theoretical Results. *J. Phys. Chem. A* **104**, 10812–10820 (2000).
 37. Serrano-Andrés, L. & Merchán, M. Theoretical CASPT2 study of the excited state double proton transfer reaction in the 7-azaindole dimer. *Chem. Phys. Lett.* **418**, 569–575 (2006).
 38. Sekiya, H. & Sakota, K. Excited-state double-proton transfer in a model DNA base pair: Resolution for stepwise and concerted mechanism controversy in the 7-azaindole dimer revealed by frequency- and time-resolved spectroscopy. *J. Photochem. Photobiol. C Photochem. Rev.* **9**, 81–91 (2008).
 39. Novak, A. Hydrogen bonding in solids correlation of spectroscopic and crystallographic data. *Large Mol.* (1974). at <http://www.springerlink.com/index/E15T41678T75T264.pdf>
 40. Woutersen, S. & Cristalli, G. Strong enhancement of vibrational relaxation by

- Watson-Crick base pairing. *J. Chem. Phys.* **121**, 5381–6 (2004).
41. Ganim, Z. *et al.* Amide I two-dimensional infrared spectroscopy of proteins. *Acc. Chem. Res.* **41**, 432–41 (2008).
 42. Kozich, V., Szyc, Ł., Nibbering, E. T. J., Werncke, W. & Elsaesser, T. Ultrafast redistribution of vibrational energy after excitation of NH stretching modes in DNA oligomers. *Chem. Phys. Lett.* **473**, 171–175 (2009).
 43. Szyc, Ł., Dwyer, J. R., Nibbering, E. T. J. & Elsaesser, T. Ultrafast dynamics of N–H and O–H stretching excitations in hydrated DNA oligomers. *Chem. Phys.* **357**, 36–44 (2009).
 44. Yang, M. *et al.* Dynamics and couplings of N-H stretching excitations of guanosine-cytidine base pairs in solution. *J. Phys. Chem. B* **115**, 5484–92 (2011).
 45. Lessing, J. *et al.* 2D IR Spectroscopic Study of the GVGXPGVG Peptide. 2–5 (2012).
 46. Greve, C. *et al.* N-H stretching modes of adenosine monomer in solution studied by ultrafast nonlinear infrared spectroscopy and ab initio calculations. *J. Phys. Chem. A* **116**, 7636–7644 (2012).
 47. Fidder, H. *et al.* N-H stretching vibrations of guanosine-cytidine base pairs in solution: ultrafast dynamics, couplings, and line shapes. *J. Phys. Chem. A* **117**, 845–54 (2013).
 48. De Marco, L., Thämer, M., Reppert, M. & Tokmakoff, A. Direct observation of intermolecular interactions mediated by hydrogen bonding. *J. Chem. Phys.* **141**, 034502 (2014).
 49. Siebert, T., Guchhait, B., Liu, Y., Costard, R. & Elsaesser, T. Anharmonic Backbone Vibrations in Ultrafast Processes at the DNA-Water Interface. *J. Phys. Chem. B* **119**, 9670–7 (2015).
 50. Kim, Y. S. & Hochstrasser, R. M. Applications of 2D IR Spectroscopy to Peptides, Proteins, and Hydrogen-Bond Dynamics †. 8231–8251 (2009).

51. Fayer, M. D. Dynamics of Liquids , Molecules , and Proteins Measured with Ultrafast 2D IR Vibrational Echo Chemical Exchange Spectroscopy. (2009). doi:10.1146/annurev-physchem-073108
52. Hamm, P. & Zanni, M. *Concepts and Methods of 2D Infrared Spectroscopy*. (Cambridge University Press, 2011). at <<https://books.google.com/books?hl=en&lr=&id=hRbJ5n9bPGAC&pgis=1>>
53. Fayer, M. D. *Ultrafast Infrared Vibrational Spectroscopy*. **2**, (CRC Press, 2013).
54. Lim, M. & Hochstrasser, R. M. Unusual vibrational dynamics of the acetic acid dimer. *J. Chem. Phys.* **115**, 7629–7643 (2001).
55. Huse, N. *et al.* Anharmonic couplings underlying the ultrafast vibrational dynamics of hydrogen bonds in liquids. *Phys. Rev. Lett.* **95**, 147402 (2005).
56. Heyne, K. *et al.* Coherent low-frequency motions of hydrogen bonded acetic acid dimers in the liquid phase. *J. Chem. Phys.* **121**, 902–13 (2004).
57. Dreyer, J. Hydrogen-bonded acetic acid dimers: anharmonic coupling and linear infrared spectra studied with density-functional theory. *J. Chem. Phys.* **122**, 184306 (2005).
58. Dwyer, J. R., Dreyer, J., Nibbering, E. T. J. & Elsaesser, T. Ultrafast dynamics of vibrational N–H stretching excitations in the 7-azaindole dimer. *Chem. Phys. Lett.* **432**, 146–151 (2006).
59. Dreyer, J. Unraveling the structure of hydrogen bond stretching mode infrared absorption bands: an anharmonic density functional theory study on 7-azaindole dimers. *J. Chem. Phys.* **127**, 054309 (2007).
60. Elsaesser, T. *et al.* Ultrafast vibrational dynamics and anharmonic couplings of hydrogen-bonded dimers in solution. *Chem. Phys.* **341**, 175–188 (2007).
61. Petersen, P. B., Roberts, S. T., Ramasesha, K., Nocera, D. G. & Tokmakoff, A. Ultrafast N-H vibrational dynamics of cyclic doubly hydrogen-bonded homo- and heterodimers. *J. Phys. Chem. B* **112**, 13167–13171 (2008).

62. Kozich, V., Dreyer, J. & Werncke, W. Mode-selective vibrational redistribution after spectrally selective N-H stretching mode excitation in intermolecular hydrogen bonds. *J. Chem. Phys.* **130**, 034505 (2009).
63. Szyc, Ł. *et al.* The hydrogen-bonded 2-pyridone dimer model system. 1. Combined NMR and FT-IR spectroscopy study. *J. Phys. Chem. A* **114**, 7749–60 (2010).
64. Yang, M., Szyc, Ł., Dreyer, J., Nibbering, E. T. J. & Elsaesser, T. The hydrogen-bonded 2-pyridone dimer model system. 2. Femtosecond mid-infrared pump-probe study. *J. Phys. Chem. A* **114**, 12195–201 (2010).
65. Kato, T. & Shirota, H. Intermolecular vibrational modes and orientational dynamics of cooperative hydrogen-bonding dimer of 7-azaindole in solution. *J. Chem. Phys.* **134**, 164504 (2011).
66. Greve, C., Nibbering, E. T. J. & Fidler, H. Hydrogen-bonding-induced enhancement of Fermi resonances: a linear IR and nonlinear 2D-IR study of aniline-d₅. *J. Phys. Chem. B* **117**, 15843–55 (2013).
67. Stingel, A. M., Calabrese, C. & Petersen, P. B. Strong Intermolecular Vibrational Coupling through Cyclic Hydrogen-Bonded Structures Revealed by Ultrafast Continuum mid-IR Spectroscopy. *J. Phys. Chem. B* **117**, 15714–15719 (2013).
68. Costard, R., Greve, C., Fidler, H. & Nibbering, E. T. J. Hydrogen bonding induced enhancement of Fermi resonances: ultrafast vibrational energy flow dynamics in aniline-d₅. *J. Phys. Chem. B* **119**, 2711–25 (2015).
69. Van Hoozen, B. L. & Petersen, P. B. Origin of the 900 cm⁻¹ broad double-hump OH vibrational feature of strongly hydrogen-bonded carboxylic acids. *J. Chem. Phys.* **142**, 104308 (2015).
70. Chou, P.-T., Wei, C.-Y., Chang, C.-P. & Kuo, M.-S. Structure and Thermodynamics of 7-Azaindole Hydrogen-Bonded Complexes. *J. Phys. Chem.* **99**, 11994–12000 (1995).
71. Suzuki, T., Okuyama, U. & Ichimura, T. Double Proton Transfer Reaction of 7-Azaindole Dimer and Complexes Studied by Time-Resolved Thermal Lensing

- Technique. *J. Phys. Chem. A* **101**, 7047–7052 (1997).
72. Dreyer, J. Density functional theory simulations of two-dimensional infrared spectra for hydrogen-bonded acetic acid dimers. *Int. J. Quantum Chem.* **104**, 782–793 (2005).
 73. Rubtsov, I. V., Wang, J. & Hochstrasser, R. M. Dual frequency 2D-IR of peptide amide-A and amide-I modes. *J. Chem. Phys.* **118**, 7733 (2003).
 74. Dougherty, T. P. & Heilweil, E. J. Dual-beam subpicosecond broadband infrared spectrometer. **19**, 129–131 (1994).
 75. Nyby, C. M. *et al.* Mid-IR beam direction stabilization scheme for vibrational spectroscopy, including dual-frequency 2DIR. *Opt. Express* **22**, 6801–9 (2014).
 76. Leger, J. D. *et al.* Fully automated dual-frequency three-pulse-echo 2DIR spectrometer accessing spectral range from 800 to 4000 wavenumbers. *Rev. Sci. Instrum.* **85**, 083109 (2014).
 77. Bian, H. *et al.* Molecular Conformations and Dynamics on Surfaces of Gold Nanoparticles Probed with Multiple-Mode Multiple-Dimensional Infrared Spectroscopy. *J. Phys. Chem. C* **116**, 7913–7924 (2012).
 78. Tyrode, E. & Hedberg, J. A Comparative Study of the CD and CH Stretching Spectral Regions of Typical Surfactants Systems Using VSFS: Orientation Analysis of the Terminal CH 3 and CD 3 Groups. *J. Phys. Chem. C* **116**, 1080–1091 (2012).
 79. Calabrese, C., Stingel, A. M., Shen, L. & Petersen, P. B. Ultrafast continuum mid-infrared spectroscopy: probing the entire vibrational spectrum in a single laser shot with femtosecond time resolution. *Opt. Lett.* **37**, 2265–2267 (2012).
 80. Gündoğdu, K., Bandaria, J., Nydegger, M., Rock, W. & Cheatum, C. M. Relaxation and anharmonic couplings of the O-H stretching vibration of asymmetric strongly hydrogen-bonded complexes. *J. Chem. Phys.* **127**, 044501 (2007).
 81. Greve, C. *et al.* N-H stretching excitations in adenosine-thymidine base pairs in

- solution: pair geometries, infrared line shapes, and ultrafast vibrational dynamics. *J. Phys. Chem. A* **117**, 594–606 (2013).
82. Stenger, J. *et al.* Femtosecond mid-infrared photon echo study of an intramolecular hydrogen bond. *Chem. Phys. Lett.* **354**, 256–263 (2002).
 83. Kozich, V., Dreyer, J., Ashihara, S., Werncke, W. & Elsaesser, T. Mode-selective O-H stretching relaxation in a hydrogen bond studied by ultrafast vibrational spectroscopy. *J. Chem. Phys.* **125**, 074504 (2006).
 84. Kozich, V. & Werncke, W. Non-degenerate second-order scattering and difference combination bands in infrared-pump/anti-Stokes resonance Raman-probe experiments. *J. Raman Spectrosc.* **38**, 1180–1185 (2007).
 85. De Marco, L., Ramasesha, K. & Tokmakoff, A. Experimental Evidence of Fermi Resonances in Isotopically Dilute Water from Ultrafast Broadband IR Spectroscopy. *J. Phys. Chem. B* (2013). doi:10.1021/jp4034613
 86. Thamer, M., De Marco, L., Ramasesha, K., Mandal, A. & Tokmakoff, A. Ultrafast 2D IR spectroscopy of the excess proton in liquid water. *Science* (80-.). **350**, 78–82 (2015).
 87. Mandal, A., Ramasesha, K., De Marco, L. & Tokmakoff, A. Collective vibrations of water-solvated hydroxide ions investigated with broadband 2DIR spectroscopy. *J. Chem. Phys.* **140**, 204508 (2014).
 88. Ramasesha, K., De Marco, L., Mandal, A. & Tokmakoff, A. Water vibrations have strongly mixed intra- and intermolecular character. *Nat. Chem.* **5**, 935–40 (2013).
 89. Mandal, A. & Tokmakoff, A. Vibrational dynamics of aqueous hydroxide solutions probed using broadband 2DIR spectroscopy. *J. Chem. Phys.* **143**, 194501 (2015).
 90. Chen, H., Bian, H., Li, J., Wen, X. & Zheng, J. Relative Intermolecular Orientation Probed via Molecular Heat Transport. *J. Phys. Chem. A* (2013). doi:10.1021/jp312604v

91. Beckerle, J. D., Casassa, M. P., Cavanagh, R. R., Heilweil, E. J. & Stephenson, J. C. Sub-picosecond time-resolved IR spectroscopy of the vibrational dynamics of Rh (CO)₂ (acac). *Chem. Phys.* **160**, 487–497 (1992).
92. Dougherty, T. P., Grubbs, W. T. & Heilweil, E. J. Photochemistry of Rh(CO)₂(acetylacetonate) and Related Metal Dicarbonyls Studied by Ultrafast Infrared Spectroscopy. *J. Phys. Chem.* **98**, 9396–9399 (1994).
93. Merchant, K. A., Thompson, D. E. & Fayer, M. D. Two-dimensional time-frequency ultrafast infrared vibrational echo spectroscopy. *Phys. Rev. Lett.* **86**, 3899–902 (2001).
94. Khalil, M., Demirdöven, N. & Tokmakoff, A. Coherent 2D IR Spectroscopy: Molecular Structure and Dynamics in Solution. *J. Phys. Chem. A* **107**, 5258–5279 (2003).
95. Baiz, C. R., McRobbie, P. L., Anna, J. M., Geva, E. & Kubarych, K. J. Two-dimensional infrared spectroscopy of metal carbonyls. *Acc. Chem. Res.* **42**, 1395–404 (2009).
96. Khalil, M., Demirdöven, N. & Tokmakoff, A. Vibrational coherence transfer characterized with Fourier-transform 2D IR spectroscopy. *J. Chem. Phys.* **121**, 362–373 (2004).
97. DeFlores, L. P., Nicodemus, R. A. & Tokmakoff, A. Two-dimensional Fourier transform spectroscopy in the pump-probe geometry. *Opt. Lett.* **32**, 2966 (2007).
98. Shim, S.-H. & Zanni, M. T. How to turn your pump-probe instrument into a multidimensional spectrometer: 2D IR and Vis spectroscopies via pulse shaping. *Phys. Chem. Chem. Phys.* **11**, 748–61 (2009).
99. Heilweil, E. J. Ultrashort-pulse multichannel infrared spectroscopy using broadband frequency conversion in LiIO(3). *Opt. Lett.* **14**, 551–3 (1989).
100. Tokmakoff, a., Marshall, C. D. & Fayer, M. D. Optical parametric amplification of 1-kHz high-energy picosecond midinfrared pulses and application to infrared transient-grating experiments on diamond. *J. Opt. Soc. Am. B* **10**, 1785 (1993).

101. Emmerichs, U., Woutersen, S. & Bakker, H. J. Generation of intense femtosecond optical pulses near 3 μm with a kilohertz repetition rate. *J. Opt. Soc. Am. B* **14**, 1480 (1997).
102. Kaindl, R. A. *et al.* Generation, shaping, and characterization of intense femtosecond pulses tunable from 3 to 20 μm . *J. Opt. Soc. Am. B* **17**, 2086–2094 (2000).
103. Fecko, C. J., Loparo, J. J. & Tokmakoff, A. Generation of 45 femtosecond pulses at 3 μm with a KNbO₃ optical parametric amplifier. *Opt. Commun.* **241**, 521–528 (2004).
104. Shirai, H., Yeh, T.-T., Nomura, Y., Luo, C.-W. & Fuji, T. Ultrabroadband Midinfrared Pump-Probe Spectroscopy Using Chirped-Pulse Up-conversion in Gases. *Phys. Rev. Appl.* **3**, 051002 (2015).
105. Cook, D. J. & Hochstrasser, R. M. Intense terahertz pulses by four-wave rectification in air. *Opt. Lett.* **25**, 1210–2 (2000).
106. Kress, M., Löffler, T., Eden, S., Thomson, M. & Roskos, H. G. Terahertz-pulse generation by photoionization of air with laser pulses composed of both fundamental and second-harmonic waves. *Opt. Lett.* **29**, 1120–1122 (2004).
107. Dai, J., Karpowicz, N. & Zhang, X.-C. Coherent Polarization Control of Terahertz Waves Generated from Two-Color Laser-Induced Gas Plasma. *Phys. Rev. Lett.* **103**, 023001 (2009).
108. Fuji, T. & Suzuki, T. Generation of sub-two-cycle mid-infrared pulses by four-wave mixing through filamentation in air. *Opt. Lett.* **32**, 3330–2 (2007).
109. Petersen, P. B. & Tokmakoff, A. Source for ultrafast continuum infrared and terahertz radiation. *Opt. Lett.* **35**, 1962–1964 (2010).
110. Cheng, M., Reynolds, A., Widgren, H. & Khalil, M. Generation of tunable octave-spanning mid-infrared pulses by filamentation in gas media. *Opt. Lett.* **37**, 1787–1789 (2012).
111. Fuji, T., Nomura, Y. & Suzuki, T. Generation of Phase-Stable Sub-Cycle Mid-

- Infrared Pulses from Filamentation in Nitrogen. *Appl. Sci.* **3**, 122–138 (2013).
112. Serrano, A. L., Ghosh, A., Ostrander, J. S. & Zanni, M. T. Wide-field FTIR microscopy using mid-IR pulse shaping. *Opt. Express* **23**, 17815–27 (2015).
 113. Ghosh, A. *et al.* Experimental implementations of 2D IR spectroscopy through a horizontal pulse shaper design and a focal plane array detector. *Opt. Lett.* **41**, 524 (2016).
 114. Baiz, C. R. & Kubarych, K. J. Ultrabroadband detection of a mid-IR continuum by chirped-pulse upconversion. *Opt. Lett.* **36**, 187–189 (2011).
 115. Nomura, Y. *et al.* Single-shot detection of mid-infrared spectra by chirped-pulse upconversion with four-wave difference frequency generation in gases. *Opt. Express* **21**, 18249 (2013).
 116. Shim, S.-H., Strasfeld, D. B., Fulmer, E. C. & Zanni, M. T. Femtosecond pulse shaping directly in the mid-IR using acousto-optic modulation. *Opt. Lett.* **31**, 838–840 (2006).
 117. Nite, J. M., Cyran, J. D. & Krummel, A. T. Active Bragg angle compensation for shaping ultrafast mid-infrared pulses. *Opt. Express* **20**, 23912 (2012).
 118. Zanni, M. T. & Hochstrasser, R. M. Two-dimensional infrared spectroscopy: a promising new method for the time resolution of structures. *Curr. Opin. Struct. Biol.* **11**, 516–22 (2001).
 119. Woutersen, S. & Hamm, P. Nonlinear two-dimensional vibrational spectroscopy of peptides. *J. Phys. Condens. Matter* **14**, R1035–R1062 (2002).
 120. Roberts, S. T. *et al.* Observation of a Zundel-like transition state during proton transfer in aqueous hydroxide solutions. *Proc. Natl. Acad. Sci. U.S.A.* **106**, 15154–15159 (2009).
 121. Szyk, Ł., Yang, M., Nibbering, E. T. J. & Elsaesser, T. Ultrafast vibrational dynamics and local interactions of hydrated DNA. *Angew. Chem. Int. Ed.* **49**, 3598–3610 (2010).

122. Yang, M., Szyc, Ł. & Elsaesser, T. Femtosecond two-dimensional infrared spectroscopy of adenine-thymine base pairs in DNA oligomers. *J. Phys. Chem. B* **115**, 1262–7 (2011).
123. Hamm, P. Coherent effects in femtosecond infrared spectroscopy. *Chem. Phys.* **200**, 415–429 (1995).
124. Tauber, M. J., Mathies, R. A., Chen, X. & Bradforth, S. E. Flowing liquid sample jet for resonance Raman and ultrafast optical spectroscopy. *Rev. Sci. Instrum.* **74**, 4958 (2003).
125. Bratos, S., Leicknam, J.-C. & Pommeret, S. Relation between the OH stretching frequency and the OO distance in time-resolved infrared spectroscopy of hydrogen bonding. *Chem. Phys.* **359**, 53–57 (2009).
126. Doepker, R. D. & Ausloos, P. Gas-Phase Photolysis of Cyclohexane in the Far Ultraviolet: Modes of Decomposition of the Neutral Excited Cyclohexane Molecule and Reactions of the Parent Cyclohexane Ion. *J. Chem. Phys.* **42**, 3746 (1965).
127. Ausloos, P., Rebbert, R. E. & Lias, S. G. Gas-phase photolysis of cyclohexane in the photoionization region. *J. Phys. Chem.* **72**, 3904–3914 (1968).
128. Liljeblad, J. F. D. & Tyrode, E. Vibrational sum frequency spectroscopy studies at solid/liquid interfaces: Influence of the experimental geometry in the spectral shape and enhancement. *J. Phys. Chem. C* **116**, 22893–22903 (2012).
129. Agger, C. *et al.* Supercontinuum generation in ZBLAN fibers—detailed comparison between measurement and simulation. *J. Opt. Soc. Am. B* **29**, 635 (2012).
130. Xia, C. *et al.* 10.5 W Time-Averaged Power Mid-IR Supercontinuum Generation Extending Beyond 4 μm With Direct Pulse Pattern Modulation. *IEEE J. Sel. Top. Quantum Electron.* **15**, 422–434 (2009).
131. Domachuk, P. *et al.* Over 4000 nm bandwidth of mid-IR supercontinuum generation in sub-centimeter segments of highly nonlinear tellurite PCFs. *Opt. Express* **16**, 7161 (2008).

132. Petersen, C. R. *et al.* Mid-infrared supercontinuum covering the 1.4–13.3 μm molecular fingerprint region using ultra-high NA chalcogenide step-index fibre. *Nat. Photonics* **8**, 830–834 (2014).
133. Théberge, F. *et al.* Multioctave infrared supercontinuum generation in large-core As_2S_3 fibers. *Opt. Lett.* **39**, 6474–7 (2014).
134. Yu, Y. *et al.* 1.8-10 μm mid-infrared supercontinuum generated in a step-index chalcogenide fiber using low peak pump power. *Opt. Lett.* **40**, 1081–4 (2015).
135. Mouawad, O. *et al.* Multioctave midinfrared supercontinuum generation in suspended-core chalcogenide fibers. *Opt. Lett.* **39**, 2684–7 (2014).
136. Saini, T., Kumar, A. & Sinha, R. Broadband mid-infrared supercontinuum spectra spanning 2 – 15 μm using As_2Se_3 chalcogenide glass triangular-core graded-index photonic crystal fiber. *J. Light. Technol.* **PP**, 1–1 (2015).
137. Hudson, D. D., Baudisch, M., Werdehausen, D., Eggleton, B. J. & Biegert, J. 1.9 octave supercontinuum generation in a As_2S_3 step-index fiber driven by mid-IR OPCPA. *Opt. Lett.* **39**, 5752–5 (2014).
138. Kedenburg, S., Steinle, T., Mörz, F., Steinmann, A. & Giessen, H. High-power mid-infrared high repetition-rate supercontinuum source based on a chalcogenide step-index fiber. *Opt. Lett.* **40**, 2668–71 (2015).
139. Eggleton, B. J., Luther-Davies, B. & Richardson, K. Chalcogenide photonics. *Nat Phot.* **5**, 141–148 (2011).
140. Yu, Y. *et al.* A broadband, quasi-continuous, mid-infrared supercontinuum generated in a chalcogenide glass waveguide. *Laser Photon. Rev.* **8**, 792–798 (2014).
141. Karim, M. R., Rahman, B. M. A. & Agrawal, G. P. Dispersion engineered $\text{Ge}_{115}\text{As}_{24}\text{Se}_{645}$ nanowire for supercontinuum generation: A parametric study. *Opt. Express* **22**, 31029 (2014).
142. Gao, W. *et al.* Mid-infrared supercontinuum generation in a suspended-core As_2S_3 chalcogenide microstructured optical fiber. *Opt. Express* **21**, 9573–83

(2013).

143. Kubat, I. *et al.* Thulium pumped mid-infrared 0.9-9 μm supercontinuum generation in concatenated fluoride and chalcogenide glass fibers. *Opt. Express* **22**, 3959–67 (2014).
144. Cheng, T. *et al.* Mid-infrared supercontinuum generation in a novel AsSe₂-As₂S₅ hybrid microstructured optical fiber. *Opt. Express* **22**, 23019–25 (2014).
145. Møller, U. *et al.* Multi-milliwatt mid-infrared supercontinuum generation in a suspended core chalcogenide fiber. *Opt. Express* **23**, 3282–91 (2015).
146. Hudson, D. D. *et al.* Octave spanning supercontinuum in an As₂S₃ taper using ultralow pump pulse energy. *Opt. Lett.* **36**, 1122–4 (2011).
147. Hu, J., Menyuk, C. R., Shaw, L. B., Sanghera, J. S. & Aggarwal, I. D. Maximizing the bandwidth of supercontinuum generation in As₂Se₃ chalcogenide fibers. *Opt. Express* **18**, 6722–39 (2010).
148. Gattass, R. R. *et al.* All-fiber chalcogenide-based mid-infrared supercontinuum source. *Opt. Fiber Technol.* **18**, 345–348 (2012).
149. Gao, W. *et al.* Mid-infrared supercontinuum generation in a four-hole As₂S₅ chalcogenide microstructured optical fiber. *Appl. Phys. B* **116**, 847–853 (2014).
150. Liao, M. *et al.* Five-Octave-Spanning Supercontinuum Generation in Fluoride Glass. *Appl. Phys. Express* **6**, 032503 (2013).
151. Liao, M. *et al.* Ultrabroad supercontinuum generation through filamentation in tellurite glass. *Laser Phys. Lett.* **10**, 036002 (2013).
152. Silva, F. *et al.* Multi-octave supercontinuum generation from mid-infrared filamentation in a bulk crystal. *Nat. Commun.* **3**, 807 (2012).
153. Corkum, P. B., Ho, P. P., Alfano, R. R. & Manassah, J. T. Generation of infrared supercontinuum covering 3–14 μm in dielectrics and semiconductors. *Opt. Lett.* **10**, 624 (1985).

154. Pigeon, J. J., Tochitsky, S. Y., Gong, C. & Joshi, C. Supercontinuum generation from 2 to 20 μm in GaAs pumped by picosecond CO_2 laser pulses. *Opt. Lett.* **39**, 3246–9 (2014).
155. Ashihara, S. & Kawahara, Y. Spectral broadening of mid-infrared femtosecond pulses in GaAs. *Opt. Lett.* **34**, 3839–41 (2009).
156. Yu, Y. *et al.* Mid-infrared supercontinuum generation in chalcogenides. *Opt. Mater. Express* **3**, 1075 (2013).
157. Lanin, A. A., Voronin, A. A., Stepanov, E. A., Fedotov, A. B. & Zheltikov, A. M. Multioctave, 3–18 μm sub-two-cycle supercontinua from self-compressing, self-focusing soliton transients in a solid. *Opt. Lett.* **40**, 974–7 (2015).
158. Demirdöven, N., Khalil, M., Golonzka, O. & Tokmakoff, A. Dispersion compensation with optical materials for compression of intense sub-100-fs mid-infrared pulses. *Opt. Lett.* **27**, 433 (2002).
159. McDermott, M. L. & Petersen, P. B. Robust Self-Referencing Method for Chiral Sum Frequency Generation Spectroscopy. *J. Phys. Chem. B* **119**, 12417–23 (2015).
160. Barrett, A. & Petersen, P. B. Order of Dry and Wet Mixed-Length Self-Assembled Monolayers. *J. Phys. Chem. C* **119**, 23943–23950 (2015).
161. Calabrese, C., Vanselous, H. & Petersen, P. B. Deconstructing the Heterogeneity of Surface-Bound Catalysts: Rutile Surface Structure Affects Molecular Properties. *J. Phys. Chem. C* **120**, 1515–1522 (2016).
162. Woutersen, S. & Bakker, H. J. Ultrafast vibrational and structural dynamics of the proton in liquid water. *Phys. Rev. Lett.* **96**, 138305 (2006).
163. Lindemann, R. & Zundel, G. Symmetry of hydrogen bonds, infrared continuous absorption and proton transfer. *J. Chem. Soc. Faraday Trans. 2* **68**, 979 (1972).
164. Steinel, T. *et al.* Water dynamics: dependence on local structure probed with vibrational echo correlation spectroscopy. *Chem. Phys. Lett.* **386**, 295–300 (2004).

165. Siwick, B. J. & Bakker, H. J. On the role of water in intermolecular proton-transfer reactions. *J. Am. Chem. Soc.* **129**, 13412–20 (2007).
166. Mohammed, O. F., Dreyer, J., Magnes, B.-Z., Pines, E. & Nibbering, E. T. J. Solvent-dependent photoacidity state of pyranine monitored by transient mid-infrared spectroscopy. *Chemphyschem* **6**, 625–36 (2005).
167. Xiong, W. *et al.* Transient 2D IR Spectroscopy of Charge Injection in Dye-Sensitized Nanocrystalline Thin Films. *J. Am. Chem. Soc.* **131**, 18040–18041 (2009).
168. Chen, J. *et al.* Ultrafast Photoinduced Interfacial Proton Coupled Electron Transfer from CdSe Quantum Dots to 4,4'-Bipyridine. *J. Am. Chem. Soc.* **138**, 884–892 (2016).